University of California
Santa Barbara

Designing novel cell-based structures for energy absorption

A dissertation submitted in partial satisfaction
of the requirements for the degree

Doctor of Philosophy
in
Mechanical Engineering

by

Steven Craig Wehmeyer

Committee in charge:

Professor Matthew R. Begley, Chair
Professor Robert M. McMeeking
Professor Frank W. Zok
Professor Otger Campas

September 2019

The Dissertation of Steven Craig Wehmeyer is approved.

Professor Robert M. McMeeking

Professor Frank W. Zok

Professor Otger Campas

Professor Matthew R. Begley, Committee Chair

June 2019

Designing novel cell-based structures for energy absorption

by

Steven Craig Wehmeyer

I dedicate this thesis to my wife who has supported me, challenged me, and encouraged me constantly, and to my kids, all of whom I love and cherish. This work is also dedicated to my parents, who have supported my family in countless ways - providing the freedom to pursue any avenue I may choose, and supporting me wholeheartedly along the way.

"Ambitious people know that everything they do and every discipline they adhere to form the links in the chain of events that will lead them to their final destination."

-Jim Rohn

Acknowledgements

First and foremost, I would like to gratefully acknowledge support from my advisor, Matthew Begley, who has been a tremendous mentor both professionally and personally. Always believing in me, even when I may not have believed in myself, and pushing me to become a better student, researcher, and person. Next, I'd like to thank Frank Zok for his guidance and support. The dissertation committee members, Begley research group, fellow mechanical engineering students, and the mechanical engineering staff at UCSB have all been a great resource for discussions to spur creativity and provide encouragement when needed.

I also gratefully acknowledge support provided by the Institute for Collaborative Biotechnologies through grant W911NF-09-0001 from the U.S. Army Research Office for funding this research. The content of the information does not necessarily reflect the position or the policy of the Government, and no official endorsement should be inferred.

Lastly, the authors also acknowledge support from the Center for Scientific Computing from the CNSI, MRL: an NSF MRSEC (DMR-1720256) and NSF CNS-1725797 for access to the supercomputers at UCSB.

Curriculum Vitæ

Steven Craig Wehmeyer

Education

2019 **Doctor of Philosophy, Mechanical Engineering**
Solid Mechanics, Materials, and Structures
University of California, Santa Barbara
GPA 3.85/4.0

2010 **Bachelor of Science, Mechanical Engineering**
Bachelor of Science, Engineering
Arkansas State University, Jonesboro
GPA 3.82/4.0

Research Experience

2011-2019 **Graduate Student Researcher**
University of California, Santa Barbara
PI: Prof. Matthew R. Begley
Studied the non-linear behavior of struts under compression for polymeric, elastic lattice structures. Developed analytical models, as well as extensive finite element simulations (using Abaqus) to accurately predict and tailor stress-strain responses. This effort was funded by the Institute for Collaborative Biotechnologies (ICB) through a partnership with UCSB, other academic institutions, industry, and the U.S. Army.

2010 **Research Experience for Undergraduates**
University of Arkansas, Fayetteville
PI: Prof. Ajay Malshe
Researched purification of single-walled carbon nanotubes. Developed a novel process or purification to drastically reduce processing time and increase high purity yield.

2009-2010 **Undergraduate Thesis Research**
Arkansas State University, Jonesboro
PI: Prof Nathan B. Edgar
Power electronics components were studied in SolidWorks Simulation modeling heat transfer. These models were compared to analytical and experimental results to validate the numerical model.

Teaching Experience

Spring 2014	ME189C Capstone Senior Design
Winter 2010	ME151B Thermodynamics II
Fall 2010	ME151A Thermodynamics I

Publications

2019	S. Wehmeyer, F.W. Zok, C. Eberl, P. Gumbsch, and M.R. Begley, "Post-buckling and dynamic response of angled struts in elastic lattices," *Journal of the Mechanics and Physics of Solids", accepted for publication.*
2010	Wehmeyer, Steven. "Experimental and Numerical Simulation: Cooling Power Electronics Components". Thesis. Arkansas State University, 2010.

Awards and Certificates

2010	EIT license
2010	Arkansas State University High Honors graduate

Abstract

Designing novel cell-based structures for energy absorption

by

Steven Craig Wehmeyer

The design of cellular materials with controlled energy dissipation is relevant to a broad range of applications, ranging from cushioning (such as shoes and athletic protection) to vibration control in damped, lightweight structures. Additive manufacturing has dramatically expanded the design space for such structures, enabling a diverse range of topologies. This dissertation establishes analysis techniques to make quantitative links between base properties, strut topology and cellular response; those techniques are then used to conduct case studies of various classes of strut-based structures to generate insight regarding effective strategies for designs that achieve specific types of response. Key contributions include: (i) a detailed numerical study of buckling behaviors that control large deformation response of low-density, elastic structures, (ii) the development of analytical and reduced-order models for buckling behaviors in viscoelastic struts subject to dynamic loading, (iii) a highly efficient framework to predict the damped frequency response of cellular materials, and (iv) a broad study of the effects of topology in single-celled structures, including the use of multiple strut sizes.

These contributions have led to several new, quantitative insights regarding the design of low- density structures to control energy dispersion. (i) For cellular materials that include struts that lie at an angle to the direction of compression, snap-through behaviors influence both the initial softening at small strains and the stiffening behavior observed at moderate strains. The models presented in this work illustrate that novel structures comprising cells with struts at multiple angles create significant opportunities to control

the softening regime that falls between initial response and stiffening associated with large deformation. (ii) Cellular structures comprising viscoelastic struts create significant opportunities to improve vibration damping through a combination of materials selection and topological design. The use of high damping materials as the core of composite struts can improve damping over the base shell material by a factor of 5-10 while maintaining the stiffness of the base structure. The use of non-uniform cells that disrupt standing waves insight structures can further increase damping by a factor of two, with potentially larger gains possible with topology optimization. (iii) The use of internal struts that sub-divide larger cells provides stabilization of buckling events; this can be exploited to improve both the onset of non-linearity (broadly defined, strength) and the energy absorbed by purely elastic structures subjected to compression. The broad topology study illustrates that response is highly sensitive to small variations in internal topology, indicating that topology optimization must rely on direct search algorithms.

Contents

List of Figures

Chapter 1

Introduction

1.1 Brief overview of low relative density materials

Lightweight, highly porous polymers are widely used to control the transmission of force, momentum or energy between two bodies, in applications such as running shoes, car interiors, clothing for blast protection, and athletic equipment such as helmets and floor padding. In many of these, high specific modulus and high specific strength are highly desirable for weight reduction, while reversible energy dissipation is desirable to mitigate transmitted forces during repeating impacts. Figure 1.1A illustrates key aspects of the macroscopic compression response of low relative density materials. A central feature is the presence of sharp stiffness drops upon compressive loading. In the extreme, the effective tangent modulus goes to near zero, such that a constant (plateau) stress persists to relatively large values of macroscopic strain, typically about 50% when measured macroscopically. The presence of a large plateau region is typically associated with relative densities less than $\sim$ 10%, although there are many examples where such low relative densities exhibit no clearly defined plateau [3–5]. For some low density materials, the stiffness can be a strong function of strain even prior to densification. It should be

appreciated that the behaviors shown schematically in Figure 1.1A are meant to highlight the diversity of foam behavior; specific details of the range of stiffness, strength and densification strains vary widely with base properties, relative density and cell architecture.

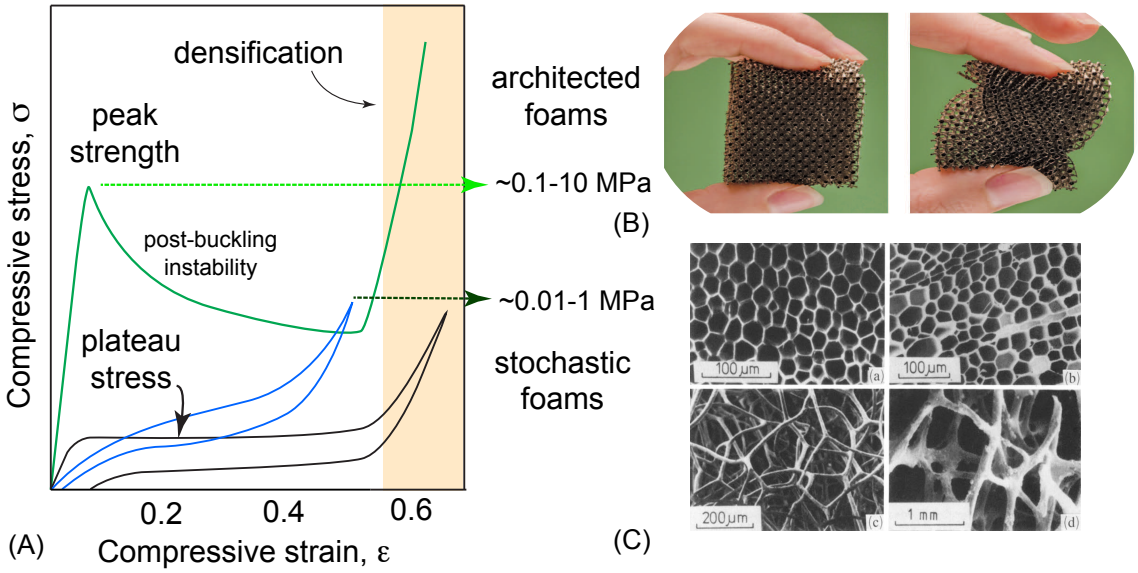

Figure 1.1: (A) Schematic illustrations of compression stress-strain curves of low density materials, showing a range of non-linear beahviors achievable with stochastic and architected foams. (B) An example of a architected foam from the literature [1]. (C) Classical examples of the microstructures of closed and open celled stochastic foams. [2]

By far, the most common material used for such applications are stochastic, polymeric foams made by expanding bubbles of gas dissolved in the uncured resin. Such foams can have either open cells (i.e. adjacent voids are all connected, leaving a network of struts) or closed cells (i.e. adjacent voids are separated by thin plates or membranes of resin). The size and shape of the cells can be varied significantly, spanning from micron to centimeter scales and from equiaxial to highly elongated pores, respectively; classical examples are shown in Figure 1.1C. [2] The ability to synthesize such strong variations in microstructure enables materials designers to produce a variety of stress-strain responses. The degree of non-linearity can be varied significantly, with stiffness changes spanning

from small reductions in tangent modulus to plateau stresses that span large strain ranges. It is critical to recognize that in many foams, large macroscopic strains do not necessarily imply large strains in the struts or cell walls. As such, many foams exhibit reversible behavior, often with hysteresis generated by viscoelastic behaviors exhibited by the base resin.

The relationship between foam structure and mechanical response has largely been elucidated by the work of Ashby and Gibson [6], who identified powerful scaling relationships to describe the effective modulus and strength of the foam in terms of cell size and the dimensions of the walls or struts. The key insight of this impressive body of work is that relative density is the dominant scaling factor in foam response; approximate values for specific modulus, specific strength and densification strains can all be predicted using relative density. For low density foams (say densities less than 20%), the response is dominated by bending of cell walls or struts. Elementary beam theory combined with idealizations of the cell geometry provide a means to translate cell dimensions to both relative density and effective macroscopic stiffness. Similarly, the models produce estimates for plateau stress based on strut buckling. It is worth noting that while densification is discussed extensively in Gibson/Ashby, the associated modeling approaches are largely empirical.

Structured cellular materials, often referred to as lattice or metamaterials, create many opportunities to overcome the inherent limitations of stochastic foams; a recent example is shown in Figure 1.1B [1]. In these materials, cell topology is exploited to control deformation mechanisms. Generally, the architecture is chosen to suppress bending deformations in favor of axial extension/compression of the cell walls (struts). (Such structures are typically referred to as stretch-dominated, even when designed for compression.) For stretch-dominated structures, yielding of the struts often occurs first due to the fact that buckling is suppressed to higher loads.

Much, if not most, of the earlier work on such materials focused on honeycombs and metallic truss-based structures (such as the octahedral truss [7]), typically fabricated by stamping or folding cell walls and subsequent bonding. Not surprisingly, the mechanics of such structures is similar to that of stochastic foams, with additional consideration of topology constraints that elevate strut stresses and promote yielding. Gibson and Ashby illustrate that the transition from wall buckling to yielding can be described in terms of relative density and yield strength. As a rule of thumb, the strength of metallic structures is buckling dominated below 10% relative density, and yielding dominated above. (Of course, the transition depends strongly on the yield strength of the base material.) While this dissertation touches upon this work, the emphasis is placed on applications where reversibility is a primary objective, and hence buckling-controlled behavior is the principle focus.

The term architected materials is increasingly used for cellular materials with topologies designed to control deformation modes. The emergence of additive manufacturing approaches has dramatically expanded the range of accessible materials and topologies, leading to renewed interest in cellular design and optimization [8]. Arguably, the design and optimization of linear behaviors is well in hand (e.g. [9]); linear, small-deformation solutions for complex topologies can be rapidly generated with conventional finite element analysis, and these combine efficiently with existing optimization frameworks. For most topologies, the small deformation limit is sufficient to accurately predict stiffness and strength, with the latter defined as the onset of yielding or buckling.

In contrast, new insights and numerical schemes are needed to address the design of topologies to control non-linear response, which is the principle focus of this dissertation. While many of the key scaling relationships describing the non-linear response of cellular materials have been elucidated (and summarized in Ashby and Gibson [6]), it is worth noting that there are several important issues that prior work does not address, or does

so only in part.

The first of these issues pertains to post-buckling behavior, which should be contrasted with the onset of buckling. Prior analyses of buckling typically address the critical buckling load using strength-of-materials approaches and assume the load on the structure is constant under subsequent deformation. There has been far less modeling of the changes in stiffness arising during post-buckling deformation, with the exception of empirical approaches to capture the stiffness rise associated with densification. Changes in load capacity at moderate strains can arise from a variety of sources prior to cell collapse, notably non-linear stiffening of struts due to stretching and subsequent buckling of additional struts. Related to this, a second issue that has not be substantially addressed is the role of struts of different sizes; cellular materials often involve cells with multiple struts or wall thicknesses, and little is known about their role in altering buckling behavior. By and large, the existing understanding of cellular material design is based on structures with a single characteristic strut size, and more often than not, a single cell size and/or shape. Finally, a third issue that has received only cursory treatment is the interplay between dynamic loading and the intrinsic viscoelastic response of the strut material; this has important implications for the hysteresis observed during cyclic loading of cellular materials.

The next section outlines the key questions that are addressed in this dissertation and intended to fill in these gaps; additional context and references are included in the chapters that follow.

1.2 Scope, key questions and organization

This work focuses on low density cellular structures made from purely linearly elastic or linearly viscoelastic polymers. The central questions of this dissertation relate to

identifying instances where architected polymeric cellular structures provide benefits over their stochastic counterparts. The work is strongly motivated by the critical need for new insights to tailor non-linear macroscopic response and exploit the power of additive manufacturing.

Specifically, this work addresses the development of cellular configurations that control the onset of buckling *and* post-buckling behaviors, which control the stiffening behaviors observed at moderate strains (under $\sim 50\%$). Emphasis is placed on the strength associated with the initial buckling events, and the post-buckling load path that determines the associated energy stored and dissipated during during cyclic loading. While additive manufacturing enables cellular materials with a broad range of intrinsic properties, the scope here is limited to polymeric materials that exhibit purely linearly elastic or viscoelastic response at small strains (less than 10%). Throughout the dissertation, it is assumed that the struts experience smalls strains that can be appropriately modeled with small strain theory, although it must be emphasized that large configurational changes (i.e. large rotations) are possible and may produce large macroscopic strains.

With this in mind, the key research questions addressed in this dissertation are outlined below, with a brief description of the chapters or sections that contain contributions in each area.

- **What is the influence of strut angles and cell topology on post-buckling behaviors that control the degree of non-linearity?** Struts loaded at shallow angles to the loading direction can exhibit complex transitions during and after buckling (e.g. switching from axial compression to tension), with profound implications for the macroscopic non-linear response. Chapter 3 presents a detailed analytical study of angled struts that can be used to gain insights regarding how these behaviors dictate the degree of non-linearity exhibited by foams. Chapter

4 provides additional insight regarding the role of cell topology on post-buckling behaviors in structures with several cells.

- **What is the role of dynamics during buckling instabilities, and how do they relate to intrinsic material damping in the struts?** Many cellular materials are intended for use in applications that experience dynamic loading, and the interaction between cyclic loading rates and post-buckling response have important implications for energy storage and dissipation. Further, new insight is needed regarding how the viscoelastic properties of the struts influence those behaviors. Chapter 3 addresses these questions and identifies loading regimes where quasi-static hysteresis curves (arising from structural non-linearity) provide acceptable insight into dynamic response.

- **How should mass and topology be adjusted within a unit cell comprising multiple internal struts to control nonlinear response?** Given that buckling is strongly dependent on the free spans of the struts, and that post-buckling behaviors often induce stretch, the question arises as to whether rearranging mass to sub-divide larger cells can achieve improvements in strength and energy storage. Put another way, can tension members be included to improve post-buckling response without compromising strength or absorption on a per unit weight basis? Chapter 4 addresses this by considering a host of different topologies with identical total mass but different mass distributions within strut-based structures.

- **What are efficient frameworks to analyze damping in cellular structures, and how can they be used to quantify the impact of materials selection and topology?** By and large, the damped response of cellular structures is analyzed using heuristic approaches to include damping, creating a critical need to understand how viscoelastic properties of base materials impact cellular response.

Chapter 5 presents a highly efficient framework to predict structural damping in terms of intrinsic viscoelastic properties, and illustrates that significant gains in structural damping are possible through material selection and topology modifications.

- **What are effective numerical approaches to simulate large deflection response and can these be made scalable to address the behavior of complex lattices?** Large displacements of struts relative to the wall thickness induce strongly non-linear behaviors, even though the strains in the struts may be small and the material response is linear elastic. The associated non-linear kinematic relationships create several computational challenges, which are detailed in Chapter 2, along with a detailed study to identify effective numerical parameters (time stepping, damping, imperfections) for accurate simulations. Chapter 6 presents a novel numerical framework based on total energy minimization, with the goal of developing robust numerical techniques to optimize topology for non-linear behavior.

Chapter 2

Numerical methods for elastic truss structures with slender members

2.1 Introduction

The analysis of truss-based structures comprising slender, linearly elastic struts is quite challenging when strut displacements are larger than the strut thickness. Even though the strains in the struts may be small (in comparison to those required to induce material nonlinearity), such problems are strongly non-linear due to the complex kinematic relationships associated with large rotations. These relationships can allow the possibility of multiple equilibrium states, which confound numerical techniques that are based on incremental projections from a base state (i.e. a previously determined equilibrium). The simplest example of this is the buckling of a slender column, where the solution switches from pure axial compression to the buckled state: at the precise instant of buckling, both the uniform compression and buckling solutions are valid.

In a nutshell, incremental approaches that use previous deformation states as the basis for continued deformation often fail to recognize the buckled state as a nearby

solution. The result is a valid equilibrium solution that has greater energy than the alternative, equally valid, equilibrium solution of the buckled state. Such difficulties are compounded significantly when multiple struts are present, since there may be multiple buckling modes, each associated with a distinct pattern of multiple buckled struts.

The principle method to address these difficulties is to include small imperfections to the initial geometry, such that the structure is inherently biased towards a buckling mode with a lower energy state. The central limitations of this technique are that: (i) it is difficult to determine whether or not the imperfections introduced are sufficient to trigger the buckling mode associated with the lowest energy state, and (ii) it is difficult to know a priori whether even small imperfections influence the results beyond merely allowing the numerical algorithm to capture abrupt transitions.

The most common procedure to introduce these imperfections is to conduct an eigenvalue analysis of buckling modes [10]; this analysis uses a first order expansion of the non-linear stiffness matrix to solve for equilibrium solutions associated with a deformed state where non-linear kinematics produce a solution. This procedure yields both an estimate for the macroscopic load associated with the onset of buckling and the shape of the buckled structure. The shape of the structure at the instant of buckling is then used to define the shape of initial imperfections, thereby biasing the numerical solution towards the buckled state. In order for this method to be effective, the structure must exhibit negligible changes in stiffness prior to the buckling load, which is generally tantamount to there being only small changes in geometry prior to the onset of buckling. This condition is not overly restrictive, since many slender structures will be stretch-dominated up until the onset of buckling, while those that are influenced by bending prior to the onset of buckling usually exhibit less abrupt bifurcations that are easier to simulate.

Even with suitable imperfections in hand to bias the solution toward buckling states, it can still be challenging to solve for post-buckling response, due to the abrupt change

in system stiffness. For systems that exhibit non-monotic stiffness (e.g. loads that first decrease with imposed deformation at the onset of buckling, then increase), implicit solution techniques are notoriously unreliable, as stiffness projections can be extremely poor indicators of future behavior.

As a simple illustration, consider the non-monotonic load deflection behavior shown in Figure 2.1 for several different topologies. With sufficient imposed deformation, all four of these beam-based structures encounter configurations with zero macroscopic stiffness. This creates serious headaches for implicit, iterative techniques such as Newton-Raphson; the projected increase in deformation is absurdly large due to the low (or zero) stiffness at the onset of buckling. One recourse is to limit the allowable increment in deformation (commonly referred to as step size); this works well in some instances, such as the structure in Figure 2.1A and the *first* buckling event for the structure in Figure 2.1B. However, abrupt changes in load such as those shown in Figure 2.1C and Figure 2.1D exhibit persistence convergence challenges. This lack of robustness is highly problematic when considering a range of topologies, as they typically must be resolved through on a case-by-case basis. Unfortunately, even modified methods designed to address such behavior, such as the RIKS method [11], are increasingly prone to similar behaviors for structures involving more than a few struts.

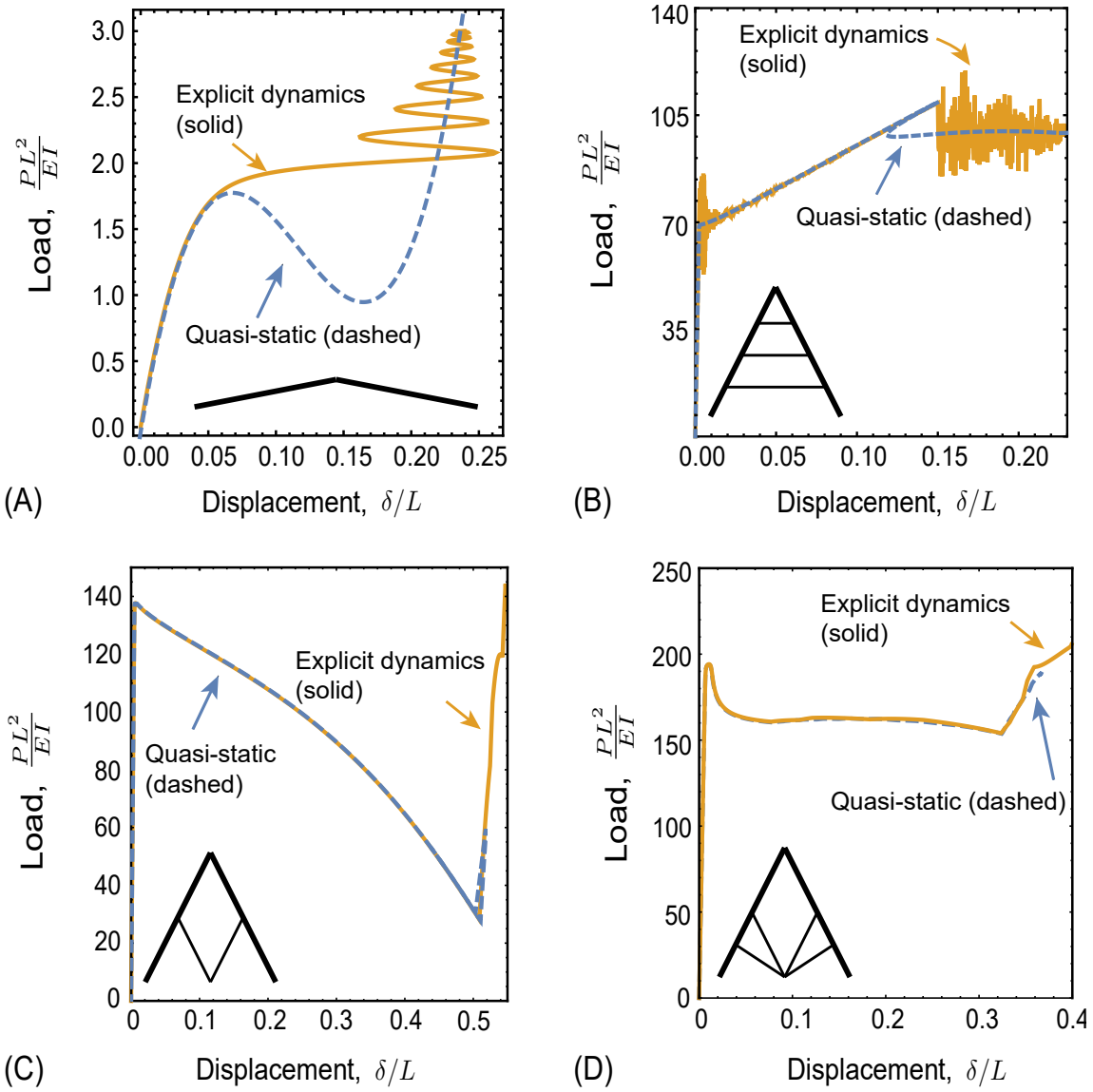

Figure 2.1: Illustrations of load-deflection behavior in structures with slender struts, exhibiting instances of zero-stiffness. The structures all have relative density in the range $\rho/\rho_o = 5 - 7\%$, depending on how mass is distributed. (A) A low-angle 8^o V-structure loaded in force control to illustrate dynamic snap-through behavior. (B) A horizontally braced 60^o V-structure loaded in displacement control. (C) A 60^o V-structure with a single set of inner braces loaded in displacement control. (D) A 60^o V-structure with two sets of inner braces loaded in displacement control.

Due to the lack of robustness of implicit methods, explicit dynamic simulations are generally preferred. In such simulations, the incremental equations of motion include

inertia (acceleration) terms and the structural response is found using integration with respect to time. Imperfections are included to bias the structural response towards buckling modes (as before), but inertia provides a limitation on structural response in instances where the global stiffness measures trend toward zero. It should be noted that while this aids in finding post-buckling solutions, they do not necessarily ensure that buckled states associated with lower energy are tracked.

There are two central considerations when generating such dynamic solutions; first, to capture quasi-static responses, the imposed loading rates must be sufficiently small to prevent dynamic stabilization of buckling modes. This immediately establishes a trade-off between effectiveness and speed, since computational time will scale inversely with time steps. This trade-off is exacerbated by the fact that adaptive time-stepping must be intentionally limited, such that bifurcations are not stepped over. Second, some measure of damping must be included to ensure post-buckling behaviors are not unduly influenced by dynamic oscillations induced by abrupt changes in stiffness. Such oscillations can be very problematic when they persist to later stages of deformation and influence secondary buckling events.

The above considerations dictate that a number of interrelated simulation parameters must be carefully chosen to reliably non-linear response. These include: (i) element size in each strut, (ii) the imposed deformation rate (in this work, defined in terms of imposed boundary velocities), (iii) artificial damping to mitigate post-buckling behaviors, (iv) imperfections, both the number of included eigenmodes and the absolute size of prescribed deviation from nominal geometries. The sections that follow outline the results of a general parameter study designed to identify widely applicable numerical procedures; the central objective is to identify numerical parametesr that are appropriate irrespective of the truss topology. This is critical to enable a systematic design study of structures involving many geometry parameters. The four types of structures used in this numerical

study are shown in Figure 2.2.

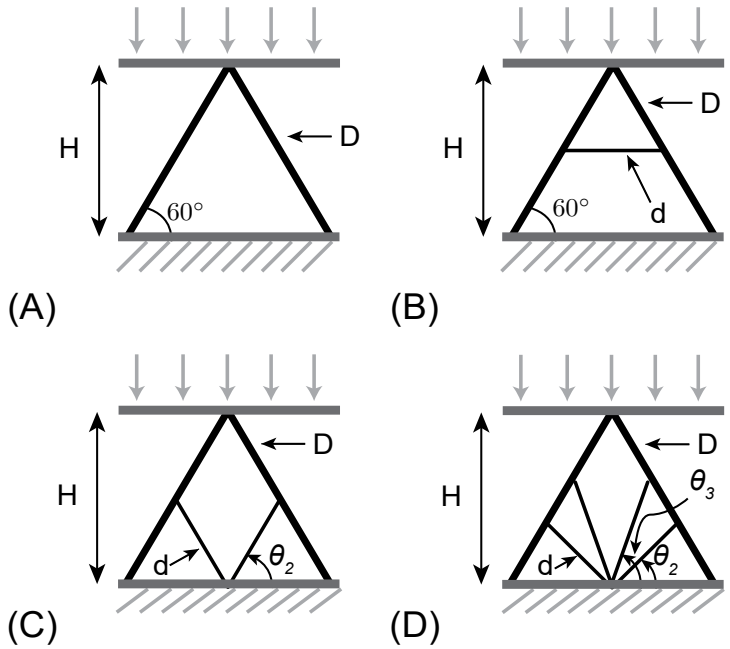

Figure 2.2: Schematic diagrams of the four topology classes used to identify broadly applicable numerical procedures, as well as the design study in Chapter 4: (A) A simple straight-sided arch, used as the comparator for later studies considering the impact of internal bracing. (B) Horizontal brace; cases are run with multiple parallel internal braces, which are defined as the same class. (C) Single angled internal brace structure; the geometry is varied by changing the internal brace angle, but the topology is the same. (D) Double angled internal brace structure; the geometry is varied by changing the internal brace angles, but the topology is the same.

2.2 Convergence metrics and parameter study outline

Two metrics were used to evaluate the sensitivity of the simulation to numerical parameters; the load at the onset of buckling, and the work defined by the area under the load-deflection curve. Figure 2.3 illustrates typical load-deflection results used to compute these metrics, for several different topologies.

To identify the load at the onset of buckling (also referred to herein as strength), the instantaneous macroscopic stiffness of the structure was computed from the load-deflection relationships generated by the simulation. The strength of the structure was defined as the load associated with the first instance where the tangent modulus fell below 1% of the initial stiffness of the structure. Even when bucking-induced oscillations were present, this method proved highly reliable, as in no case did the structure immediately resume a high stiffness value after the onset of strong non-linearity.

To identify the energy stored by the deformed elastic structure, one must choose a relevant macroscopic strain range. Here, we used a single estimate for the macroscopic strain associated with densification, determined by an efficiency parameter that correlates with self-contact. The efficiency parameter is defined as [12]:

$$\eta = \frac{\int_0^{x'} F(\bar{x}) d\bar{x}}{F_{max}|_{x'}} \tag{2.1}$$

$F(\bar{x})$ is the load on the structure for imposed displacement $\bar{x}$; the load-deflection curve is integrated up to a specified maximum displacement; the result is divided by the maximum force encountered up to the same specified displacement. As shown in Figure 2.3, the maximum efficiency hits a peak well after the first buckling instability, at the instance where the stiffness of the structure begins to increase substantially. This point is defined in this context as the densification strain; the reported energy stored is the area under the load-deflection curve up until this point.

Hundreds of spot-checks conducted from thousands of simulations revealed that efficiency parameter always exhibited a local peak, such as those shown in Figure 2.3, just prior to abrupt increases in system stiffness. The densification point, associated with an abrupt increase in local stiffness, consistently correlates with self-contact between members or the platens. No attempt was made to accurately simulate behaviors after

self-contact was initiated; such behaviors are sensitive to contact descriptions. As such, the present study is limited to macroscopic strains in the 30-50% range, as determined via the peak efficiency. Hence, the estimates for energy store in this work is a lower bound.

A detailed numerical study was conducted to quantify the impact of element density, loading rate, damping parameters and imperfections. The goal was to ensure that variations in the metrics from one topology to another (or one geometry to another within a given topology) are not a consequence of poorly chosen numerical parameters. The parametric studies were conducted on four different truss topologies, as shown in Figure 2.2. Each of these structures exhibits non-linear behaviors that are characteristic of that class of topology, e.g. a linear stiffness after buckling (Figure 2.2.A), snap-through behaviors with smooth transitions (Figure 2.2.B), and varying degrees of load drops after buckling (Figure 2.2.C and Figure 2.2.D). In order to avoid interplay between various numerical parameters (e.g. loading rate and damping), an ad hoc set of calculations were first conducted across the parameter space to establish the strength of such interactions.

Using the insights from the ad hoc study of numerical parameters, appropriate ranges were identify for further study. Then, one parameter was held fixed at an extreme value where sensitivity was small (e.g. an extremely slow loading rate) while a second parameter was varied (e.g. the level of damping). This process was repeated for all combinations of mesh density, loading rate, and damping. After identifying regimes where these three parameters played little role, the influence of imperfections was studied. The sections below outline the convergence studies on each individual parameter; the selection of a 'universal' set of numerical parameters is summarized in the final section.

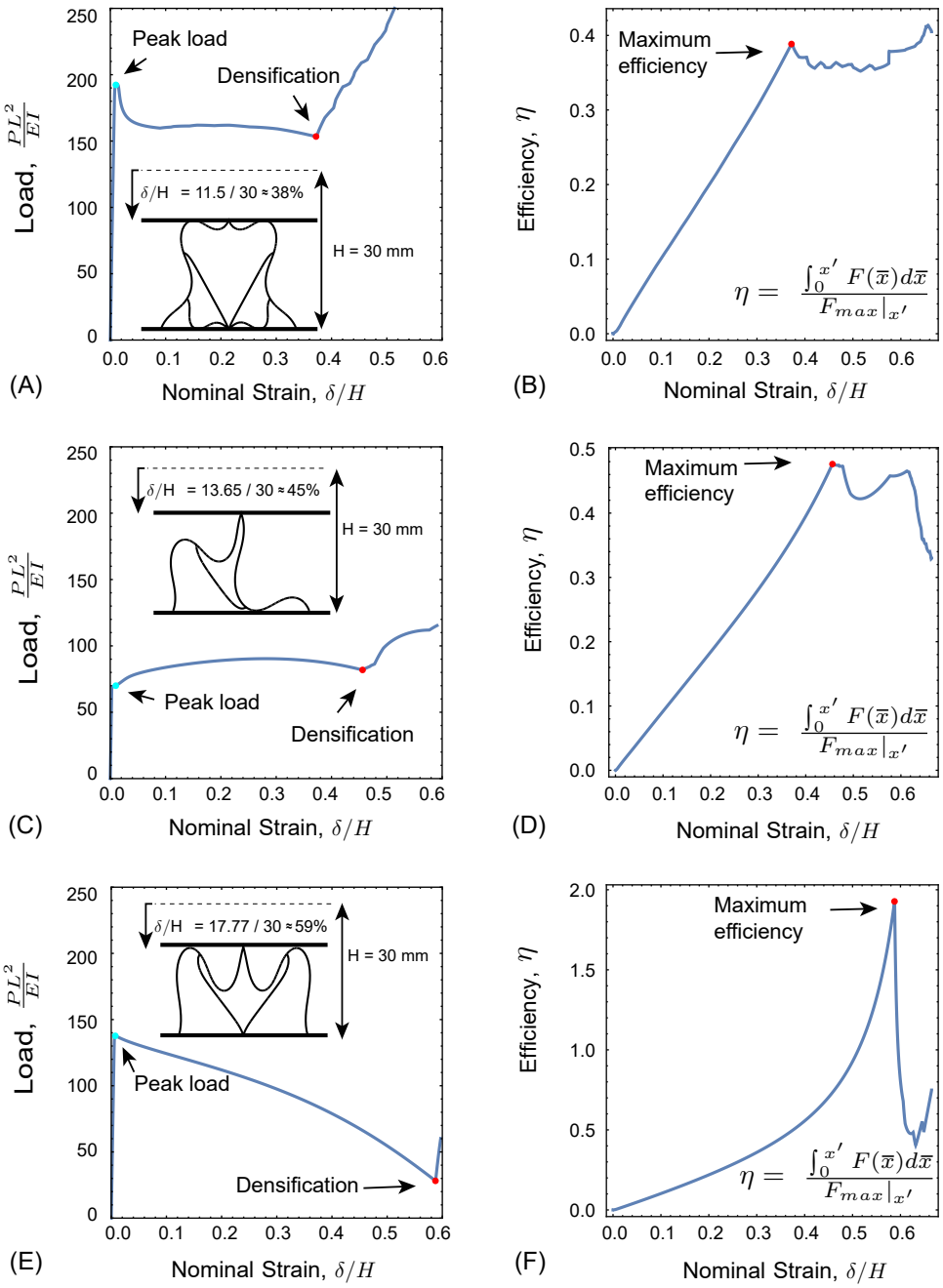

Figure 2.3: Typical force-displacement and efficiency parameter results for three different topologies: (A,B) Double angled internal braces, (C,D) a single horizontal internal brace, (E,F) a single angled internal brace. The densification strain is taken as the first local maximum on the efficiency parameter response shown in (B,D,F).

2.3 Element type and mesh convergence

In this work, explicit dynamic calculations were performed using a Timoshenko-Mindlin element (named B21 in Abaqus Explicit); each element has two nodes, with displacement and rotation degrees of freedom at each node. The element is shear deformable[1], such that plane-sections remain planar but can shear relative to the neutral axis of the beam. The spatial variation of displacements is quadratic, while the strain variations are linear. While the element cross-section is described herein as circular with diameter D, the results are presented in normalized form which renders the shape of the cross-section immaterial.

Mesh convergence studies were conducted on the four classes of structures shown in Figure 2.2; for each structure, the global height of the structure is fixed to 30 millimeters, the diameter of the main struts is fixed to 1 millimeter, and any bracing strut diameter is fixed to 0.5 millimeters. This corresponds to a relative density of $\rho/\rho_o \sim 5\%$. The number of elements in each strut was set by prescribing a fixed element length relative to the strut length; this dictates that longer struts will have a greater number of elements, but the element density per unit length of the struts is constant. The simulations fixed the bottom nodes of the structure (connected to a rigid platens) against all displacements and rotations, while only the horizontal displacement and rotation of the top node are fixed. The top node is then subjected to a vertical downward displacement with the following time-history:

$$\delta = \delta_o \left(1 - \cos \omega t\right) \tag{2.2}$$

where δ_o is the maximum displacement of the simulation, and ω defines the period of time over which the deformation is imposed. (Section 2.3 below discusses the role of the

[1]Shear is likely negligible in such low density structures; however, Bernoulli-Euler elements are not available in Abaqus/Explicit.

loading rate as defined by ω.) The maximum displacement δ_o was chosen to be a large number to ensure densification (i.e. self-contact) is reached.

Figure 2.4 shows the results of the mesh convergence study, plotting the peak load and area under the load-displacement curves (up unto the point of the first local maximum in efficiency) as a function of element size. In this figure, the load is normalized by the scaling factor characteristic of beam bending, i.e. EI/L^2; here, I is the moment of inertia of the struts' cross-section, while L is taken as the full length of one side of the outer struts in the V-structure. Similarly, the energy stored in the compressed structure is normalized by EI/L. Both quantities become independent of the mesh for element sizes less than about twice the strut thickness; this is much smaller than those required when using cubic beam elements, which have cubic displacement interpolation. However, shear deformable elements exhibited more robust convergence for large rotations. The mesh requirements for the double-angle brace structure in Figure 2.4 proved the most demanding of all the structures considered. Convergence was demonstrated for this case for values $\ell_e/L_s < 0.03$ where L_s is the length of the outer main strut. Hence, this limit was to guide the mesh density for all other topologies; in the remainder of the paper, all studies use a characteristic element size of $\ell_e/L_s = 0.024$.

2.4 Effect of loading rate

A parametric study of the effect of loading rate was conducted for the four classes of structures shown in Figure 2.2. The objective of this study was to establish sufficiently low loading rates that did not impact the peak load and energy storage. The central challenge is illustrated in Figure 2.5A, which depicts load-displacement results for a 'V' structure subjected to three different loading periods. For rapid loading associated with a small time to peak load, inertial stabilization of the structure delays on the onset of

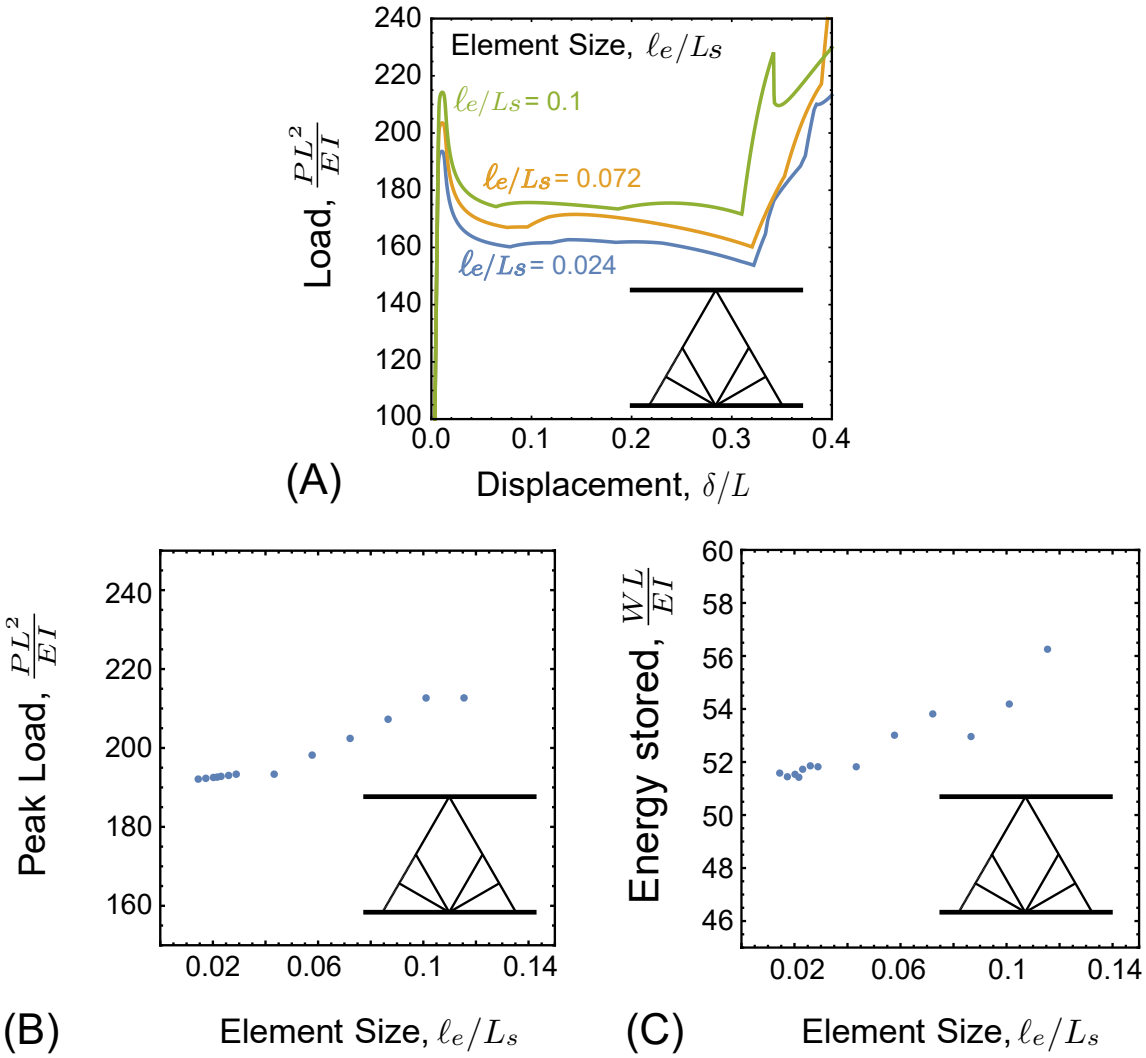

Figure 2.4: (A) Representative load-displacement responses for a two-brace structure with different mesh densities defined by the normalized element length ℓ_e/L_s, where L_s is the length of the outer main strut. Corresponding convergence behavior for both peak load (B) and energy storage (C); both yield converged results under $\ell_e/L_s = 0.03$, so a conservative value of 0.024 is used in subsequent studies.

buckling to higher levels of deformation.

There are two characteristic time-scales associated with deformation of the struts;

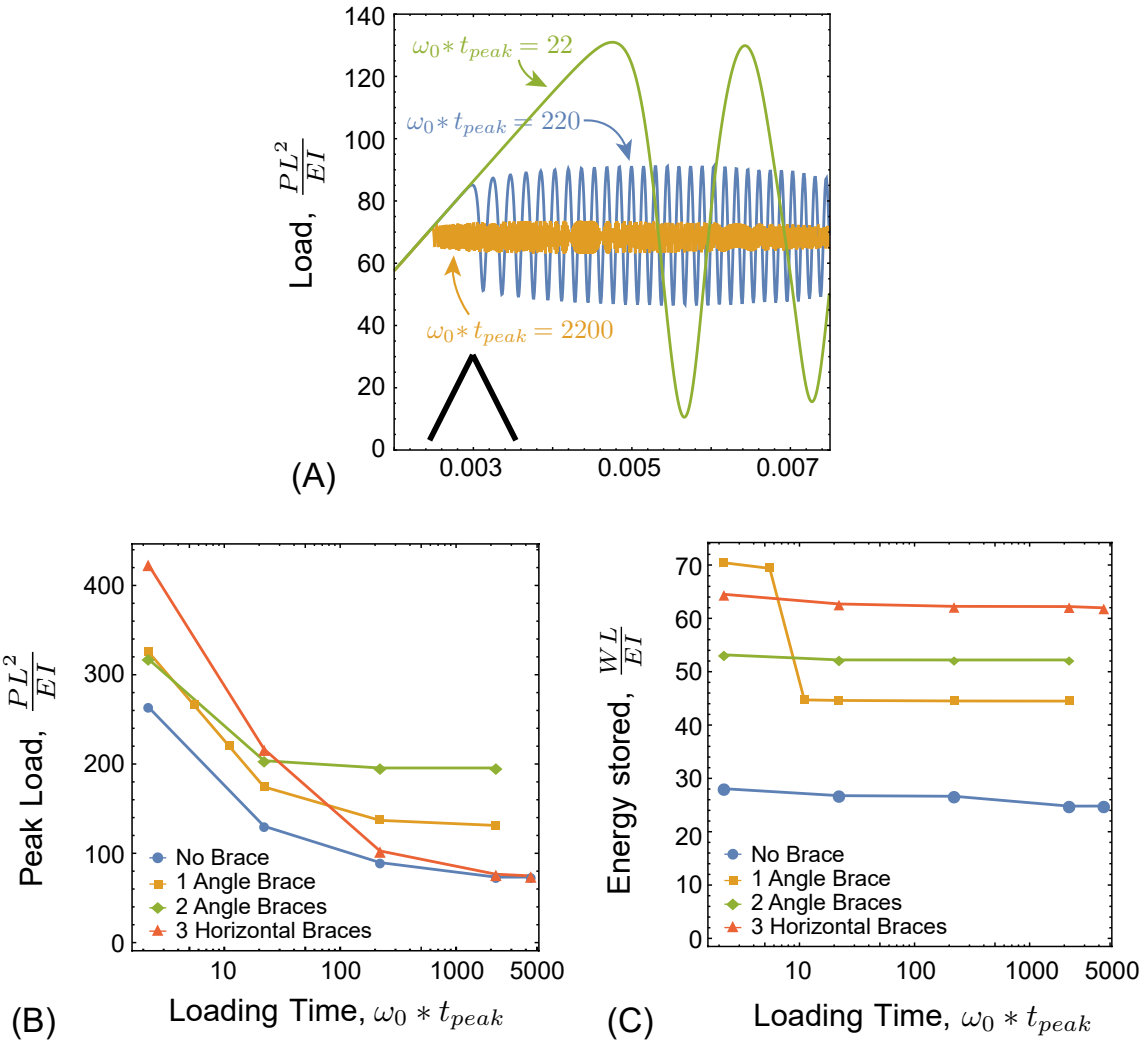

Figure 2.5: (A) Load-displacement curves for three different loading periods with no damping; $\omega_o = \sqrt{EI/\rho AL^4}$ is the characteristic bending frequency of the struts. (B, C) Peak load and energy stored as a function of the loading frequency; for large loading periods (relative to that associated with vibration), the results are independent of loading rate and hence are taken as the quasi-static limit.

the time scale associated with axial deformation is given by:

$$t_{axial} = L\sqrt{\frac{\rho}{E}} \tag{2.3}$$

where ρ is the density of the strut material, E is the elastic modulus and L is the strut

length. This corresponds to the time required for an axial compression pulse to traverse the length of the outer strut. The characteristic time scale associated with bending is given by:

$$t_{bending} = \sqrt{\frac{\rho A L^4}{EI}} = \frac{1}{\omega_o} \tag{2.4}$$

where A is the cross-sectional area of the strut and I is the strut's moment of inertia. This corresponds to the characteristic period of bending vibration modes in the strut; the axial natural frequency is given by the inverse of this scaling time multiplied by a scalar constant that depends on boundary conditions. See Chapters 3 and 5 for additional details. One can anticipate quasi-static behaviors in the limit that $t_{peak} >> t_{bending}$ and $t_{peak} >> t_{axial}$. For slender members, $t_{axial} << t_{bending}$; as such, the present study varied the loading rate in relation to $t_{bending}$. Quasi-static behaviors can be expected when $\omega_o t >> 1$.

It should be pointed out that while the load-displacement response of stable configurations is quasi-static, the behavior during unstable transitions from one state to another can by highly dynamic. This is illustrated by the post-buckling oscillations in Figure 2.5A. The focus here is on ensuring that the peak load reached at the onset of buckling instability is independent of loading rate. As will be illustrated in the next section, even small amounts of damping mitigate the post-buckling oscillations seen in Figure 2.5A.

Figures 2.5B and 2.5C illustrate the effect of loading rate on peak load, and area under the load-displacement curve, respectively. The figures demonstrate that rate-independence is achieved for $\omega_o t_{peak} > 2000$ for all four classes of structures. Note from Figure 2.5A that the frequency of post-buckling oscillations generally depends on the loading rate. However, the area under the curve is much less sensitive, regardless of the

nature of post-buckling vibrations. This is because the area under such oscillations is virtual identical to the area under the time-averaged response, i.e. the oscillations above and below the mean cancel one another. For all subsequent calculations, the time to peak load is set to $\omega_o t_{peak} = 2200$.

2.5 Effect of damping

As shown in Figures 2.1, 2.5 and 2.6, instabilities triggered by strut buckling introduce oscillations associated with the release of strain energy that can occur during the transition from one deformed state to another. Such oscillations are entirely plausible for highly elastic materials; however, even small amounts of internal damping will significantly reduce their appearance. One can easily anticipate that polymer materials motivating this work will have at least some damping to suppress such behavior. Here, a simple phenomenological damping model is utilized merely to produce lightly damped structures that minimize the role of dynamic oscillations on post-buckling response. This phenomenological description is used for the design study in Chapter 4. Realistic constitutive laws with intrinsic damping are addressed in Chapter 5.

The phenomenological damping model used in this convergence study is the widely-adopted 'proportional damping' description, which introduces velocity-dependent dissipative terms into the dynamic equations of motion. That is, the governing equations are modified to be of the form:

$$[M]\left[\ddot{Q}\right] + [C]\left[\dot{Q}\right] + [K]\,[Q] = [F(t)] \tag{2.5}$$

where $[Q]$ are the generalized nodal variables resulting from the finite element discretization, $[M]$ is the generalized mass matrix, $[K]$ is the generalized stiffness matrix, and

$[F(t)]$ is the generalized force vector. The damping matrix $[C]$ is expressed in terms of the mass and stiffness matrices:

$$[C] = \alpha\,[M] + \beta\,[K] \tag{2.6}$$

where α and β are phenomenological damping constants. Mechanistically, the constant α is consistent with damping introduced by fluids surrounding the structure, while β is consistent with internal viscoelasticity arising from a single Maxwell model. It can be shown that α is most impactful at low frequencies, while β is impactful at high frequencies [13]. As β typically plays a more significant role in elevating viscous forces, the present study sets $\beta = 0$ and modulates the mass damping parameter α. In Abaqus Explicit, α is scaled by the inverse of the natural frequency ($\alpha \propto 1/\omega_o$).

Figure 2.6 illustrates the impact of various damping levels on the four classes of structures shown in Figure 2.2. Zero damping enables large, high frequency oscillations such as those shown in Figure 2.6A. As damping is introduced, these oscillations are mitigated, as shown in Figure 2.6B; high levels of damping are also shown, which can delay the onset of buckling instabilities and produce higher peak loads that are likely not representative of lightly-damped structures. The results in Figures 2.7A and 2.7B show the influence of the damping parameter α on the peak load and area under the load-displacement curve, respectively. It is clear that low levels of damping, with $\alpha/\omega_o < 0.5$, have a negligible impact on these quantities, while severely curtailing post-buckling behaviors (as seen in Figure 2.6). Hence, $\alpha/\omega_o = 0.45$ is chosen for the study of truss topology presented in Chapter 4.

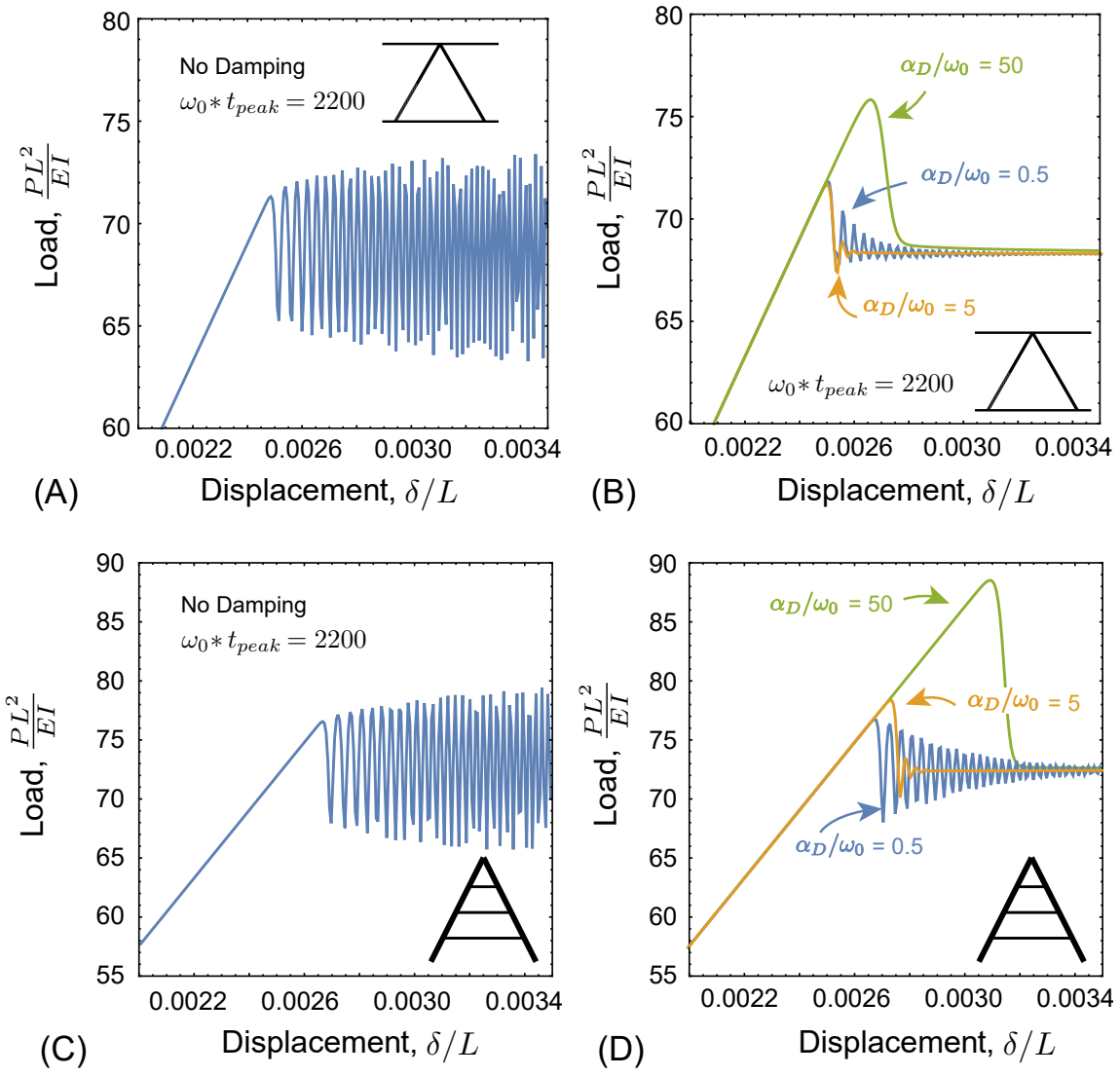

Figure 2.6: Illustrations of the effect of damping on load-deflection response: (A) a simple "V" structure with no damping, (B) a simple "V" structure with several damping levels, (C) a horizontally braced structure with no damping, and (D) a horizontally braced structure with several damping levels. Damping levels that completely suppress post-buckling vibrations can also artificially elevate the buckling load.

2.6 Effect of imperfections

As described in Section 2.1, deviations from the nominal geometry (i.e. imperfections) can be effective in ensuring that incremental methods capture relevant buckling

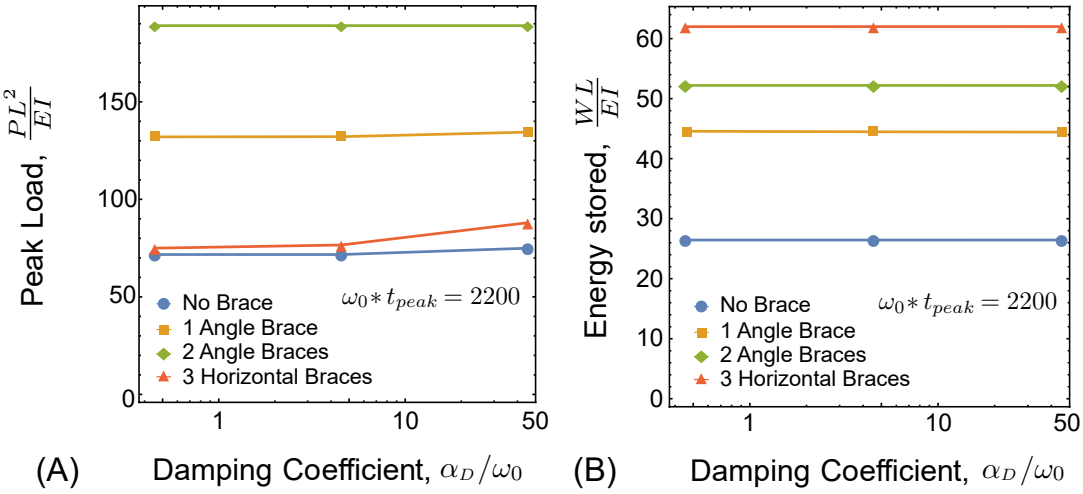

Figure 2.7: Peak load and energy stored versus the damping parameter used to suppress post-buckling oscillations, illustrating that small levels of damping have little influence on the metrics used to test convergence. The scaling frequency is $\omega_o = \sqrt{EI/\rho AL^4}$.

modes. Imperfections are generally based on the eigenmodes of the system, i.e. states associated with a first-order expansion of the non-linear stiffness matrix. For truss structures involving more than a couple members, post-buckling behaviors can be influenced by higher order eigenmodes that occur at larger displacements than the first buckling event. This complicates the selection of eigenmodes to be included and their associated amplitudes. Figure 2.8 illustrates various buckling modes computed from an eigenvalue analysis that are used as the basis for defining imperfections; note that the amplitude of deformation includes arbitrary scaling to highlight the deformed shape.

The results shown in Figure 2.9 illustrate the role of imperfections, by plotting the peak load and area under the load-displacement curve for various types of imperfections for the four classes of structures shown in Figure 2.2. In Figure 2.9A, the number of superposed eigenmodes is fixed at seven (i.e. modes 1-7 added together), while the amplitude of the imperfection is varied relative to the strut size. In this study, the contribution of each eigenmode to the total imperfection (i.e. the amplitude for each

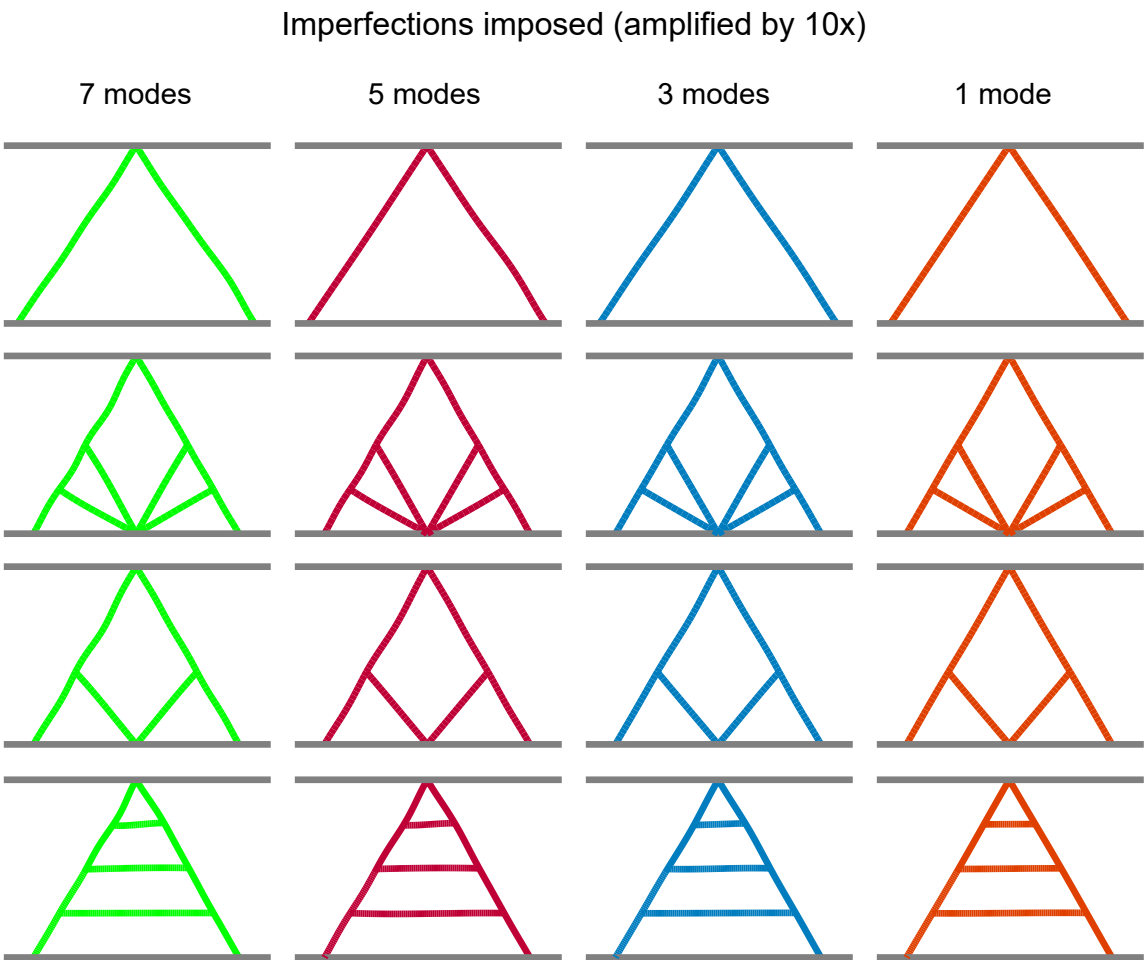

Figure 2.8: Examples of truss topologies with imperfections based on superposition of buckling modes; actual deviations from nominal geometry are slight, and increase slightly as higher buckling modes are included.

eigenmode) is equal.

For small imperfections, the peak load is relatively unaffected by their magnitude. It is worth emphasizing that setting the imperfection size to zero leads to inconsistent results, with some structures exhibiting dramatic increases in peak load because the first buckling load is stepped over during the incremental solution. At large imperfection sizes, the peak load decreases due to the increase in bending compliance associated with macroscopic changes to the shape of the structure. Imperfections that lead to changes in bending

compliance are generally observable in the geometry without the scaling amplification shown in Figure 2.8. Figure 2.9B shows the impact of imperfection size on the area under the load-displacement curve. While this quantity is relatively insensitive to imperfection size for three of the four structures, the case of a V structure with two sets of angled braces shows that some structures can be strongly influenced by the imperfection size.

In Figure 2.9C, the size of the imperfections is held fixed, while the number of eigenmodes used to define imperfection shape is varied (e.g. 3 eigenmodes indicates the first 3 eigenmodes superposed to create the initial imperfection). Note that for certain structures, the peak loads obtained with higher order imperfections are slightly lower than those with just an imperfection based on the lowest eigenmode. This behavior is even more pronounced in the energy stored, as seen in Figure 2.9D; a dramatic drop is observed when at least two modes are included.

From the results in Figures 2.9C and 2.9D, it is clear that including at least the first three eigenmodes will produce results that are not influenced by the specific choice of included modes. The results in Figures 2.9A and 2.9B show that the selection of imperfection amplitude is more nuanced; apparently, there is a lower limit required to achieve consistent results (see the results for the V-structure with two sets of angled struts in Figure 2.9B), as well as an upper limit to ensure the imperfections do not introduce significant bending compliance (see all cases in Figure 2.9A). For the broad topology discussed in Chapter 4, the first seven eigenmodes are included with an amplitude of 1% of the diameter.

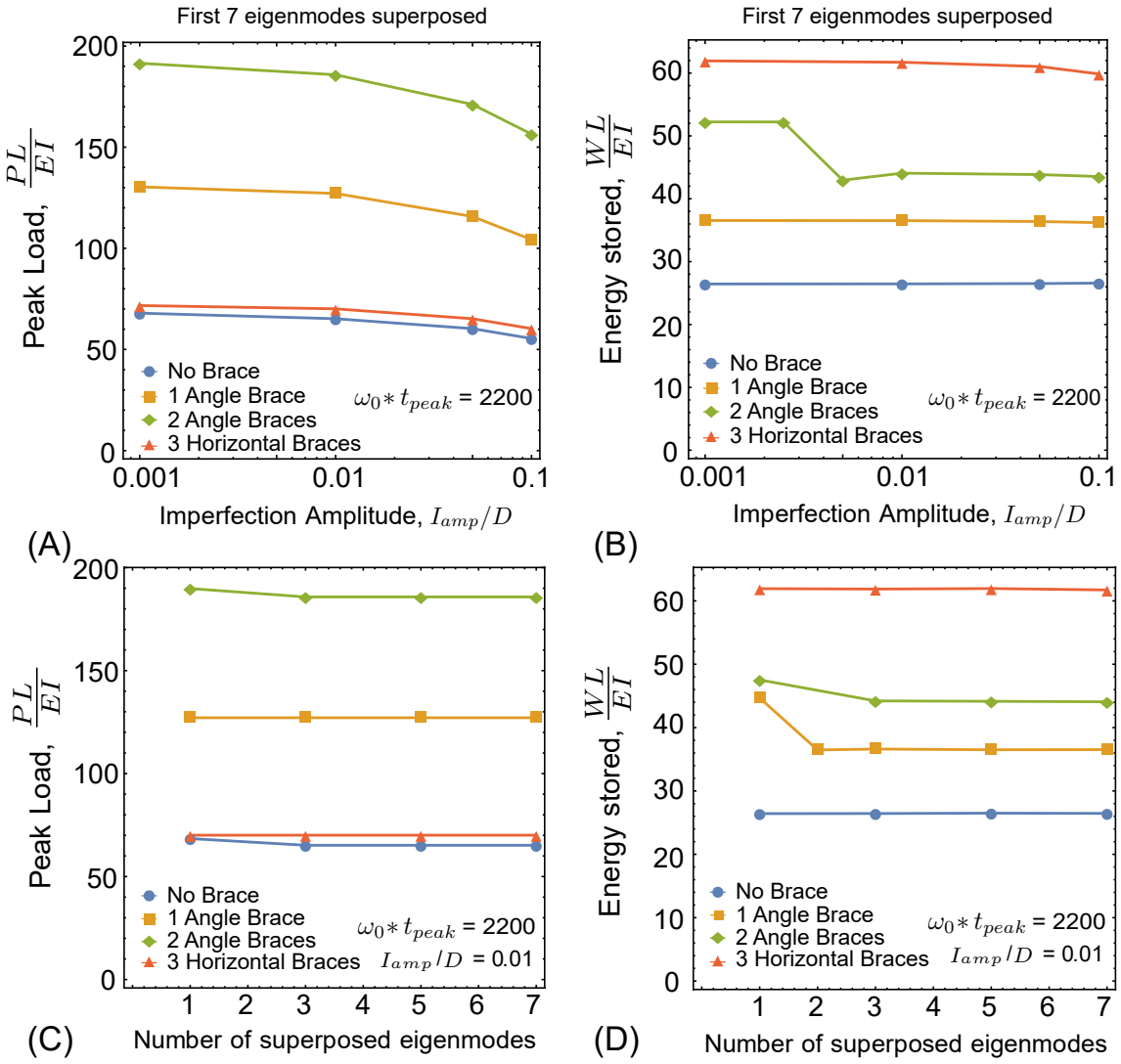

Figure 2.9: A summary of the impact of imperfections on peak load and energy storage, including both amplitude (A and B) and number eigenmodes (C and D). Results for all four truss topologies are shown. The loading rate is defined by the period of $\omega_o t_{peak} = 2200$. In the amplitude study in A and B, the first seven eigenmodes are added to the structure as an initial imperfection and the imperfection amplitude is varied relative to the main strut diameter. For the eigenmode study in C and D, the imperfection amplitude is fixed to be 1% of the main strut diameter and the number of eigenmodes is varied.

2.7 Summary of numerical parameters used in subsequent studies

In summary, the mesh size required for convergent simulations is assumed to be independent of the structural topology, and corresponds roughly to the strut thickness when using Timoshenko-Mindlin elements. Similarly, the minimum loading time interval required to avoid inertial effects (prior to buckling) is also relatively independent of the structural topology, and corresponds roughly to 10^3 times the temporal scale associated with bending vibrations. (The time scale for axial waves is much smaller, and is therefore satisfied by meeting the limitation associated with bending.) With regards to damping, the results will be relatively insensitive to the mass damping parameter when $\alpha/\omega_0 \leq 0.5$; structural oscillations during unstable transitions in deformed state are damped out in less than ten or so oscillations when the damping is set near this limit. In contrast to these three parameters, the role of imperfections is more nuanced. Studies on the four topologies considered in this chapter have shown that it is most effective to include at least three eigenmodes with a amplitude of 1% of the strut diameter; this avoids macroscale imperfections that alter the initial stiffness, and ensures that the lowest buckling loads are obtained during incremental dynamic solutions. A summary table of the parameters chosen for later simulations, and the associated scaling factors, is provided in Table 2.1.

Parameter	**Normalized form**	**Value**
Element size	ℓ_e/L_s	0.024
Load rate	$\omega_0 t_{peak}$	2200
Damping coefficient	α_D/ω_0	0.45
Imperfection amplitude	A_{imp}/D	0.01
Number of eigenmodes	—	7

Table 2.1: Summary of parameters that produce consistent results for the four topologies shown in Figure 2.1 and used as the basis for the design study in Chapter 4.

Chapter 3

Post-buckling and dynamic response of angled struts in elastic lattices

3.1 Introduction

The emergence of three-dimensional fabrication techniques at length-scales spanning from the nanoscale to the macroscale has renewed interest in design of cellular solids. Over the last decade or so, significant attention has been placed on developing novel structures that specifically exploit buckling of struts or cell walls, notably metamaterials that exhibit hysteretic damping or stable changes in configuration that alter macroscale mechanical, optical or acoustic properties. [For examples, see [8, 14–27].] While cellular topologies to achieve 'programmable' non-linear responses are highly varied, a unifying design element is the use of struts that lie at angle to the principle loading direction, such as those shown in Figure 3.1A.

With suitable lateral constraint, angled struts experience 'snap-through' during compressive loading due to buckling instabilities arising from non-linear kinematic motions, as shown in Figures 3.1 and 3.2. Such instabilities are highly sensitive to the angle of

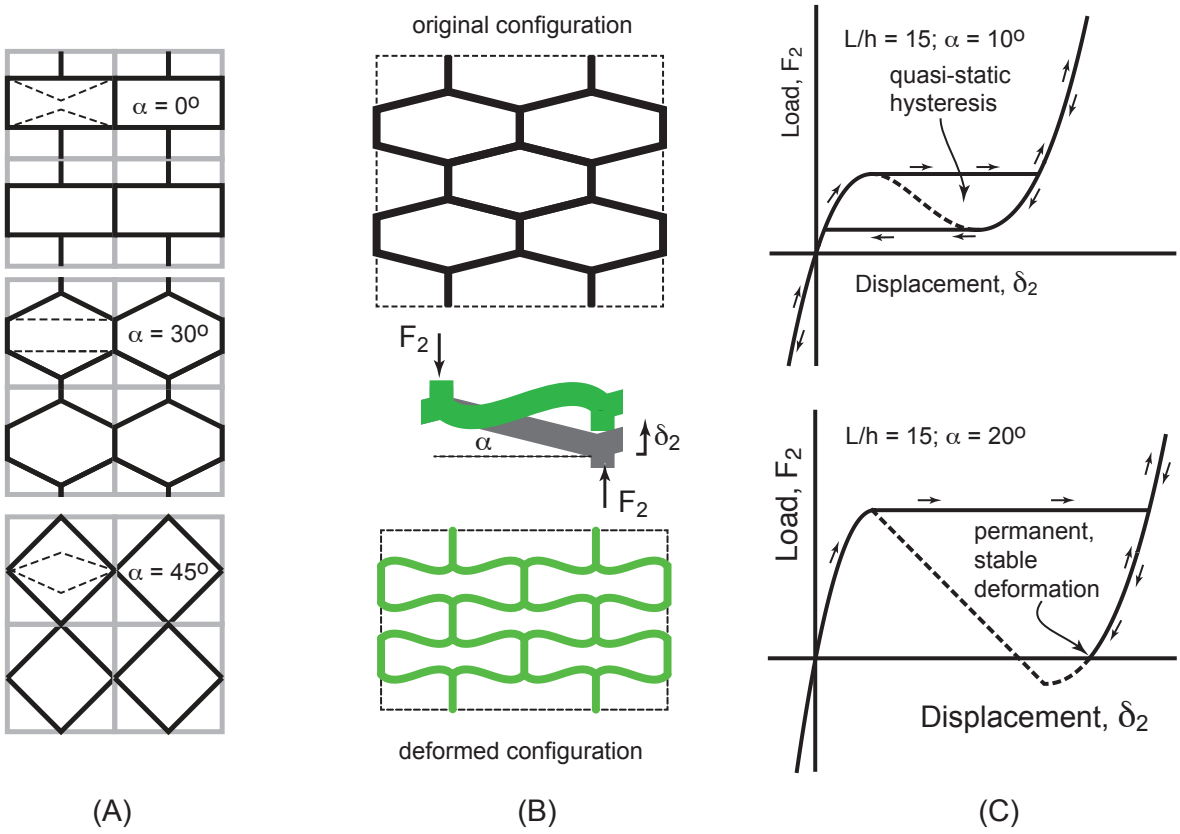

Figure 3.1: (A) Lattices with angled struts; the focus here is on buckling behavior of struts under various states of biaxial straining without shear. (B) Original and deformed shapes when the lattice is constrained against expansion and the angled struts experience snap-through. (C) Load-deflection curves for two different strut angles when constrained against lateral expansion, showing both reversible (top) and irreversible (bottom) snap-through.

the struts and their length-to-thickness (aspect) ratio L/h; this is illustrated in Figure 3.2 with theoretical predictions described in the remainder of the paper. The force-displacement response in Figure 3.2B for $L/h = 15$ and $L/h = 20$ exhibit an unstable linear unloading portion (during load control); this straight segment is a consequence of imperfections in the strut. As shown in Figure 3.2C, significant forces are generated perpendicular to the loading direction.

Prior treatments of snap-through phenomena (and structures capable of exploiting related behaviors) are extensive [e.g. [28–44]] and highlight many salient aspects of design, analysis and performance. On the one hand, previous treatments have established a solid foundation to identify relevant geometries and predict the behaviors shown in Figures 3.1 and 3.2. On the other, a comprehensive framework has not been presented that spans the entire design space and enables the evaluation of critical design parameters, such as the influence of biaxial loading, peak strains in the members governing failure, and expected hysteresis during cyclic loading. To address the need for a flexible design tool that covers all aspects of non-linear response, we present a comprehensive analytical solution for the angled struts shown in Figure 3.1. This solution encompasses most (if not the entirety) of analytical approximations and numerical simulations in prior work, and provides the following new capabilities.

First, the solution addresses lateral constraints (in the horizontal direction of Figure 3.1) and allows one to identify combinations of geometry and biaxial strain states that lead to instabilities. Second, the solution provides estimates for strains in the struts after snap-through, which are critical to assessing strut failures and the cyclic durability of bistable lattices. Third, the analytical solution accounts for imperfections (i.e. slightly curved struts), allowing predictions of the defect sensitivity of various topologies. Fourth, the analytical solution can be used with superposition to predict the response of different cell types used in parallel, facilitating the conceptual design of novel lattices to achieve

specific non-linear responses. Fifth and finally, it provides insight into strut deformations that can be exploited in dynamics models; this enables an efficient, single degree-of-freedom dynamics model that can be used to evaluate the dynamics of instabilities, angled struts utilized in series (as opposed to parallel), and hysteretic losses during cyclic loading.

It should be emphasized that the merit of the present analysis centers on its bandwidth (in spanning all predicted various behaviors considered elsewhere), efficiency (complex numerical solutions are avoided) and the extension to dynamic behaviors, notably damping during cyclic loading. The efficiency of the framework is particularly powerful, as it enables rapid parametric studies to identify desirable regions of the design space, including those that avoid failures and/or involve the cooperative movement of multiple struts. Put simply, the present analysis should be viewed as a comprehensive design tool that provides rapid assessment of various architected topologies, and in certain contexts, stochastic foams. As such, the model should find rich utility in guiding the development of programmable materials.

This perspective is substantiated by numerous outcomes of the model that have not been previously elucidated. First, combinations of strut aspect ratio and strut angle that lead to reversible snap through (a requirement of exploiting cyclic hysteresis arising from non-linearity) are closely correlated with relative density. E.g., for rhombic lattices, reversible snap-through occurs only for relative densities in the range $0.25 < \bar{\rho} < 0.4$; the corresponding relative density range for other topologies are easily achieved from analysis of different unit cells. Together with well-established scaling of lattices, this sets limits on the achievable stiffness and strength of such lattices. Second, reversible snap-through regimes must tolerate strains of 1-10%; this sets design limits on geometry and/or materials selection. Third, the models allow for rapid assessments of dynamic behaviors during snap-through: notably, peak strains associated with overshoot and the dissipated

work under cyclic loading. The results reveal that dramatic increases in damping are possible even in scenarios that do not achieve snap-through. Finally, lattices that exploit struts at different angles hold promise for improving strength and energy absorption; combining cell based struts with different characteristic angles offers increased stiffness, strength, and post-buckling stability.

The solutions presented in this work, and illustrations of its utility, draw inspiration from three substantial bodies of literature whose seminal contributions have launched interest in such structures. Following Williams' landmark treatment of an angle toggle switch [28], there have been numerous treatments of bistability in beam-like sensors and switches, notably in the MEMS community [e.g. [41, 42, 45–52]]. Similarly, the consideration of large deformation in frames (notably for space structures) have established powerful numerical techniques to consider more complex structures [e.g. [29–40, 43]]. Finally, over the last decade, there have been numerous specific implementations of snap-through structures, particularly those enabled by advances in three-dimensional printing [e.g. [21–24, 27]]. These works highlight many (but not all) aspects of the models presented here.

3.2 Governing equations and solutions for moderate rotations

The analysis presented here describes the response of one of the angled struts in Figure 3.3A, with (X_1, X_2) defining the global coordinate system. The struts are assumed to have an initial curvature, defined by $\kappa_o = 1/R$ in Figure 3.3B; in the limit that $\kappa_o \to 0$, the strut is perfectly straight. In what follows, we adopt a Kelvin-Voigt viscoelastic model ($\sigma = E\epsilon + \eta\dot{\epsilon}$) to gain insight regarding the nature of hysteretic losses relative to intrinsic

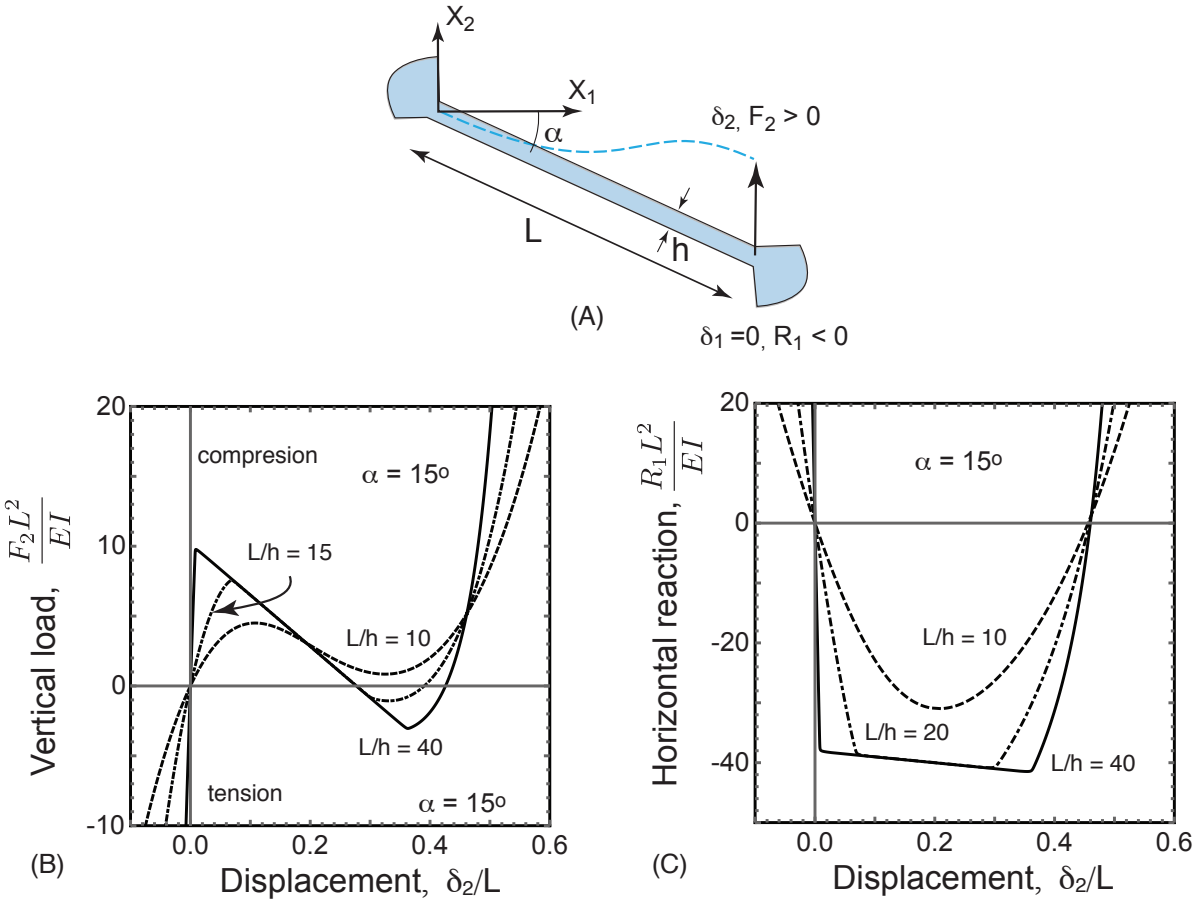

Figure 3.2: Typical plane strain ($\delta_1 = 0$) behavior of angled struts, loaded in compression: (A) the strut geometry, indicating vertical positive forces that put the strut into axial compression, (B) representative load-displacement curves for a shallow angle and several slenderness ratios, (C) the reaction forces in the horizontal direction.

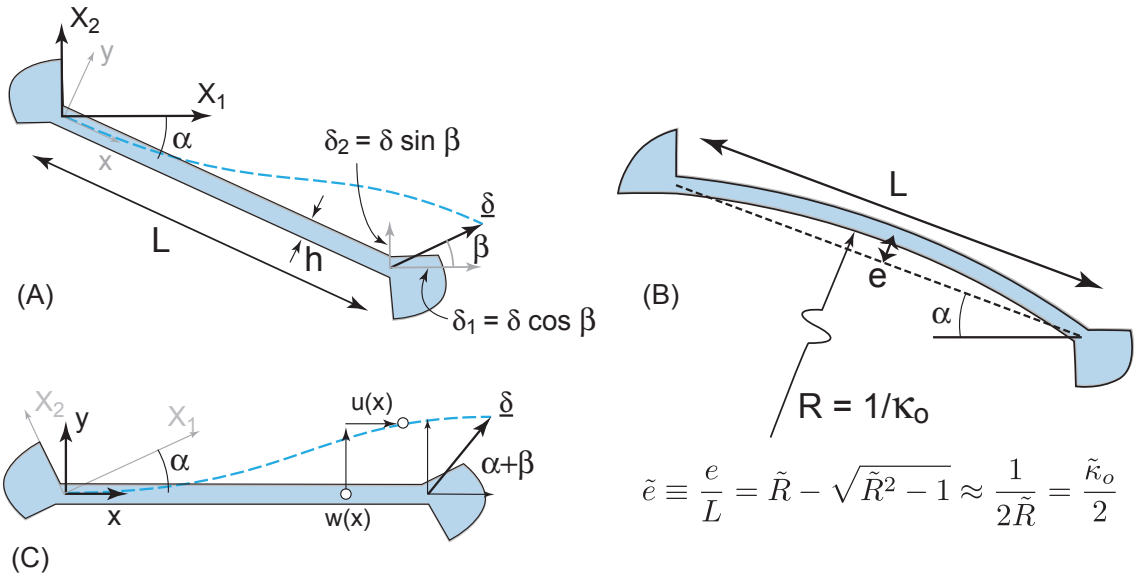

$$\tilde{e} \equiv \frac{e}{L} = \tilde{R} - \sqrt{\tilde{R}^2 - 1} \approx \frac{1}{2\tilde{R}} = \frac{\tilde{\kappa}_o}{2}$$

Figure 3.3: (A) Global coordinates and geometric variables used in the non-linear analysis that invokes moderate rotation theory. (B) Illustration of strut curvature, as characterized by the dimensionless radius of curvature, $\tilde{kappa}_o = \kappa_o/L$, which can be related to the eccentricity of the midspan. (C) Local coordinates and variables used to solve for the response.

material damping. Throughout the following, (x, y) refers to the local coordinate system aligned with the beam, as shown in Figure 3.3C.

Moderate rotation theory is utilized that invokes the approximation that $\sin\theta \simeq \theta$, where θ is the angle of an infinitesimal line segment in the deformed state relative to the original $x-$axis. This approximation is reasonably accurate for $\theta <\sim 30^o$. As a rule of thumb, the analysis presented here can be expected to be accurate up until $\delta \sin(\alpha + \beta) \approx 0.3$, where δ is the magnitude of the deflection of one anchor point relative to the other, and β defines the direction of loading with respect to the global X_1-axis. This encompasses a surprisingly large range of behavior (as quantified in Section 5.1), including virtually all bistable solutions.

3.2.1 Coupled non-linear dynamic governing equations

Assuming moderate rotations and that plane sections remain plane, the strain in the beam is given by:

$$\epsilon(x,y,t) = u'(x,t) + \frac{1}{2}\left[w'(x,t)\right]^2 + \kappa_o w(x,t) - y \cdot w''(x,t) \tag{3.1}$$

$$= \epsilon_o(x,t) - y \cdot w''(x,t) \tag{3.2}$$

where $u(x,t)$ is the axial displacement of the strut's neutral axis, $w(x,t)$ is the displacement perpendicular to the neutral axis, y is the distance from the neutral axis of the strut, and primes denote differentiation with respect to x. In eqn. 3.2, the stretching of the centerline is re-defined as ϵ_o, i.e. the sum of the first three terms in eqn. 3.1, while the last term represents the bending strain.

The governing equations can be derived from the principle of virtual work, which dictates the difference of internal and external virtual work is:

$$\begin{aligned}\delta W_{int} - \delta W_{ext} &= \int_0^L E\left[\int_A \left(\epsilon_o - y\cdot w''\right)\left(\delta u' + w'\delta w' + \kappa_o \delta w - \delta w'' y\right) dA\right] dx \\ &+ \int_0^L \eta\left[\int_A \left(\dot{\epsilon}_o - \dot{w}'' y\right)\left(\delta u' + w'\delta w' + \kappa_o \delta w - \delta w'' y\right) dA\right] dx \\ &+ \int_0^L \rho A \ddot{w}\delta w dx + \int_0^L \rho A \ddot{u}\delta u dx - F_x \delta u(L) - F_y \delta w(L) = 0 \end{aligned} \tag{3.3}$$

where δu and δw are virtual displacements, $F_{x,y}$ are the applied forces referenced to the local coordinate system, and the axial and transverse accelerations are given by $\ddot{u}$ and $\ddot{w}$, respectively. (See Figure 3.3.) Here, rotary inertia is neglected, as its virtual work contribution is negligible when $(h/L)^2 << 1$ for deflections on the order of L. After expanding, performing the usual integration by parts and collecting like terms, eqn. 3.3

leads to:

$$EA\left[u' + \frac{1}{2}(w')^2 + \kappa_o w + \bar{\eta}\left(\dot{u}' + w'\dot{w}' + \kappa_o \dot{w}\right)\right]' + \rho A\ddot{u} = 0 \quad (3.4)$$

$$\rho A\ddot{w} + EI\left[w'''' + \bar{\eta}\dot{w}''''\right]$$

$$-EA\left[\left(u' + \frac{1}{2}(w')^2 + \kappa_o w + \bar{\eta}\left(\dot{u}' + w'\dot{w}' + \kappa_o \dot{w}\right)\right)w'\right]' + EAk_o\epsilon_o = 0 \quad (3.5)$$

where I is the moment of inertia of the strut and $\bar{\eta} = \eta/E$. The boundary terms arising from the integration dictate the reaction forces (for imposed displacements) or the boundary conditions (for imposed forces). For the present case, the boundary condition at $x = L$ appears as:

$$\left[EA\left(u'(L) + \kappa_o w(L) + \bar{\eta}\dot{u}'(L) + \bar{\eta}\kappa_o \dot{w}(L)\right) - F_x\right]\delta u(L) = 0 \quad (3.6)$$

$$EI\left[w'''(L) + \bar{\eta}I\dot{w}'''(L) + F_y\right]\delta w(L) = 0 \quad (3.7)$$

In what follows, we use the following normalizations: $U = u/L$, $W = w/L$, $\bar{x} = x/L$, and $\bar{h} = h/L$. The characteristic inertial time scale and characteristic free vibration frequency are given by:

$$t_o = \sqrt{\frac{\rho AL^4}{EI}}; \quad \omega_o = \frac{1}{t_o} = \sqrt{\frac{EI}{\rho AL^4}} \quad (3.8)$$

These are simply the scalings controlling the vibration characteristics of the structure; the actual natural frequency will be proportional to ω_o through a scalar factor that depends on geometry, as described below. Defining normalized time as $\tau = t/t_o = \omega_o t$,

the governing equations become:

$$\left[\left(U' + \frac{1}{2}\left(W'\right)^2 + \tilde{\kappa}_o W\right) + \tilde{\eta}\left(\dot{U}' + W'\dot{W}' + \tilde{\kappa}_o \dot{W}\right)\right]' + \frac{\bar{h}^2}{12}\ddot{U} = 0 \quad (3.9)$$

$$\ddot{W} + \left[W'''' + \tilde{\eta}\dot{W}''''\right]$$

$$-\frac{12}{\bar{h}^2}\left[\left(U' + \frac{1}{2}\left(W'\right)^2 + \tilde{\kappa}_o W + \tilde{\eta}\left(\dot{U}' + W'\dot{W}'\right) + \tilde{\kappa}_o \dot{W}\right) W'\right]' + \frac{12}{\bar{h}^2}\kappa_o \epsilon_o = 0 \quad (3.10)$$

with

$$\tilde{\eta} = \bar{\eta}\sqrt{\frac{EI}{\rho A L^4}}. \quad (3.11)$$

The normalized boundary conditions for a clamped end condition at $\bar{x} = 1$ are given by:

$$\tilde{F}_x(\tau) = \frac{L^2 F_x(\tau)}{EI} = U'(1) + \tilde{\kappa}_o W(1) + \tilde{\eta}\left[\dot{U}'(1) + \tilde{\kappa}_o \dot{W}(1)\right] \quad (3.12)$$

$$\tilde{F}_y(\tau) = \frac{L^2 F_y(\tau)}{EI} = -W'''(1) - \tilde{\eta}\dot{W}'''(1) \quad (3.13)$$

When displacements are applied, the above forces represent the corresponding reaction forces resulting from the applied displacements. The relationship between the reaction force in the local and global coordinates are easily found via a simple coordinate transformation.

3.2.2 Quasi-static solutions

For quasi-static conditions, the time-derivative terms in the dynamic governing equations can be neglected; in this case, the axial equilibrium equation given as eqn. 3.9 implies that the strain at the neutral axis is constant, i.e.:

$$U' + \frac{1}{2}\left(W'\right)^2 + \tilde{\kappa}_o W = \epsilon_o \quad (3.14)$$

where ϵ_o is a parameter to be determined. Here, we re-define the unknown parameter describing strain at the neutral axis:

$$\Lambda = \sqrt{\frac{12\epsilon_o^{c,t}}{\bar{h}^2}} \tag{3.15}$$

with $\epsilon_o^{c,t}$ representing the *magnitude* of axial strain at the neutral axis. With the sign of this strain taken into account in the definition of Λ, the remaining governing equation, eqn. 3.10, in the quasi-static limit becomes:

$$W'''' \mp \Lambda^2 W'' \pm \tilde{\kappa}_o W = 0; \quad W(0) = W'(0) = W'(1) = 0; \quad W(1) = \Delta \sin(\alpha + \beta) \tag{3.16}$$

where Δ is the displacement of the end of the beam. Hence, the top signs are used if the axial strain $\epsilon_o = \epsilon_o^t > 0$ and the bottom signs are used if $-\epsilon_o^c = \epsilon_o < 0$ (i.e. the neutral axis of the strut is in compression). The final piece of the puzzle is to determine Λ; integrating eqn. 3.14 along the length of the beam, one obtains:

$$\Delta \cos(\alpha + \beta) + \int_0^1 \left(\tilde{\kappa}_o W + \frac{1}{2} [W']^2 \right) d\bar{x} = \pm \frac{\bar{h}^2}{12} \Lambda^2 \tag{3.17}$$

where the geometric relationship $U(1) = \Delta \cos(\alpha + \beta)$ has been utilized. Solving eqn. 3.16 and plugging the result into eqn. 3.17 yields a non-linear equation that defines Λ, which is quadratic in terms of the applied end displacement. Once the full solution is found, one can compute the reaction forces at the right end of the strut, i.e. $\tilde{F}_x = \mp \Lambda^2$ and $\tilde{F}_y = -W'''(1)$.

The governing equations described in eqns. 3.16 - 3.17 provide a complete set of equations that can be solved for the response as a function of the slenderness ratio $L/h = 1/\bar{h}$, strut angle α and loading direction β. Since the nature of the solutions depends on the

sign of the strain of the neutral axis, it is most convenient to present two sets of solutions: one for the tensile regime and one for the compressive regime. A convenient and robust way to generate response relationships (*e.g.* load-deflection, strain-displacement, *etc.*) is outlined in Section 2.3.

The tension regime, $\epsilon_o > 0$***:*** In this regime, the average axial stress in the strut is positive. The solution is found from eqns. 3.16 and 3.17 using the top signs in the equations, yielding:

$$W(\bar{x}) = \Delta \sin(\alpha+\beta)\left[\frac{\Lambda\bar{x}\cosh(\Lambda/2) - \sinh(\Lambda/2) + \sinh\left([\Lambda - 2\Lambda\bar{x}]/2\right)}{\Lambda\cos(\Lambda/2) - 2\sin(\Lambda/2)}\right] + \tilde{\kappa}_o f_t(\Lambda,\bar{x})$$

$$f_t(\Lambda,\bar{x}) = \frac{\Lambda(\bar{x}-1)\bar{x} + \sinh(\Lambda\bar{x}) - \coth\left(\frac{\Lambda}{2}\right)(\cosh(\Lambda\bar{x})-1)}{2\Lambda} \tag{3.18}$$

$$\tilde{F}_x = \Lambda^2 \tag{3.19}$$

$$\tilde{F}_y = \frac{1}{2}\Lambda^2\left(\frac{2\Delta\sin(\alpha+\beta)\left(e^{\Lambda}+1\right)\Lambda}{e^{\Lambda}(\Lambda-2)+\Lambda+2} + \tilde{\kappa}_o\right) \tag{3.20}$$

where the parameter Λ is related to the applied displacement according to:

$$a_t(\Lambda,\alpha,\beta)\cdot\Delta^2 + b_t(\alpha,\beta,\tilde{\kappa}_o)\cdot\Delta + c_t(\Lambda,\tilde{\kappa}_o,\bar{h}) = 0 \tag{3.21}$$

$$a_t(\Lambda,\alpha,\beta) = \frac{\Lambda\sin^2(\alpha+\beta)(\Lambda(\cosh(\Lambda)+2) - 3\sinh(\Lambda))}{4\left(\Lambda\cosh\left(\frac{\Lambda}{2}\right) - 2\sinh\left(\frac{\Lambda}{2}\right)\right)^2}$$

$$b_t(\alpha,\beta,\tilde{\kappa}_o) = \cos(\alpha+\beta) + \frac{\tilde{\kappa}_o}{2}\sin(\alpha+\beta)$$

$$c_t(\Lambda,\tilde{\kappa}_o,\bar{h}) = \frac{\tilde{\kappa}_o^2(\Lambda(\cosh(\Lambda)+2) - 3\sinh(\Lambda))}{24\Lambda(\cosh(\Lambda)-1)} + \frac{\bar{h}^2}{12}\Lambda^2$$

Note that eqn. 3.21 indicates that the displacement for a given level of tensile strain (defined by Λ) can be multi-valued: this reflects the fact that tensile strains can be developed either by pulling downwards on the strut (see Figure 3.1), or pushing the strut

upwards through the 'flat' position to the point that strains become tensile.

The above solution is valid unless the strain at the strut centerline is compressive. Taking the limit of eqn. 3.21 with $\Lambda \to 0$ and solving for Δ, one determines that the tensile regime corresponds to:

$$\Delta < 0 \quad \& \quad \Delta > \frac{5\left[\tilde{\kappa}_o + 2\cot\left(\alpha+\beta\right)\right]}{6\sin\left(\alpha+\beta\right)} \tag{3.22}$$

$$\tilde{F}_1 \quad > \quad -10\left[\tilde{\kappa}_o + 2\cot\left(\alpha+\beta\right)\right]\sin\alpha \tag{3.23}$$

$$\tilde{F}_2 < 0 \quad \& \quad \tilde{F}_2 > 10\left[\tilde{\kappa}_o + 2\cot\left(\alpha+\beta\right)\right]\cos\alpha \tag{3.24}$$

Note that the above transition forces have been computed for the global coordinate system. An analysis of the compressive solutions yields identical transition points, such that the relevant solution (tension or compression) is completely determined by the inequalities above. In the limit of small deflections, $\Lambda^2 \simeq (12/\bar{h}^2)\Delta\cos\left(\alpha+\beta\right)$, and the macroscopic forces and displacements are related by:

$$\begin{bmatrix} \tilde{F}_1 \\ \tilde{F}_2 \end{bmatrix} = \frac{12}{\bar{h}^2}\begin{bmatrix} \cos^2\alpha + \bar{h}^2\sin^2\alpha & -\cos\alpha\sin\alpha\left(1-\bar{h}^2\right) \\ -\cos\alpha\sin\alpha\left(1-\bar{h}^2\right) & \bar{h}^2\cos^2\alpha + \sin^2\alpha \end{bmatrix}\begin{bmatrix} \Delta_1 \\ \Delta_2 \end{bmatrix} \tag{3.25}$$

which can be confirmed independently by conducting a small displacement analysis.

Finally, the strains in the beam are given by:

$$\epsilon_{max} = \frac{\bar{h}^2\Lambda^2}{12} \pm \frac{\bar{h}}{2}\left(\tilde{\kappa}_o f_\epsilon^t(\Lambda,\bar{x}) + \frac{\Delta\Lambda^2\sin(\alpha+\beta)\sinh\left(\frac{1}{2}(\Lambda-2\Lambda x)\right)}{\Lambda\cosh\left(\frac{\Lambda}{2}\right)-2\sinh\left(\frac{\Lambda}{2}\right)}\right) \tag{3.26}$$

$$f_\epsilon^t(\Lambda,\bar{x}) = \left(\frac{1}{2}\Lambda\sinh(\Lambda\bar{x}) - \frac{1}{2}\Lambda\coth\left(\frac{\Lambda}{2}\right)\cosh(\Lambda\bar{x}) + 1\right) \tag{3.27}$$

where the positive sign corresponds to the strains at the bottom of the strut and the negative sign corresponds to strains at the top of the strut. Referring to Figure 3.1, the

maximum tensile strain in the beam occurs at the top of the strut at $\bar{x} = 0$ when the beam is pulled downwards, and the top of the strut at $\bar{x} = 1$ when the beam is pushed upwards. (Similarly, the maximum compressive strains occur on the opposite face and opposite end.) That is, when the average axial strain in the beam is tensile, the maximum tensile strains always occur at the endpoints, in accordance with the bending strains. In the compressive regime, this is not necessarily true. These observations can be easily verified numerically using the above solutions.

The compressive regime: $\epsilon_o < 0$***:*** In this regime, the average axial stress in the struts is negative. The solution for this regime is found using the bottom signs of eqns. 3.16 and 3.17, yielding the results:

$$W(\bar{x}) = \frac{\Delta \sin(\alpha+\beta)\left(\cos(\Lambda\bar{x}) + \cot\left(\frac{\Lambda}{2}\right)(\Lambda\bar{x} - \sin(\Lambda\bar{x})) - 1\right)}{\Lambda\cot\left(\frac{\Lambda}{2}\right) - 2} + \tilde{\kappa}_o f_c(\Lambda, \bar{x}, \tilde{\kappa}_o)$$

$$f_c(\Lambda, \bar{x}, \tilde{\kappa}_o) = \frac{\tilde{\kappa}_o\left(\Lambda(\bar{x}-1)\bar{x} + \sin(\Lambda\bar{x}) + \cot\left(\frac{\Lambda}{2}\right)(\cos(\Lambda\bar{x}) - 1)\right)}{2\Lambda} \tag{3.28}$$

$$\tilde{F}_x = -\Lambda^2 \tag{3.29}$$

$$\tilde{F}_y = -\frac{2\Delta\sin(\alpha+\beta)\Lambda^3\sin(\Lambda)\csc^2\left(\frac{\Lambda}{2}\right)}{4\Lambda\cot\left(\frac{\Lambda}{2}\right) - 8} - \frac{\tilde{\kappa}_o\Lambda^2\csc^2\left(\frac{\Lambda}{2}\right)(\Lambda\sin(\Lambda) + 2(\cos(\Lambda) - 1))}{4\Lambda\cot\left(\frac{\Lambda}{2}\right) - 8} \tag{3.30}$$

where the parameter Λ is related to the applied displacement according to:

$$a_c(\Lambda, \alpha, \beta)\cdot\Delta^2 + b_c(\alpha, \beta, \tilde{\kappa}_o)\cdot\Delta + c_c(\Lambda, \tilde{\kappa}_o, \bar{h}) = 0 \tag{3.31}$$

$$a_c(\Lambda, \alpha, \beta) = \frac{\Lambda\sin^2(\alpha+\beta)(\Lambda(\cos(\Lambda)+2) - 3\sin(\Lambda))}{4\left(\Lambda\cos\left(\frac{\Lambda}{2}\right) - 2\sin\left(\frac{\Lambda}{2}\right)\right)^2}$$

$$b_c(\alpha, \beta, \tilde{\kappa}_o) = \cos(\alpha+\beta) + \frac{\kappa_o}{2}\sin(\alpha+\beta)$$

$$c_c(\Lambda, \tilde{\kappa}_o, \bar{h}) = \frac{\tilde{\kappa}_o^2\left(3(\Lambda - \sin(\Lambda))\csc^2\left(\frac{\Lambda}{2}\right) - 2\Lambda\right)}{48\Lambda} + \frac{\bar{h}^2\Lambda^2}{12}$$

Again, the displacement can be multi-valued: the two solutions split the compressive regime roughly in half, with one solution generating the load displacement curve in the initial loading stage through the buckling event seen in Figures 3.1 - 3.3, and the other covering the transition to the tensile regime. Taking the limit of eqn. 3.31 with $\Lambda \to 0$ and solving for Δ, we obtain transition points and small deformation results that are identical to those listed earlier from the tension solution, as expected.

In the compression regime, the strain in the beam is given by:

$$\epsilon(\bar{x}) = -\frac{\bar{h}^2\Lambda^2}{12} \pm \frac{\bar{h}}{2}\left(\tilde{\kappa}_o f_\epsilon^c(\Lambda,\bar{x}) + \frac{\Delta\Lambda^2 \csc\left(\frac{\Lambda}{2}\right)\sin(\alpha+\beta)\sin\left(\frac{1}{2}(\Lambda-2\Lambda x)\right)}{\Lambda\cot\left(\frac{\Lambda}{2}\right)-2}\right)$$
$$f_\epsilon^c(\Lambda,\bar{x}) = 1 - \frac{1}{2}\Lambda\left(\sin(\Lambda x) + \cot\left(\frac{\Lambda}{2}\right)\cos(\Lambda x)\right) \quad (3.32)$$

where the top sign refers to the bottom of the beam, and the bottom sign refers to the top of the beam. The position of the maximum strains in the compressive regime depend on the level of average axial strain, Λ.

3.2.3 Computation of relationships between loads, deflections, and strains

The above relationships between loads, deflections and the implicit parameter Λ are most easily evaluated parametrically. For example, one can use Λ as the specified parameter, and then compute associated deflections Δ by solving the associated quadratic function, then solve for the associated loads once Δ is determined. Figure 3.4 illustrates the relationships that emerge from this process for $\beta = \pi/2$ (i.e. $\delta_1 = 0$ for a lattice subject to zero lateral strain).

In Figure 3.4A, the term corresponding to $\sqrt{b^2-4ac}$ in the quadratic solution for Δ is plotted as a function of Λ for compressive loading. At discrete points, the radical becomes

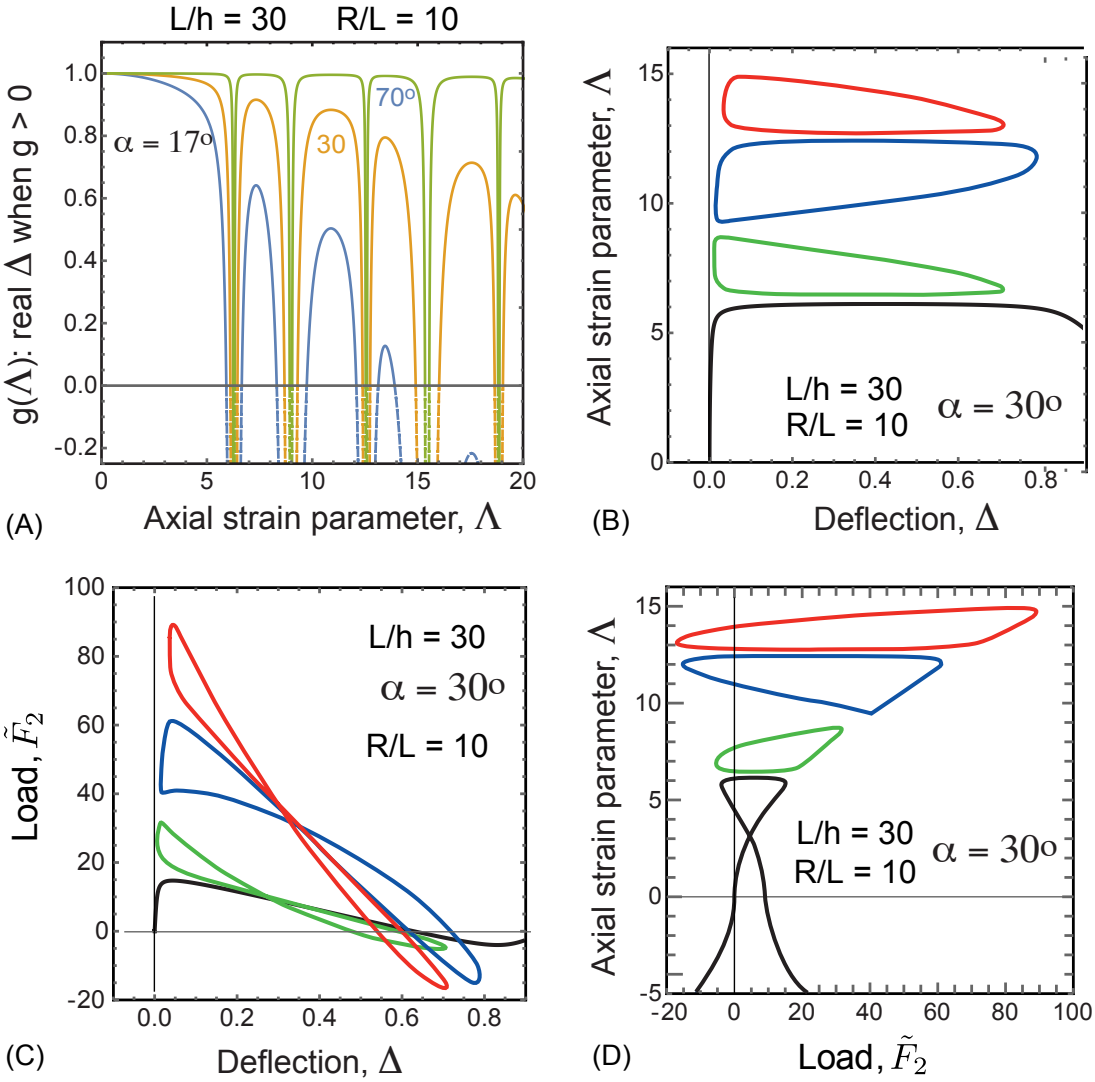

Figure 3.4: (A) Ranges of the axial strain parameter corresponding to real displacement solutions for several strut angles; smaller strut curvatures make the transitions more abrupt. (B) Axial strain parameter versus applied deflection for plane strain ($\epsilon_1 = 0$) illustrating the displacements associated with the domains in (A). (C) Load--displacement curves for the domains shown in (A). (D) Axial strain parameter as a function of applied force for the domains shown in (A-C).

negative, indicating imaginary displacement solutions: these discrete points correspond to the critical buckling points. As the imperfection is reduced (i.e. decreasing $\tilde{\kappa}_o$), the regions with imaginary solutions decrease in size. It is interesting, and critically important, that setting $\tilde{\kappa}_o \equiv 0$ yields similar solutions *that eliminate the first critical point, i.e. the first buckling mode*. Thus, the inclusion of an infinitesimal but non-zero value for $\tilde{\kappa}_o$ is needed to capture the lowest buckling mode, indicating that the problem is sensitive to imperfections. For values of Λ beyond the first critical point shown in Figure 3.4A, one recovers higher buckling modes; these higher order modes are seen in Figures 3.4B - 3.4D. As indicated by Figure 3.4A, the presence of 'higher order' buckling modes may disappear all together for certain strut angles, slenderness ratios and undeformed beam curvatures.

Once a set of (Λ, Δ) values are computed, all other solution variables can be computed in the following way. Critical loads and displacements for transitions, such as those shown in Figures 3.1 and 3.2, are most easily computed by ordering the triplets according to Δ, and then fitting an interpolation curve for subsequent computation. In generating the dataset, one must take care to specify a range of Λ associated with the lowest energy state of the solution; this was done by using the results in Figure 3.4 with a root finding algorithm to determine the maximum relevant value of Λ in the compressive regime. It is worth noting that the loads and deflections vary substantially for very small variations in Λ when Λ approaches the maximum allowable value. Hence, to resolve the response in detail, a non-uniform 'grid' in the parameter Λ is needed, with a densely populated grid in Λ near the peak values.

3.2.4 Approximate dynamic solutions with $\delta_1 = 0$ (constrained lattices)

Unlike the quasi-static response, the axial and transverse behavior cannot be decoupled in the dynamic response, and full solutions require both spatial and temporal discretization. However, building upon insights from the quasi-static solution, we present an approximate solution for the dynamic behavior that is shown to be accurate for $\alpha <\sim 20^o$. Further, we present the solution for a strut *without* imperfections ($\tilde{\kappa}_o = 0$), motivated by the fact the results are imperfection insensitive for these angles.

The approximate solution assumes that the time-dependent deflection of the beam can be described by:

$$W(\bar{x},\tau) = \Delta(\tau) f(\bar{x}) \cos\alpha; \quad U(\bar{x},\tau) = -\Delta(\tau) g(\bar{x}) \sin\alpha \tag{3.33}$$

where $\Delta(\tau)$ is the time-dependent vertical displacement of the center of the beam, and $f(\bar{x})$ is a time-***in***dependent function that describes the deformed shape of the beam. This is only an approximation, because the non-linear kinematics implies that it is not strictly possible to find such a separable solution. For the sake of simplicity, we will assume that $f(\bar{x}) = \sin^2(\pi\bar{x}/2)$, which satisfies the boundary conditions $f(0) = f'(0) = f'(1) = 0$ and $f(1) = 1$, and further, is the exact solution for buckling at large strut angles. Alternatively, we could choose $f(\bar{x}) = (3 - 2\bar{x})\bar{x}^2$, which is the quasi-static small deflection solution: the impact of the specific choice of $\bar{x}$ is surprisingly small, as can be demonstrated by repeating the following analysis with that assumption.

The full governing equations described earlier illustrate that the average axial stress in the beam is uniform provided the forces from axial accelerations are small in comparison to those arising from axial straining. Since the axial accelerations scale with $\ddot{\Delta}\bar{h}^2 \sin\alpha$

(in comparison to the transverse accelerations which scale with $\ddot{\Delta}\cos\alpha$), this is a fair approximation for moderate α but is not true for nearly vertical beams. Neglecting axial accelerations in eqn. 3.9 and using eqn. 3.33, one obtains:

$$-\sin\alpha\Delta(\tau)g'(\bar{x}) + \frac{\cos^2\alpha}{2}\left(\Delta(\tau)f'(\bar{x})\right)^2 = \epsilon_o(\tau) \tag{3.34}$$

Differentiating with respect to space, we find that:

$$-\sin\alpha\Delta(\tau)g''(\bar{x}) = -\frac{\cos^2\alpha}{2}\left(\Delta(\tau)\right)^2 f'(\bar{x})f''(\bar{x}) \tag{3.35}$$

Solving this subject to the boundary conditions $g(0) = 0$ and $g(1) = 1$, we obtain:

$$g(\bar{x}) = \bar{x} - \Delta(\tau)\frac{\pi}{32}\frac{\cos^2\alpha}{\sin\alpha}\sin\left[2\pi\bar{x}\right] \tag{3.36}$$

This completely defines the strain and strain rate distributions, as controlled by the displacement amplitude $\Delta(\tau)$:

$$\epsilon(\bar{x}, y, \tau) = -\Delta(\tau)\sin[\alpha] + \frac{\pi^2}{16}\cos^2\alpha\Delta(\tau)^2 - \frac{\pi^2}{2}\cos\alpha\cos\pi\bar{x}\Delta(\tau)\cdot y \tag{3.37}$$

$$\dot{\epsilon}(\bar{x}, y, \tau) = -\dot{\Delta}(\tau)\sin(\alpha) + \frac{\pi^2}{8}\cos^2\alpha\Delta(\tau)\dot{\Delta}(\tau) - y\cdot\dot{\Delta}(\tau)\frac{\pi^2}{2}\cos\alpha\cos\pi\bar{x} \tag{3.38}$$

where the first terms reflects $u'(\bar{x})$, the second term reflects $(1/2)\left[w'(\bar{x})\right]^2$, and the last terms reflects $w''(\bar{x})$.

Using this approximation in a statement of virtual work and integrating over the area of the strut yields an approximate dynamic governing equation for $\Delta(\tau)$:

$$m_o\ddot{\Delta}(\tau) + \tilde{\eta}\{c_o + c_{nl}\left[\Delta(\tau)\right]\}\dot{\Delta}(\tau) + \{k_o + k_{nl}\left[\Delta(\tau)\right]\}\Delta(\tau) = \tilde{F}_2(\tau) \tag{3.39}$$

where the linear (small deflection) coefficients are given by:

$$m_o = \frac{3}{8}\cos^2\alpha;\;\; k_o = \frac{12}{\bar{h}^2}\sin^2\alpha + \frac{\pi^4}{8}\cos^2\alpha;\;\; c_o = \tilde{\eta}\left(\frac{12}{\bar{h}^2}\sin^2\alpha + \frac{\pi^4}{8}\cos^2\alpha\right) \quad (3.40)$$

and the non-linear (large deflection) coefficients are given by

$$k_{nl}\left[\Delta(\tau)\right] = \frac{3\pi^2\cos^2\alpha}{32\bar{h}^2}\left[(\pi^2\cos^2\alpha\cdot\Delta(\tau)^2 - 24\sin\alpha\cdot\Delta(\tau)\right] \quad (3.41)$$

$$c_{nl}\left[\Delta(\tau)\right] = 6\pi^2\cos^2\alpha\left[\pi^2\cos^2\alpha\cdot\Delta(\tau)^2 - 16\sin\alpha\cdot\Delta(\tau)\right] \quad (3.42)$$

The linearized solution for small deflections (i.e. neglect of c_{nl} and k_{nl}) give an indication of the approximation's accuracy. First, it can be shown that k_o differs from the exact small-displacement solution by 1.5%. (That is, the pre-factor $\pi^4/8 \simeq 12.18$ in eqn. 3.40 is strictly equal to 12). Second, the *undamped* natural frequency of the approximation for small deflections is given by:

$$\Omega_n = \frac{\omega_n}{\omega_o} = \sqrt{\frac{k_o}{m_o}} = \sqrt{\frac{32}{\bar{h}^2}\tan^2\alpha + \frac{\pi^4}{3}} \quad (3.43)$$

The approximate solution differs from the exact solution for small deflections by 3.9%, in that the term corresponding to $\pi^4/3 \simeq 32.5$ is equal to 31.28 in the exact solution. Hence, the approximate solution provides highly accurate estimates for both the statics solution and first vibration frequency, with small differences arising from the fact that the assumed displacement functions are not strictly equal to either the static deflection profile or the first mode shape.

Finally, it is useful to note the effective damping coefficient in the limit of small

displacements, which is given by:

$$\xi_o = \frac{c_o}{2\sqrt{k_o m_o}} = \frac{1}{2}\tilde{\eta}\Omega_n = \frac{1}{2}\tilde{\eta}\sqrt{\frac{32\tan^2\alpha}{\bar{h}^2} + \frac{\pi^4}{3}} \tag{3.44}$$

The effective damping coefficient increases quickly with increasing strut angle; this is a consequence of the Kelvin-Voigt material approximation that implies rate effects scale with the system stiffness. For $\bar{h} = 0.1$, over the range of $0^o < \alpha < 20^o$, the effective damping coefficient falls in the range of $\sim 3\tilde{\eta} < \xi_o <\sim 12\tilde{\eta}$.

3.3 Illustrations of quasi-static response

3.3.1 Nature of the solutions for $\delta_1 = 0$ (constrained lattices)

The compressive regime is of primary interest for applications seeking to exploit bistable behavior. Here we examine compression, assuming the struts are constrained against displacement in the X_1-direction, which corresponds to $\beta = 90^o$ in the above solutions. Under displacement control and quasi-static loading, only the first buckling mode is relevant. The higher order loops shown in Figures 3.4(B-D) are indeed valid equilibrium solutions, but they are associated with higher energies due to higher neutral axis strains and deformed shapes with higher spatial frequencies. Hence, perturbations to the state of deformation associated with the first mode would be needed to overcome the associated energy barriers.

That said, it is interesting to note in Figure 3.4 that the higher order loops cross the lowest order loop for sufficiently large displacements. This raises interesting possibilities that external perturbations may overcome those energy barriers leading to a switch from one load-deflection path to another. Such perturbations would not have to involve changes in the macroscopic deformation of a *lattice*, since they involve only changes in the

deformed shape of the beam and not the displacements of the strut end-points. While the practical relevance of this higher order equilibrium states is open to question, knowing of their existence may shed light on future *dynamic* observations where oscillations may provide the impetus for switching modes.

Figure 3.5 provides illustrations that give insight into the nature of non-linear response under load control. All of these results are easily computed using the results presented earlier. Figure 3.5 depicts the relationship between the total potential energy of the system, the displacement, and strain energy as a function of applied load and resulting displacement. Figure 3.5 clearly illustrates that the total potential energy is reduced at the first critical load point by jumping to lower state at a fixed load. Upon unloading, the structure follows the lower path, as a return to the original displacement at the critical load would require an increase in the system's potential energy. If the structure is loaded to the second critical point, it snaps back to a new displacement, as shown in Figure 3.5. Note that the strain energy as a function of displacement does not shed much light on these transitions. Further, the strain energy at zero load is multi-valued (for this structure): the positive value at zero load corresponds to the strain energy stored in the structure in the deformed equilibrium state.

3.3.2 Complete response maps for compressive regime with $\delta_1 = 0$ (constrained lattices)

Here we illustrate the behavior of angled lattices subject to compression and plane strain deformation, *i.e.* $\delta_1 = 0$ ($\beta = \pi/2$). For simplicity, we cast the results in terms of a rhombic lattice (see Figure 3.1); however, it is worth emphasizing that the above solutions can be easily modified to generate results for other cell configurations, even three-dimensional structures provided appropriate symmetry constraints are applied. For

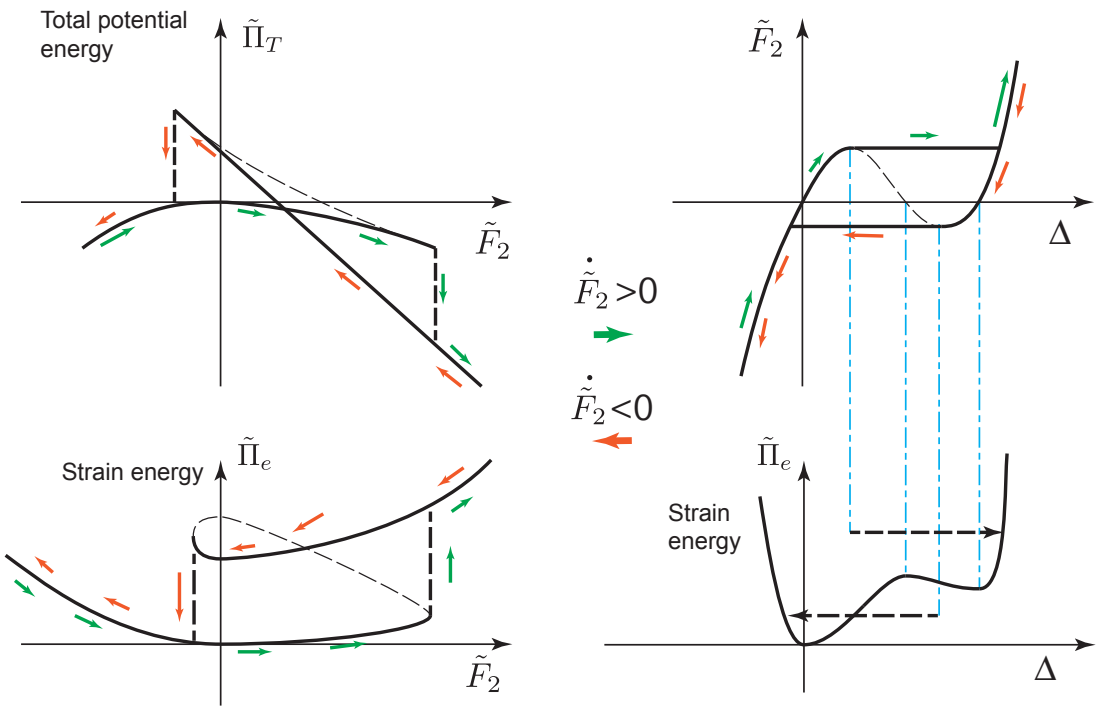

Figure 3.5: Schematic illustrations of the relationship between total potential energy, $\tilde{\Pi}_T$, strain energy $\tilde{\Pi}_e$, normalized force $\tilde{F}_2$ and displacement, Δ. Under load control, the path depends on whether the load is increasing or decreasing. The curves can be generated using the solutions presented here.

a rhombic lattice consisting of intersecting beams (see Figure 3.1A), the relative density of the lattice is given by:

$$\tilde{\rho} = \frac{\bar{h} + \bar{h}^2 \cos\alpha \sin\alpha}{\left(\bar{h}\cos\alpha + \sin\alpha\right)\left(\bar{h}\sin\alpha + \cos\alpha\right)}, \tag{3.45}$$

which takes into account the size of the nodes created by intersecting beams of finite width. A contour map of the relative density of rhombic lattices as a function of strut aspect ratio and strut angle is shown in Figure 3.6A. (Adopting the results for hexagonal lattices will naturally lower the relative density values.) The parametric algorithm described earlier was used to identify the type of response associated with each $(\bar{h}, \alpha)$ combination. The bottom red line indicates the boundary between structures that do and do not experience snap-through (i.e. negative stiffness). Below the bottom red curve, the behavior is non-linear but never unstable. The top red line indicates the boundary between structures that do and do not experience reverse snap-through upon unloading. It is striking that the contours for $\tilde{\rho} = 0.4$ and $\tilde{\rho} = 0.25$ align extremely well with the boundaries separating the three deformation regimes. This implies that an extremely accurate and simple calculation using eqn. 3.45 can be used to identify the critical length or angle needed to ensure each type of behavior.

Figures 3.6B and 3.6C illustrate contours of the specific strength of the cell and critical strain for snap-through, respectively. The strength is computed as the snap through load divided by the width of the cell, i.e. $\sigma_2 = F_2/L\cos\alpha$. The cell strain is computed as $\epsilon_2 = \delta_2/(L\sin\alpha)$, which is only strictly valid for rhombic lattices; critical strains for hexagonal lattices will be smaller, due to the presences of vertical struts. The results in Figure 3.6B illustrate that decreasing the aspect ratio of the struts (or increasing the strut angle) increases the snap-through stress faster than associated increases in density. For lattices with struts at low angles, the macroscopic strain at snap-through is quite

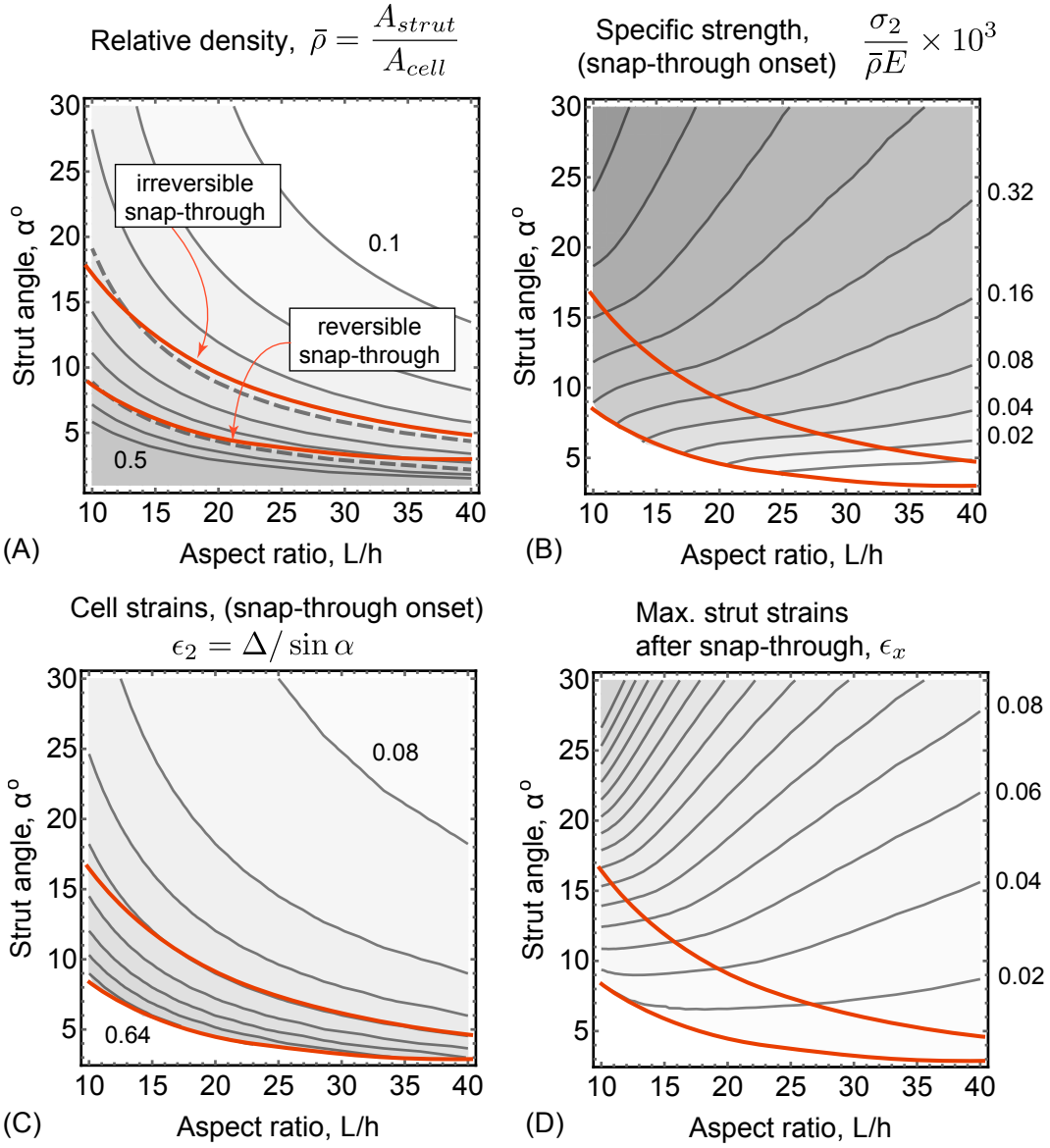

Figure 3.6: Summary of quasi-static response for $\delta_1 = 0$, i.e. lattices subjected to plane strain; (A) Contours of relative density for a rhombic lattice (in increments of 0.05), with superimposed boundaries between various regimes. (B) Contours (in increments of a factor of two) of specific strength for a rhombic lattice. (C) Contours of macroscopic strain on a rhombic lattice at the onset of snap-through (in increments of 0.08). (D) Contours of peak strut strain (in increments of 0.02) at the conclusion of snap-through, i.e. at the second displacement associated with the snap-through load.

large ($0.32 < \epsilon_2 < 0.64$), because the displacement at snap through is comparable to the vertical spacing of the lattice.

For all lattices experiencing snap-through, the displacement is greater than $L \sin \alpha$, indicating that self-contact always occurs for rhombic lattices. Neglecting self-contact (e.g. for hexagonal cells that have vertical struts), the displacement approaches $L \sin \alpha$ for small angles and large aspect ratios. Hence, for all practical purposes, snap-through without densification can only be achieved by including vertical struts in the lattice that are greater than $2L \sin \alpha$. Without such vertical struts, the lattice densifies at snap-through and the effective stiffness of the lattice rises by orders of magnitude.

Figure 3.6D depicts the peak strain in the struts after snap-through has occurred; the results correspond to strains at the snap-through load at the second (larger) displacement. These results were generated by finding the extrema of equation 3.26 and 3.27 with respect to position, at the second displacement associated with the snap-through load. One can see that in order to survive the snap-through event, the allowable strain in the nodes must be relatively high, creating significant concerns for struts and nodes made of brittle materials. This points to the desirability of using compliant or ductile materials at the nodes; in those instances, insightful results could be generated by re-solving the present framework to have zero moment at the nodes, instead of zero slope.

3.3.3 Buckling and loss of stiffness for lattices subjected to biaxial strain

The complete solutions (generated parametrically) described at the end of Section 2.2 can be easily searched to solve for biaxial strain states associated with a loss of stiffness. Each loading angle β corresponds to a given ratio of biaxial strains; for a rhombic lattice, these are $\epsilon_1 = \Delta \cos \beta / \cos \alpha$ and $\epsilon_2 = \Delta \sin \beta / \sin \alpha$. The corresponding stress state

can be computed from reaction forces using $\sigma_1 = F_1/(L\sin\alpha)$ and $\sigma_2 = F_2/(L\cos\alpha)$. For other types of cells, ϵ_2 and σ_1 must be adjusted to account for vertical posts. In what follows, we neglect the possibility of vertical post buckling. A complete illustration of biaxial strain states associated with buckling is show in Figure 3.7, along with the corresponding stresses.

To generate the results in Figure 3.7, the critical displacement associated with a loss of stiffness in each direction was computed as a function of loading direction, β; results are shown for critical displacements associated with a tangent stiffness that is 10% of the initial stiffness of the lattice. These critical displacements (and the associated reaction forces) were then converted to strains (and stresses) using the results above for a rhombic lattice. Strictly speaking, the 'instability' points associated with a loss of stiffness in each direction are different; practically speaking, buckling in either direction causes a similar loss of stiffness in the other. The curves in Figure 3.7 demonstrate that instabilities occur even for cases where there is a small tensile strain in one direction.

Figure 3.7A shows a close up of the results for small strains; the stiffness is relatively high in the third quadrant, where both strains are compressive. In this region, the usual impressions of buckling behavior are relevant. Similarly, in the first quadrant, the lattice is under tension in both directions and, though the stiffness may be highly non-linear, it will not decrease. Lines are also shown for the loading states associated with minimum stiffness, as inferred from the small deflection results in Section 2. These lines reflect end displacements that act perpendicular to the beam axis. When the strains are of opposite sign (i.e the second and fourth quadrants), the load-displacement curves are highly non-linear, and the range of displacements corresponding to linear behavior can be exceedingly small. Figure 3.7B shows a more macroscopic view of the strain space, and one observes 'loss of stiffness' boundaries very close to the minimum stiffness line. The associated states of stress are shown in Figure 3.7C; the high stress regions correspond

to the fourth quadrant (nearly equi-biaxial compression), while the needles pointing to zero stresses are traverses as the strain state migrates out of this quadrant.

The behavior of such 'soft' loading states is not associated with conventional buckling, but rather the fact that the reaction force changes sign due to large displacements relative to the beam thickness. While this domain may be irrelevant for lattice applications designed for robust snap-through behavior, it is likely relevant for other applications, such as the use of patterned electrodes utilized in soft actuators.

3.4 Illustrations of dynamic behavior for $\delta_1 = 0$ (constrained lattices)

The dynamic model of Section 2.4 can be use to predict the response to cyclic loading or impacts with comparatively rigid objects. In displacement control at slow loading rates (to be defined subsequently), the dynamic terms $\ddot{\Delta}$ and $\dot{\Delta}$ can be neglected; one obtains a simple cubic approximate solution for $\tilde{F}_2(\Delta)$. Figure 3.8A provides a comparison of this cubic approximation and the full non-linear quasi-static solutions defined earlier. The quasi-static cubic approximation is quite accurate for $0^o < \alpha < 15^o$ and $0.05 < \bar{h} < 0.1$. In what follows, we limit our attention regarding dynamic responses to this regime, as the approximate solution does not accurately capture non-linearities outside this regime.

To understand when quasi-static hysteresis estimates are relevant, consider the response of an angled strut subjected to an applied harmonic force given as:

$$\tilde{F}_2(\tau) \;=\; \frac{1}{2}\tilde{F}_o\left(1-\cos\left[r\Omega_n\tau\right]\right) \tag{3.46}$$

where $\tilde{F}_o$ is the peak force and $r \equiv \omega_a/\omega_n$ is the ratio of excitation frequency to the natural frequency of the structure. Hence, $r << 1$ represents nearly quasi-static loading

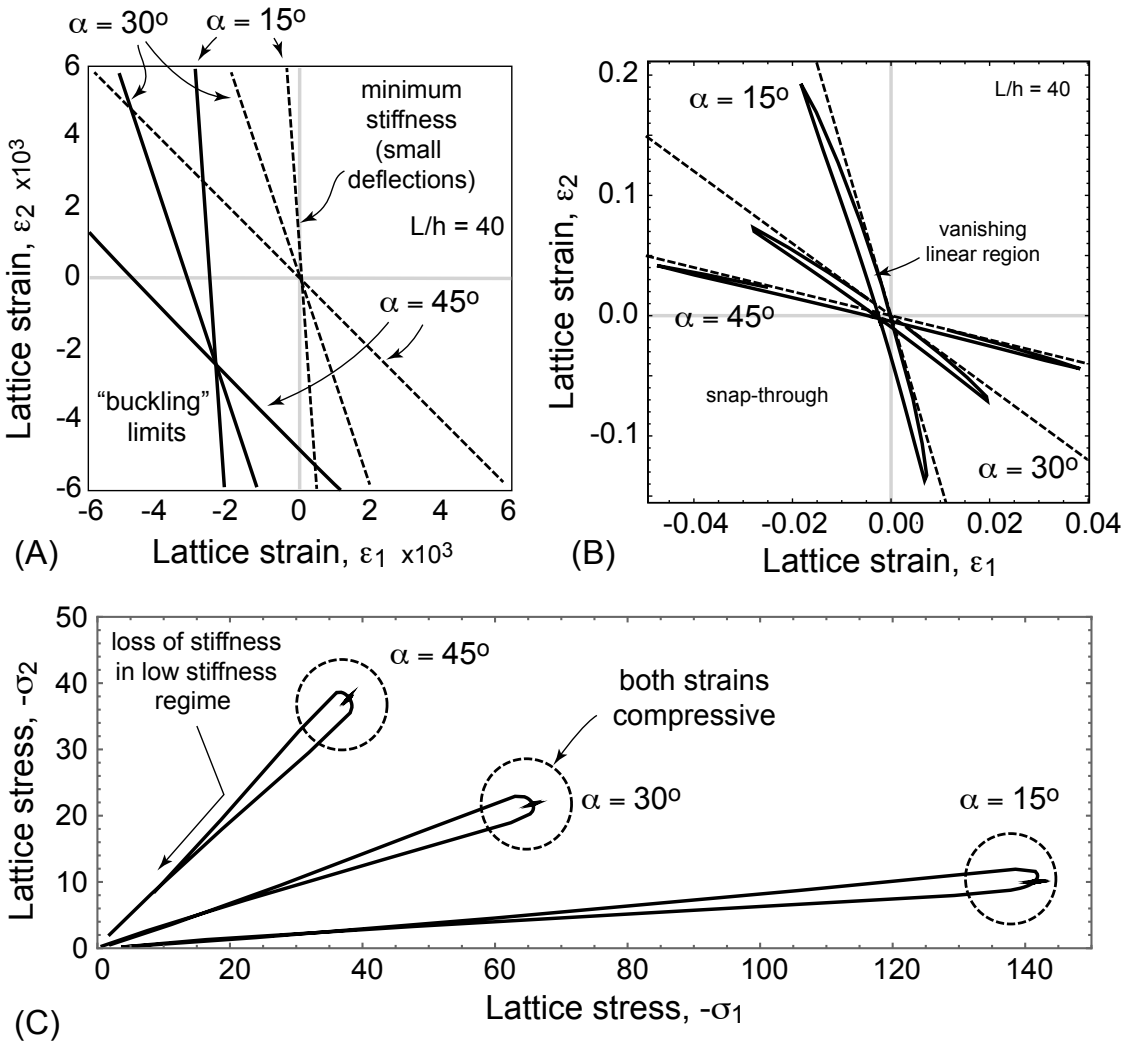

Figure 3.7: Buckling maps illustrating combinations of biaxial strains and stresses associated with a stiffness drop relative to the undeformed configuration, i.e. $k/k_o \leq 0.1$ where k_o is the stiffness at zero displacement. (A) A close-up view of the region of bi-axial compression, with dashed lines indicating strain combinations with minimum stiffness. (B) An expanded view of the buckling strain space, illustrating the stiffness drop contour is a closed loop. (C) Buckling stress space associated with the strain space shown (B).

in the sense that the applied loading rate is much smaller than the inertial response of the system. *However*, it is important to note that the structure's non-linear response under force control can be decoupled from the loading rate: simply put, any response influenced by decreasing stiffness will be strongly influenced by the inertial time scale, not the loading time scale.

This is illustrated in Figures 3.8B, which depicts the temporal response of the system for two different strut angles ($\alpha = 5^o$ and $\alpha = 8^o$), which exhibit different degrees of non-linearity. These results are for a 'slow' load cycle, whose period is fifty times greater than the small-displacement natural frequency of each strut ($\omega_n^{5^o} = 9.1\omega_o$ and $\omega_n^{8^o} = 12.7\omega_o$). The corresponding small-displacement damping coefficients in eqn. 3.44 are $\xi_o = 0.045$ (5^o) and $\xi_o = 0.064$ (8^o). These results clearly illustrate that decreases in stiffness trigger dynamic oscillations; for this level of damping and loading rate, the dynamic oscillations are essentially damped out prior to the return of the loading cycle to the low stiffness region.

Figures 3.8C and 3.8D show the force-displacement relationships for the third loading cycle, which are essentially equivalent to the second. Fully explicit dynamic FEA results are also shown, illustrating the excellent accuracy of the approximate model. The results for $\alpha = 5^o$ illustrate that any softening behavior due to strut geometry can trigger dynamic events, even for cases without quasi-static 'snap-through' events. Thus, non-linear behavior in angled lattices can effectively increase the damping of the structure, by exploiting dynamic oscillations triggered by softening regions of the load-deflection response. Importantly, the associated dissipation increase occurs even when the quasi-static response is fully stable, i.e. it occurs when the quasi-static response shows no hysteresis. When snap-through occurs (i.e. an instability), additional increases in dissipation can be dramatic.

To illustrate these effects, consider the energy required to drive the oscillator in force

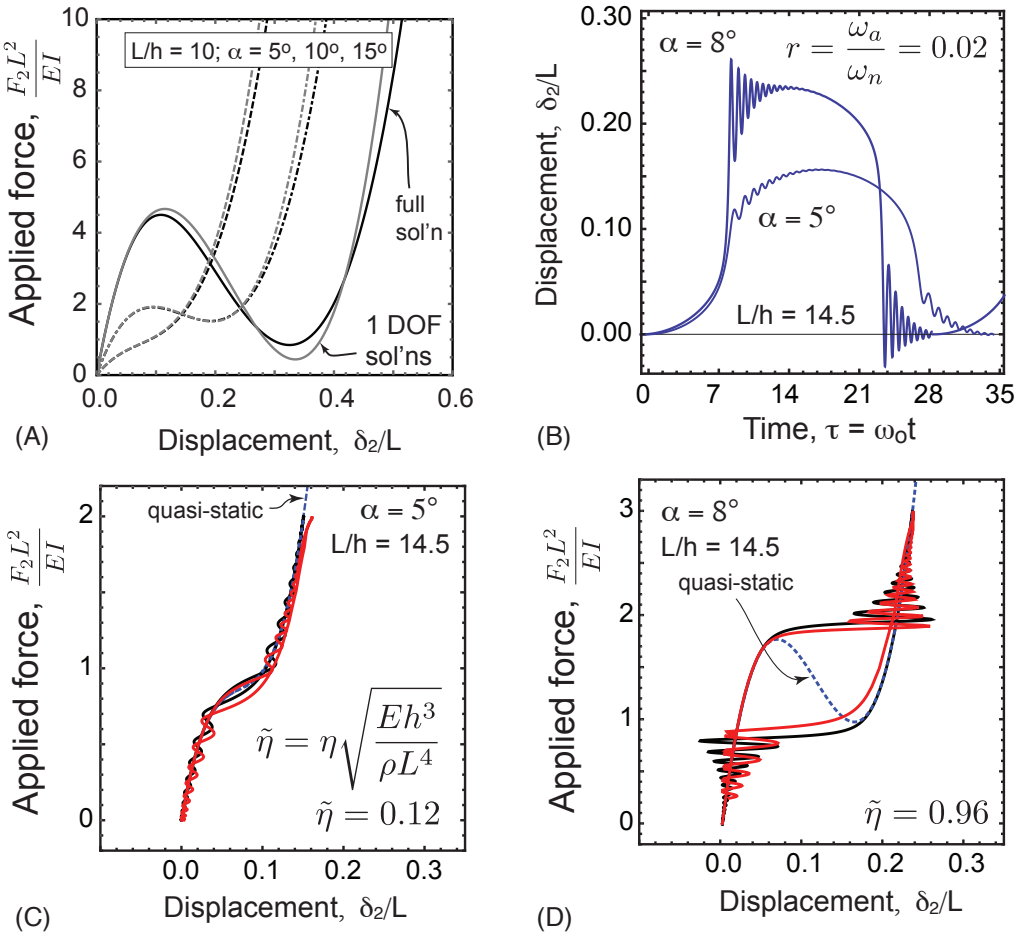

Figure 3.8: Illustrations of approximate dynamic response for low strut angles. (A) Quasi-static force-displacement curves associated with the approximation, compared with the complete solution. (B) Displacement versus time relationship for two differently angled struts loaded in force control, at a low frequency relative to the small displacement natural frequency. (C) Dynamic force-displacement curve of a structure that does not experience snap-through. (D) Force-displacement curve of a structure that experiences reversible snap through. Red lines in (C) and (D) are the results of fully explicit dynamic FEA with beam elements.

control. In terms of normalized response, the energy required over any time cycle is given by:

$$\tilde{\Pi}_d = \frac{L\Pi_d}{EI\omega_o^2} = \int_{\tau_1}^{\tau_2} \tilde{F}_2(\tau)\dot{\Delta}(\tau)d\tau = \frac{\tilde{F}_2^o}{2}\int_{\tau_1}^{\tau_2} \left(1-\cos\left[r\Omega_n\tau\right]\right)\dot{\Delta}(\tau)d\tau \quad (3.47)$$

For small deflections (*i.e.* small applied force), the energy dissipated *at steady-state* is given by:

$$\tilde{\Pi}_d^o = \frac{\pi\tilde{F}_o^2}{2}\left(\frac{\xi_o r}{4\xi_o^2 r^2 + \left(1-r^2\right)^2}\right) \quad (3.48)$$

which is identically zero for quasi-static loading ($r \to 0$) and scales linearly with $\tilde{\eta}$ and loading rate r for slow loading frequencies.

To begin, Figure 3.9A shows the hysteretic work computed using the quasi-static force-displacement solution. For cases with reversible snap-through, this is simply the area under the force-displacement curve as computed from the full solution. The central question at hand is whether this provides a reasonable estimate for hysteretic losses during cycling. Figures 3.9(B-D) illustrate the response under cyclic loading.

Figure 3.9B illustrates the required work per unit cycle to drive struts of different angles, normalized by the result for small deflections, $\tilde{\Pi}_d/\tilde{\Pi}_d^o$, and plotted as a function of applied force amplitude. Clearly, loads that produce snap-through reflect the large jump in hysteresis. This is also shown in Figure 3.9C for a single force amplitude, which plots the applied work per cycle versus the strut angle. For struts that experience snap-through, the results asymptotically approach the quasi-static hysteresis estimates. Note, however, that dramatic increases in damping can be observed even for cases that are stable under quasi-static loading. The results in Figure 3.9 illustrate that the small-deflection result for dissipated energy is an *overestimate* for very small strut angles; this

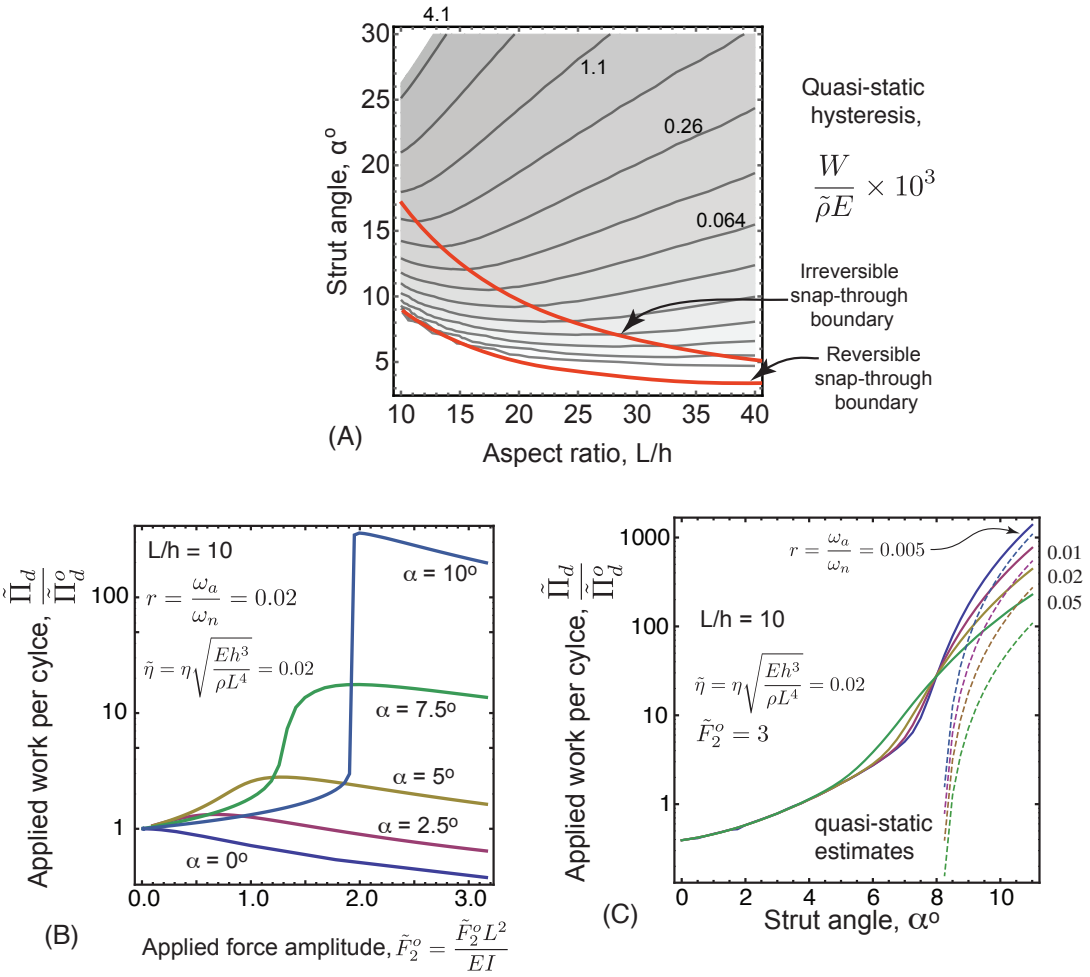

Figure 3.9: Work during cycling loading. (A) Hysteretic work of a quasi-static load--deflection cycle using the full solution. (B) Applied work per cycle normalized by the small deflection solution for several differently angled struts and slow load rates, as function of applied force amplitude. (C) Applied work per cycle normalized by the small deflection solution as a function of strut angle, for several frequencies and a single force amplitude.

is simply because these struts exhibit *stiffening* behavior. That is, the small-deflection solution overestimates the cyclic deflection range.

3.5 Discussion

3.5.1 Accuracy and range of applicability

As stated in the introduction, the moderate rotation theory is reasonably accurate for rotations less than about 30^o. Since snap-through (buckling) occurs at relatively small displacements, rotations are generally quite small up until snap-through, and the theory provides a very accurate estimate of the behavior. Quasi-static FEA calculations with *Abaqus* using shear-deformable beam elements (and including imperfections) were conducted for the range of $10 < L/h < 40$ and $0^o < \alpha < 60^o$; the present solutions have less than 8% error over this entire domain, with regards to force-displacement results up until snap-through. The largest discrepancies occur for aspect ratios at the low end of this range ($10 < L/h < 15$) and moderate strut angles ($20 < \alpha < 48$). In this region, shear in the strut contributes to the compliance, such that FEA load predictions are lower. Outside of this sub-domain, the errors are less than 5% and decrease rapidly in the $(L/h, \alpha)$ space away from this sub-domain.

The errors in *post-buckling* response can be (but are not necessarily) greater, since snap-through increases rotation. To get a sense of the practical implications of this limit for cellular materials, consider hexagonal cells (such as those in Figure 3.1) that are placed within a square box of dimension a. For angles below 15^o, set the height of the vertical sides to be the minimum required to ensure the struts do not touch when rotating through 30^o; in this case, the side struts are of dimension $a \tan(30^o - \alpha)$ and the center vertical posts required to fill in the square are slightly smaller than half this value. For

angles above 15^o, the vertical side and center struts are set to be of equal length, given by $(a/3)(1 - \tan\alpha)$. Cells with angles greater than $\alpha = 45^o$ are precluded from this discussion, as they no longer fit with the square cell.

For these cells, contact after snap-through occurs only after rotations exceed 30^o, and this level of deformation is precluded from the subsequent discussion. Assuming the vertical struts do not buckle, and their axial compression is negligible in relation to the vertical compression of the angle struts, the maximum allowable cell strain prior to exceeding the accuracy limit for moderate rotations is given by:

$$\epsilon_* = \tan\alpha - \tan\left(\alpha - 30^o\right), \tag{3.49}$$

which is always greater than 0.52 for $\alpha < 45^o$; hence, the model accurately predicts cell compression up to 50% strain for such lattices. The relative density of the cell in this exercise is given by:

$$\tilde{\rho} = \frac{\bar{h}}{2}\left(\frac{2 + \cos\alpha - \sin\alpha}{\cos^2\alpha}\right), \tag{3.50}$$

which ranges from $0.18 < \tilde{\rho} < 0.25$ for $\bar{h} = 0.125$ (arguably the upper limit for slenderness ratios accurately treated by a theory that neglects shear strains), and from $0.04 < \tilde{\rho} < 0.05$ for $\bar{h} = 0.025$ (a relatively large aspect ratio of $L/h = 40$). Thus, setting the relative density of the cells between $0.04 < \tilde{\rho} < 0.25$ and limiting the focus to $\epsilon_2 < 0.5$ ensures such hexagonal cells are appropriately addressed with moderate rotation theory.

3.5.2 Evaluating designs for multi-cell lattices that target specific responses

The ease of generating force displacement curves across the $(\bar{h}, \alpha)$ space, combined with the power of superposition, provides an opportunity to explore the design of multi-cell lattices that target specific macroscopic responses. Since the solutions enforce the restriction that lattice nodes do not rotate, such studies should be regarded as exploratory and limited to confined lattices such as those shown in Figure 3.10, or similar designs where nodal rotations are unlikely.

Figure 3.10 illustrates two different concepts for multi-cell lattices between stiff face plates: in (A), two different types of cells with different angles and strut thickness alternate parallel to the loading direction. The idea is to combine the stiff, unstable response of a high angle cell with slender members and the soft, stable response of a low angle cell with thicker members. The composite response is approximated as the sum of the forces in each cell generated during uniform compression. The struts in Figure 3.10A were chosen to minimize hysteresis associated with the plateau region; naturally, the strut angles, strut aspect ratios, and the lateral periodicity of the cell pattern (e.g. area fraction of each cell) and aspect ratios can be adjusted to modify the level of hysteresis.

Figure 3.10B illustrates a second concept, where struts of various slenderness ratios and angles are embedded within a master cell; the idea is to exploit the sequential buckling of struts (naturally leading to self contact at the cell vertex). The uppermost strut has an aspect ratio of $L/h = 20$, with aspect ratios of inner struts adjusted according to their angle (with fixed lateral span). The composite cell response is computed by assuming the force on the inner struts is zero until the outer struts experience snap through and come into contact. The response can only be regarded as approximate, as possible changes in response due to contact outside the vertex of the angled struts are ignored. Nevertheless,

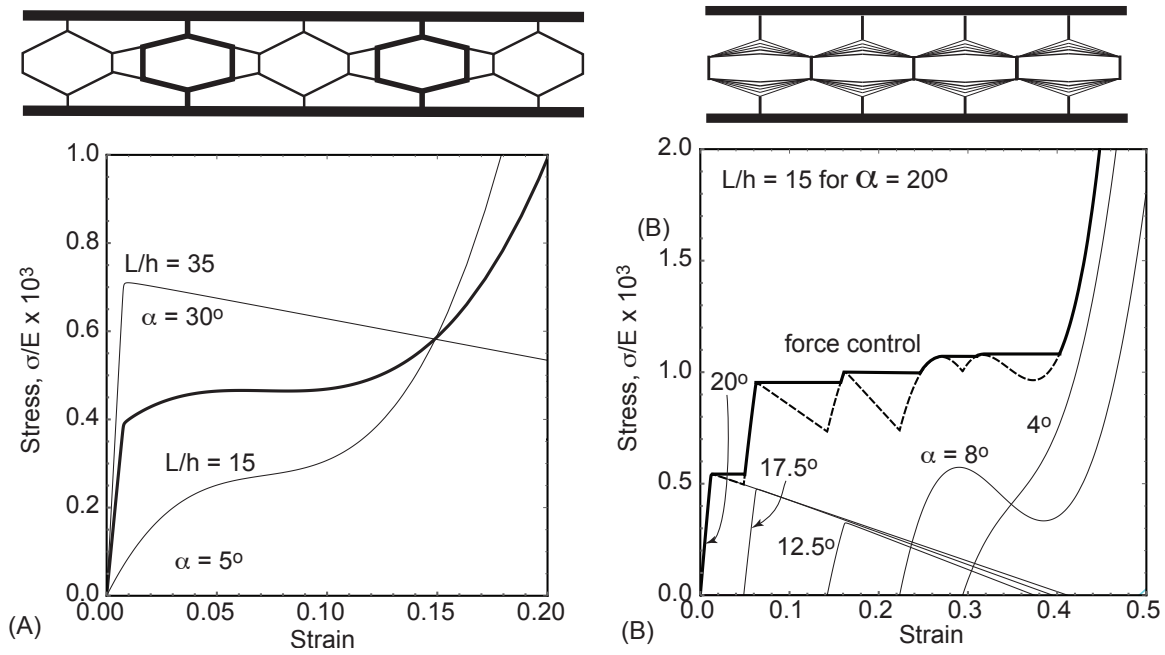

Figure 3.10: Cell designs illustrating the use of superposition to guide the development of foam architecture: (A) superposition of two different cells subjected to the same rigid displacement leads to high stiffness and a plateau stress with negligible snap-through, (B) embedded struts that buckle sequentially as they make self-contact.

it is insightful that one can approximately double the plateau stress and densification strain in comparison to the multi-cell truss in Figure 3.10A. The present framework thus provides an efficient tool for programmable materials.

3.6 Conclusions

The results presented here lead to several important conclusions regarding the nonlinear response of cellular materials that utilize angled struts:

- The complete solutions enable a comprehensive view of the design space, in that they provide: (i) a regime map indicating all combinations of slenderness ratios and strut angles that produce snap-through behavior and/or permit a second stable con-

figuration, (ii) estimates for the macroscopic lattice stresses and strains associated with the onset of buckling, including biaxial states, and (iii) estimates of the strut strains that result from instabilities. Peak strains in the struts after snap-through generally range from 0.01 (at low densities) to 0.5 (at high densities), indicating the importance of future work to incorporate flexible nodes.

- The results can be expected to be highly accurate for hexagonal lattices with relative densities in the range of $0.04 < \rho < 0.25$ and macroscopic strains less than 50%. Snap-through regimes correlate strongly with relative densities; e.g. $\bar{\rho} < 0.4$ for snap-through and $\bar{\rho} < 0.25$ for stable deformed configurations. This enables one to quickly identify combinations of slenderness ratio and angle associated with each regime of behavior. Further, the present results for biaxial loading indicate the degree of orthogonal constraint required to achieve snap-through.

- Damping is increased dramatically by structures that exhibit softening behavior, even if the structure is otherwise stable under quasi-static loading. This implies high damping lattices can be constructed without the strong non-linearity of snap-through. Quasi-static hysteresis loops underestimate the work dissipated under cyclic loading, although they can be reasonable estimates for loads well above the critical snap-through load.

- The present framework provides an opportunity to explore multi-cell design spaces and evaluate the efficacy of candidate structures with regards to achieving a prescribed desired response.

Chapter 4

Inner bracing of low density truss structures to improve peformance

4.1 Introduction

Cellular materials with low relative density are important for a broad range of applications, notably cushioning for human-related contact. For relative densities below ∼15%, the mechanical response is controlled by buckling of struts or cell wells during large deformations—a potentially favorable mechanism that allows repeated use provided yielding does not intervene [8, 14–27]. As compared with stochastic elastic foams, regularized cellular materials offer a potentially broader range of performance, since topology can be exploited to elevate stresses needed to trigger cell buckling. The emergence of additive manufacturing creates tantalizing opportunities to fabricate 'architected foams' that combine various cell and strut sizes to achieve a specific non-linear response. [24, 53]

The design of cell configurations that control large deformation response is quite challenging in several respects. First, the strongly non-linear behavior associated with large rotations requires iterative solution approaches that often fail to find acceptable equi-

librium states, even for simple structures with relatively few struts. Second, converged simulations tend to be very time consuming. This suggests that routine numerical topological optimization is a non-starter; the computational expense and lack of robustness lead to halting searches that do not cover much of the design space. Third and finally, large deformation response can be quite sensitive to angular orientation of the struts (as will be illustrated). This implies a design space that does not vary smoothly with geometry, suggesting that direct search algorithms will be necessary for optimization. All of these considerations are in stark contrast to linear responses—e.g. the initial stiffness, or strength defined by the *onset* of buckling or plasticity— where numerical optimization of cellular structure is feasible, owing to the speed and robustness of elastic simulations and smoothness of the design space. [54–60].

With this in mind, a seemingly unavoidable design exercise is to make strategic modifications to well-understood configurations to suppress unwanted deformation. We adopt this approach here, considering triangular structures defined by angled struts connecting two rigid platens as shown in Figure 4.1. We explore the impact of including highly slender, interior struts that divide the 'base cell' into trapezoidal sub-cells (i.e. horizontal braces) or triangular sub-cells (i.e. angled interior braces). The scope is limited to large, elastic deformations of cells with low relative density (i.e. slender members that buckle prior to yielding). Several different strategies for distributing mass are considered; results are presented in terms of specific performance (i.e. strength and energy stored per unit mass), and normalized by the response obtained for a simple V-structure (i.e. Figure 1.1A). The focus is on buckling strength and energy stored during post-buckling deformation.

The overarching goals are to generate insight regarding the efficacy of using multiple strut sizes, and to provide design guidelines for developing new topologies. The underlying hypothesis—sub-cells with smaller thickness can improve response without

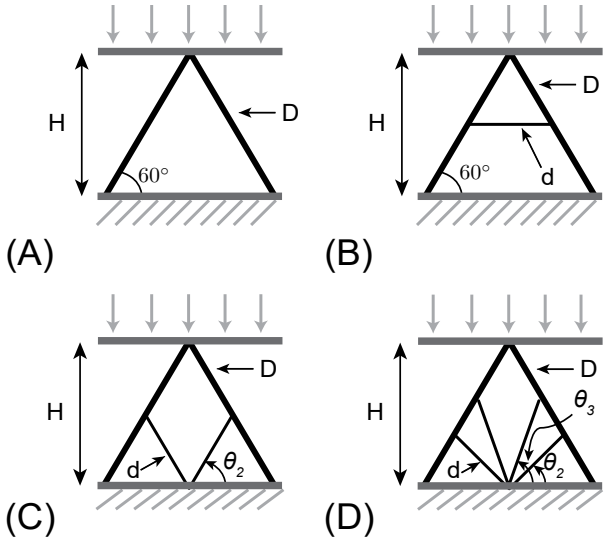

Figure 4.1: Schematic illustrations of the principal cell topologies considered here: (A) the base structure with no sub-cells used as the comparator, (B) trapezoidal sub-cells formed by horizontal interior struts, (C) triangular sub-cells formed by angled interior struts, (D) hybrid sub-cells formed by multiple types of interior struts.

comprising specific[1] properties —is based on two observations. First, on an elementary level, adding even a small spring as a lateral constraint can trigger higher order buckling modes in a vertical column. [61] Second, composites consisting of polymer strut-based lattices filled with stochastic foams exhibit compressive strengths and tangent moduli that exceed those expected from the rule of mixtures [62]. This synergy results from the lateral support provided by the foam to the lattice, which delays the onset of buckling to higher modes (unless strut yielding intervenes). However, the use of stochastic foams proves to be inefficient because it does not provide sufficient gains to offset the added mass [63]. This is because much of the foam, notably that near vertices, plays little role in altering the buckling behavior of the embedded lattice. This leads naturally to the hypothesis that buckling can be more effectively controlled with strategic placement of interior struts.

[1] i.e., normalized by mass of the structure

An important alternative approach to delaying the onset of buckling in low-density cellular materials is to use hollow truss members, which can provide strength increases of about a factor of three (relative to solid members) [64]. Lattices with hollow members have been fabricated by coating fugitive polymer lattices that were either printed [65] or photocured [66] with a metallic alloy, and subsequently removing the polymer phase via etching or volatilization. (Hollow members with arbitrary orientations are difficult to manufacture directly with many additive processes due to the need to remove sacrificial or unconsolidated materials.) The present analysis of solid members can be readily adapted to hollow structures through adjustments in material density and the second moment of area of the struts, provided the slenderness ratios are large enough that long wavelength buckling remains the dominant deformation mode.

Here, we present a comprehensive numerical study of the four topologies shown in Figure 4.1. While additional calculations will be needed to ensure the insights here translate into comparable three-dimensional structures (e.g. triangular pyramids with interior struts supporting each main strut), preliminary calculations reveal deformation on the faces of the pyramids that is identical to the two-dimensional structures considered here. Results are presented in the following way. First, each topology (i.e. utilizing a single type of interior strut or sub-cell strategy) is compared to the base V-structure (no braces) to demonstrate the range of load-displacement behaviors offered by each configuration. Then, different topologies are compared in order to identify the most promising hierarchical concepts. While one might expect a cellular structure with all of the mass in the main struts to be ideal, we show that this is *not* the optimal design in terms of strength and/or energy stored. A map of strength and energy storage is provided for several different topologies, as well as a global design map that illustrates the relative performance of all structures.

4.2 The design space of the present study

The design space is defined by the number of internal struts, their size relative to the main (outer) struts, and their orientation. In all cases, the outer struts are fixed to 60^o from the horizontal. Three central bracing concepts are explored: (i) the use of horizontal struts dividing the main structure into a triangular sub-cell and trapezoidal sub-cells as shown in Figure 4.1B, (ii) the use of a single set of two, angled, internal struts that divide the structure into two triangular sub-cells and one rhombic sub-cell as shown in Figure 4.1C, and (iii) the use of two sets of angled internal struts that divide the structure as shown in Figure 4.1D. We refer to these three concepts as having different 'topology class' [2], each defined by the combination of internal cell shapes created by internal bracing.

Even for fixed total mass, the distribution of mass within a given structure is an additional design variable that encompasses an extremely large range of possibilities. For example, each strut in the structure could be assigned its own diameter; a broad range of relative diameters could then be assigned in a large number of combinations. To simplify the study, we narrow the focus to consider only cases where the internal struts are of equal size; the structure using only main struts without internal bracing is used as the comparator. Three different strategies were explored to define the relative sizes of the outer and inner struts, as summarized in Figure 4.2.

Strategy A is the simplest approach to varying the mass distribution: the outer struts have fixed diameter D, and the inner struts have fixed diameter d. This corresponds to simply adding mass inside the cell; hence, the relative density of the braced structures increases slightly with the number of struts. The increase in relative density is relatively small, spanning from 5% for the unbraced 'base structure' to 7% for horizontal internal

[2]To be precise, any structure with different strut connectivity has a different topology, such that changing the number of horizontal struts changes the topology. However, for simplicity we group these into a single topology 'class'

struts with $D/d = 2$.[3] To mitigate the effect of added mass, specific properties are reported; for example, the specific strength of the braced structure σ_b/m_b is divided by the specific strength of the base structure, σ_o/m_o. In the approach, both the total mass and the partitioning between inner and outer struts changes as inner struts are added.

Strategy B holds the relative density fixed as internal struts are added, using the following procedure. First, a relative density is chosen for the base structure and the unbraced main strut diameter D is computed. Then, a single strut (or set of angled struts) is added to the structure, and the main strut diameter D is reduced to hold relative density constant and produce an initial diameter ratio, $D/d = constant$. For the cases with multiple horizontal bracing and two sets of angled interior struts, additional struts were created by dividing the first bracing strut into multiple equal volumes. In this approach, partitioning between the outer strut mass and *total* inner strut mass was held fixed.[4] Hence, relative density is fixed in this strategy, but the size ratio of outer to inner strut size changes as more struts are added (i.e. the inner struts become smaller relative to the outer struts as struts are added).

Strategy C holds the ratio between outer and inner struts fixed at constant ratio, D/d. As struts are added, both the main struts and inner struts are reduced in size to maintain both fixed relative density and fixed size ratio D/d. This implies that the mass partitioning between outer and inner strut varies as struts are added. In the end, this strategy proves less effective than the other two, since the reductions in the outer strut diameters dominate the response; for that reason, fewer results are presented for this strategy in favor of the other two.

In summary, the design space consisted of the number and orientation of internal

[3] As will be demonstrated, the gain in performance with added mass can be much larger than that rationalized by increases in relative density.

[4] Strategy B addresses the question: given a mass fraction to use on the interior, is better performance achieved using a single set of thick inner struts, or a larger set of thin inner struts?

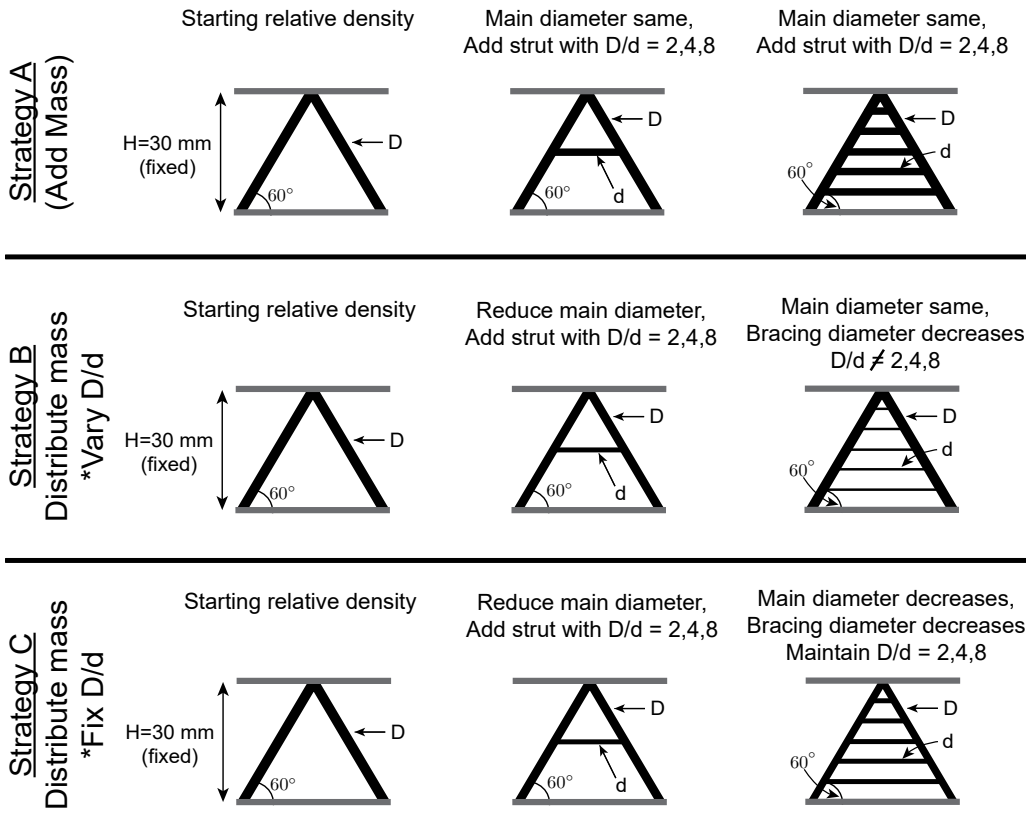

Figure 4.2: Mass distribution strategies that guided specification of outer strut and inner strut sizes; Strategy A involves adding mass (though the associated relative density changes are small) while Strategies B and C conserve mass and involve different mass partitioning between the inner and outer struts.

struts, and their size relative to the outer struts. The focus is on the mass distribution within the system, instead of overall mass (i.e. relative density). However, to assess the impact of relative density, select topologies from each 'class' are analyzed . The two performance metrics used to judge response are the peak load and the energy stored, both computed on a per mass basis.

4.3 Numerical approach

The truss structures were analyzed using SIMULIA Abaqus 6.12-1 [67] using Abaqus Explicit. An explicit method was chosen due to the strong non-linearities involved with snap-through instabilities that are inherent to many of the topologies in the present study. The structures were modeled using Timoshenko-Mindlin beam elements (B21 in Abaqus) with an elastic material (E = 1.5 GPa, $\nu = 0.3$); however, we present normalized quantities that render elastic property values arbitrary. No plasticity is defined; therefore, any post-buckling load drops that occur are *purely* geometric in nature. The top and bottom nodes of the structure were fixed to rigid compression platens. All connections between struts were modeled as rigid joints, which fixes the angle between two struts at their intersection. Self-contact between adjacent struts and contact between the structure and the platens was modeled as hard and frictionless. In the contact algorithm, elements are considered to be in contact when the beam element axis is coincident with either another beam element axis or one of the platens. The study defines the instant of self-contact as the densification strains, and focuses on response up to this limit.

An extensive study was conducted to establish the impact of loading rate, element size, imperfections, and structural damping coefficients. Small levels of damping were included using standard mass damping frameworks to suppress post-buckling oscillations. To establish consistent parameters that could be used across a very broad range of structures,

Parameter	**Normalized form**	**Value**
Element size	ℓ_e/L_s	0.024
Loading period	$\omega_0 t_{peak}$	2200
Damping coefficient	α_D/ω_0	0.45
Imperfection amplitude	A_{imp}/D	0.01
Number of eigenmodes	—	7

Table 4.1: Summary of parameters used in simulations; the characteristic frequency controlling bending dynamics is $\omega_o = \sqrt{EI/\rho AL^4}$.

a single configuration in each the four classes of structures shown in Figure 4.1 were analyzed under uniaxial compression. The study of numerical simulation parameters identified threshold values that ensure a negligible role in the peak strength and energy storage. A summary of the parameters used in this study is provided as Table 4.1. Comprehensive details of this numerical study are available in Chapter 2.

With regards to imperfections, a systematic study of the number of included eigenmodes and their amplitudes identified the minimum values needed to achieve results that were independent of specific choices. The overall goal was to choose parameters that *minimize* the predicted strength, such that estimates would be conservative. Generally speaking, including the first seven modes and imperfection amplitudes of 1% of the diameter lead to consistent load-deflection results across all structures. Fewer eigenmodes and smaller imperfections lead to higher peak strengths and more complex post-buckling behaviors, while more eigenmodes had no effect. Larger imperfection amplitudes naturally would impact the results, but they are associated with significant departures from nominal geometry and hence were not considered. Of course, small changes in the orientation of perfectly straight struts, or their diameter, are additional types of imperfections. The impact of such deviations are addressed explicitly in what follows.

4.4 Load-deflection responses of various topologies

Figures 4.3 and 4.4 show the load-displacement response for various topologies, inner strut angles and size ratios between the outer and inner struts (D/d). The loads on the structures are represented by the stress[5] on the cell per unit mass, divided by the same quantity computed for an unbraced structure. The cases in Figures 4.3 and 4.4 were chosen from a far more comprehensive design study to illustrate key features of the response. A detailed discussion of the design space for angled inner struts is presented in Section 4.5, while Section 4.6 provides a global overview of performance across the entire design space.

The structures with horizontal bracing in Figure 4.3A were generated with mass distribution Strategy B, which decreases the size of the outer struts when the first horizontal inner strut is added. This leads to a slight reduction in peak load relative to the unbraced, base structure. Horizontal braces produce significant increase in the post-buckling stiffness (relative to the base structure). The most significant increase occurs for three inner struts. This increase in stiffness is due to the fact that the asymmetric first buckling mode stretches the inner struts.[6]

For more than three struts, the strut diameter becomes too small to continue to add sufficient stiffness to the structure, hence representing an inefficient use of inner brace material. This is akin to filling low density lattices with stochastic foams; material near strut intersections experience less deformation and make a negligible contribution to load capacity. That said, the post-buckling load capacity of the case with five struts is nearly as good as the case with 3 struts, despite having much thinner members. This

[5]The stress on the structure is simply the force applied to the load point divided by the width of the base; for repeated structures between two comparatively rigid platens, this represents the average stress on the platens.

[6]The asymmetric first buckling mode is well-established for "V" trusses, and provides an excellent test of numerical procedures intended to find the lowest energy state.

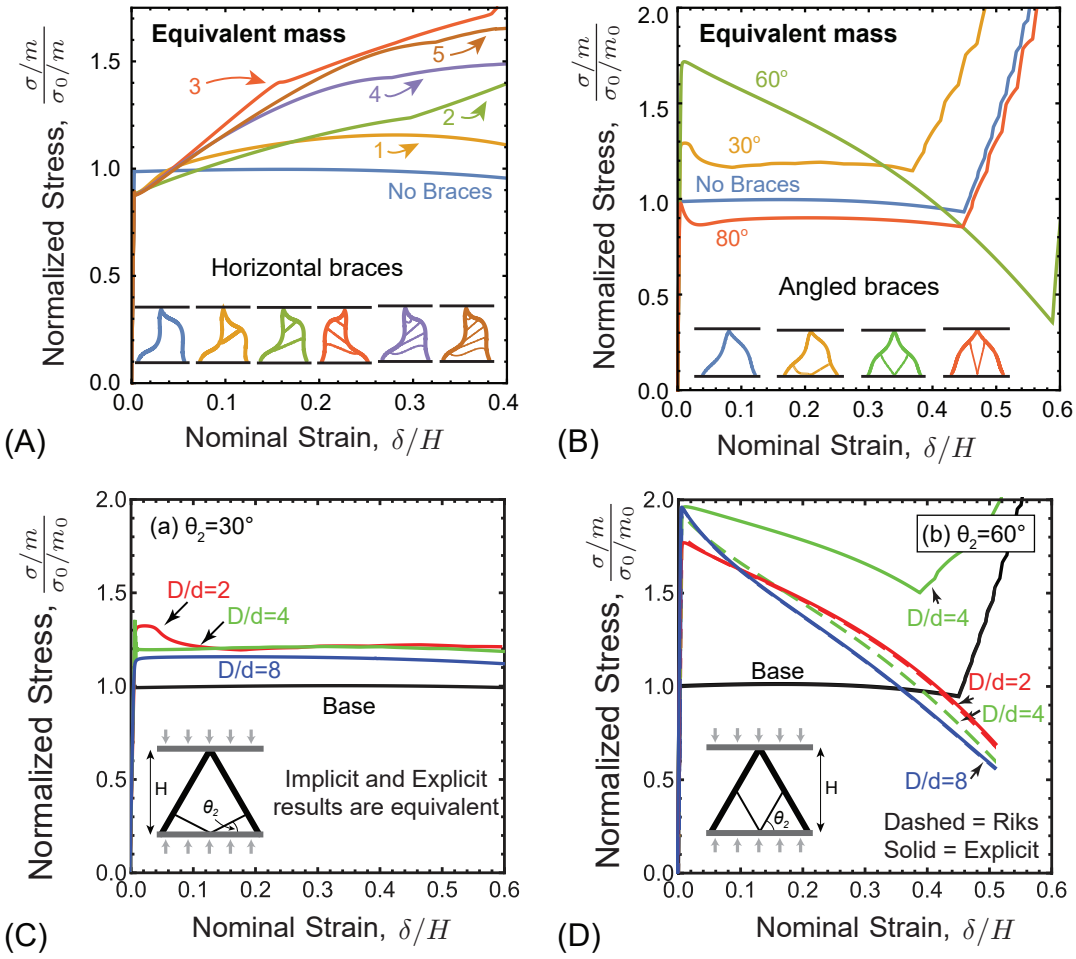

Figure 4.3: Typical load-deflection response for various trusses loaded in compression: (A) Horizontal inner struts, (B) a single set of angled inner struts at various angles, (C) Various size ratios (outer struts to inner struts) for 30^o inner struts, (D) Various size ratios (outer struts to inner struts) for 60^o inner struts. Mass distribution for each case is described in the text.

suggests that thin tension members, judiciously placed, can have a profound effect on post-buckling stability and lead to increases in energy storage.

It is important to note that the a single horizontal inner strut that connects the midpoints of the outer struts is less effective than using a greater number of thinner struts. This is true even though this case connects the two outer struts at the location with maximum buckling displacement. From the inset schematic of Figure 4.3A (colored yellow), a single horizontal strut does not prevent vertical motion of the mid-point of the main struts. By contrast, including angled struts that connect to the midpoints, as shown in Figure 4.3B, has a pronounced effect on the peak stress, due to suppression of the first buckling mode.

Figure 4.4 compares the load-deflection response of the four topologies shown in Figure 4.1, as well as the response of a structure with 60^o inner braces and a single horizontal strut that completes an inner triangle. The results illustrate that using two sets of angled inner struts provides improved strength and energy storage; essentially, 60^o struts increase strength by suppressing the first buckling mode, while 30^o struts provide post-buckling stability. The cases in Figure 4.4 are merely a subset from a much larger design study, and are broadly illustrative of the relative performance across all topologies. As illustrated in Figure 4.3B, however, the precise angle of inner struts significantly influences the response.

4.5 Complexity of the angled struts design space

A comparison of the cases shown in Figure 4.3 for angled inner braces illustrates that the response is highly sensitive to orientation (Figure 4.3B) and insensitive to inner strut size (Figures 4.3C and 4.3D). Of course, it is to be expected that connections near the mid-point will be most effective in suppressing buckling of the outer struts; indeed, inner

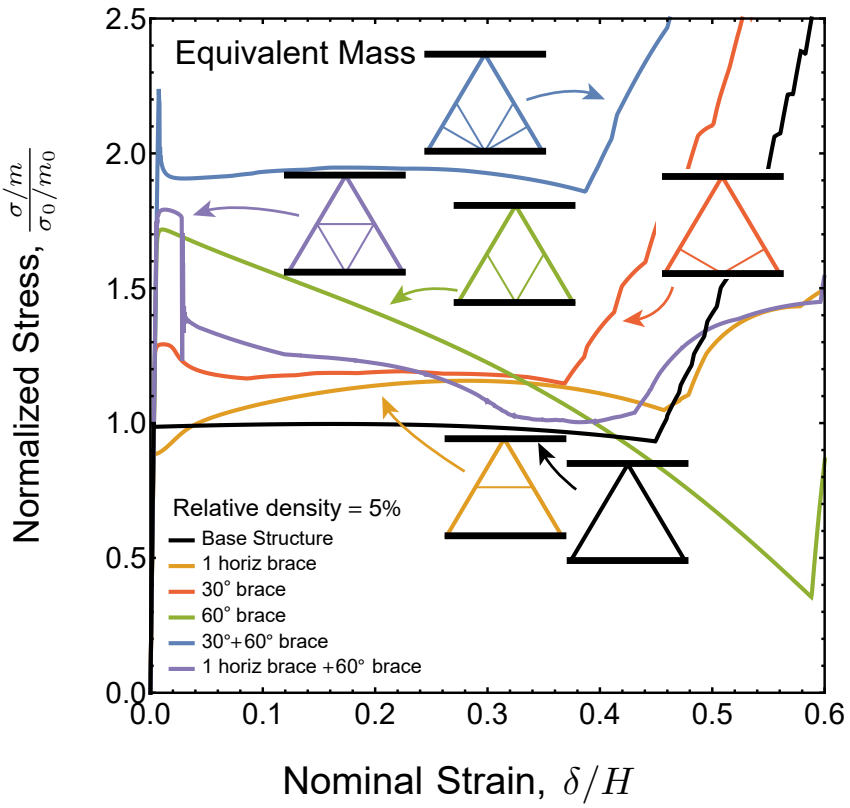

Figure 4.4: A comparison of load-deflection response for various strut topologies; all structures have equivalent mass, distributed using Strategy B, which fixes both the relative density and the partitioning of mass between inner and outer struts.

struts with 60^o orientation trigger the second buckling mode of the outer struts, nearly doubling the peak load. The perhaps surprising result is that even highly slender inner struts will produce this effect (e.g. D/d = 8, in Figure 4.3D). Apparently, even small translational or rotational constraints near the node of the outer strut buckling mode can be effective in pushing the outer struts to their second buckling mode. Interestingly, using thicker inner struts ($D/d = 2$) can be less effective, since more mass is taken from the main struts; the peak load can be pushed higher with thinner inner struts ($D/d = 8$) because the reduction in outer struts is smaller.

Motivated by the desire to fully characterize the design space (and ultimately optimize inner strut topology), a detailed study of inner strut orientation was conducted. The results for a single set of angled inner struts are shown in Figure 4.5, which depicts the peak strength and energy stored for a broad range of brace angles. Results are plotted for angles ranging from 5^o to 85^o, for inner strut sizes $D/d = 2, 4, 8$; results are also shown both Strategy A (simply adding mass) and Strategy B (reducing outer strut diameter to keep mass fixed). In most cases, Strategy A produces slightly higher results, as one expects for strategies that do not reduce the outer strut diameter.

The global trend with brace angle is clear from Figure 4.5; the best response is achieved with angles near 60^o that involve mid-point connections with the outer struts. Angles greater than 60^o generally perform better than angles less than 60^o. This is is due to the fact that the orientation of high angle inner struts are more closely aligned with the loading direction. The scatter in Figure 4.5 has profound implications for algorithms tasked with finding the angle that optimizes response. The associated sensitivity to inner brace angle more clearly illustrated in Figure 4.6, which shows the variation in peak strength and energy storage as a function of inner brace angle. As illustrated in Figure 4.6 connection locations of slender struts are critical; using thicker struts reduces the sensitivity to inner strut angle.

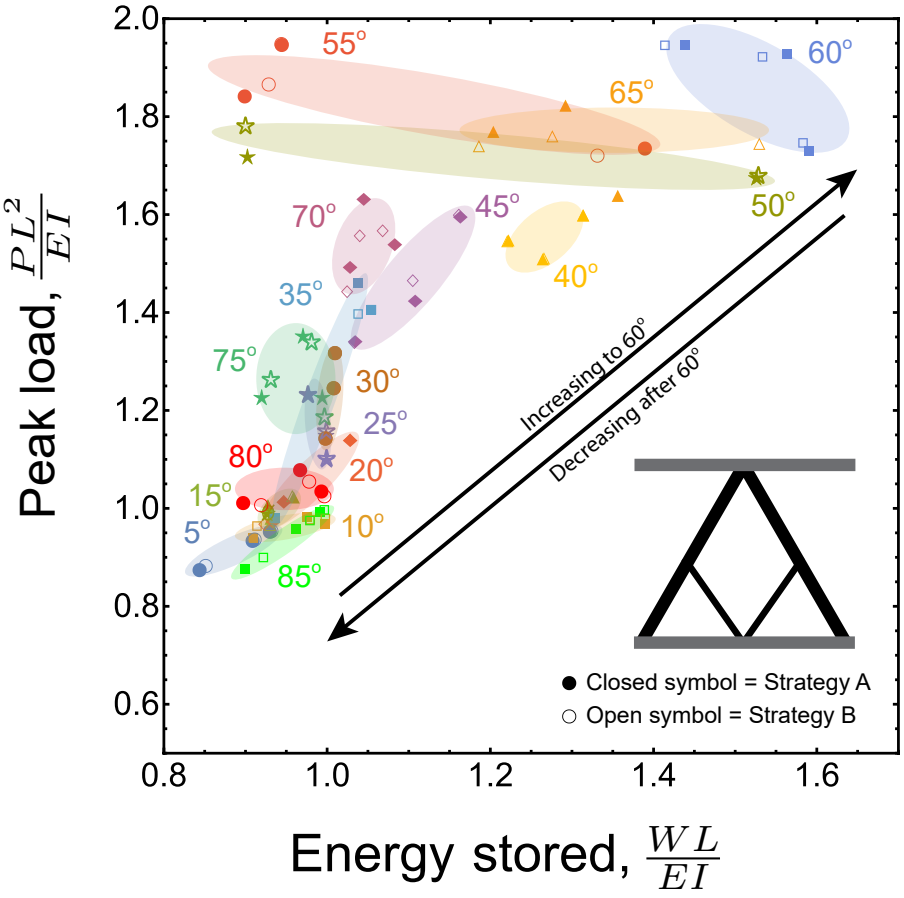

Figure 4.5: Map illustrating peak load and energy stored for angled interior struts, for a range of orientation angles and $D/d = 2, 4, 8$, using mass distribution strategies A and B.

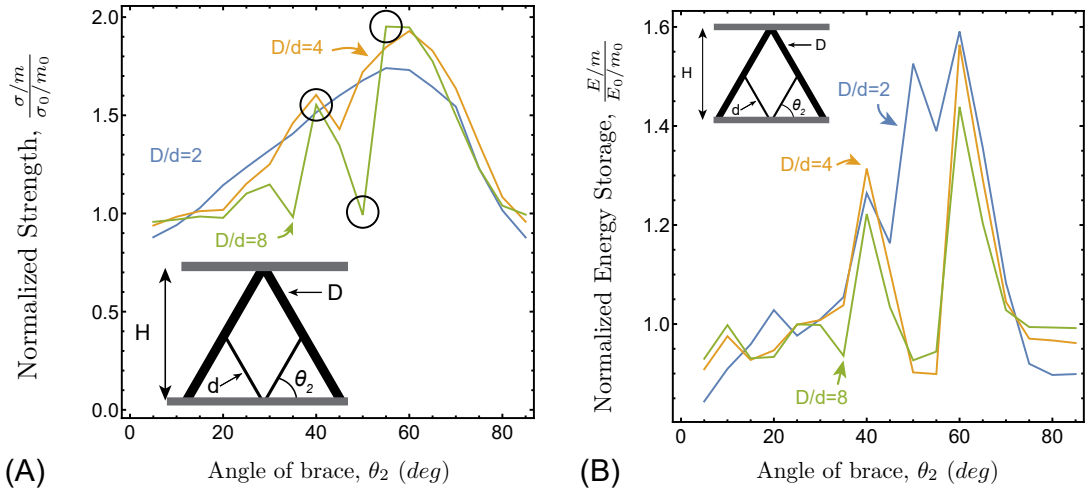

Figure 4.6: Results for one angle-brace structures. Points circled are checked for imperfection sensitivity, with the results shown in Figure 4.7. The relative density of the structures is $\sim 5\%$.

Naturally, the question arises as to whether or not sensitivity to inner strut angle is merely a consequence of the numerical solution technique: i.e., the parameters identified in Chapter 2 used throughout the parameter study. To address this question, additional numerical studies were conducted on the structures corresponding to the abrupt changes seen in Figure 4.6; black circles indicate the points chosen for this additional consideration. Figure 4.7 illustrates load-displacement responses for these cases, computed using a range of imperfections. To further substantiate the results, additional simulations were run using an independent large deformation finite element code developed by J. William Pro. Pro's code is an incremental, quasi-static framework (based on Newton-Raphson algorithms) that allows for arbitrary large rotations. Figure 4.7 shows comparisons of adding a different number of eigenmodes with two different imperfection amplitudes. The left figures show amplitudes that are the same for each eigenmode included in the simulation. Figures on the right show the imperfection amplitudes halved for each mode that is added.

While arbitrarily including fewer eigenmodes for certain angles elevates their predicted

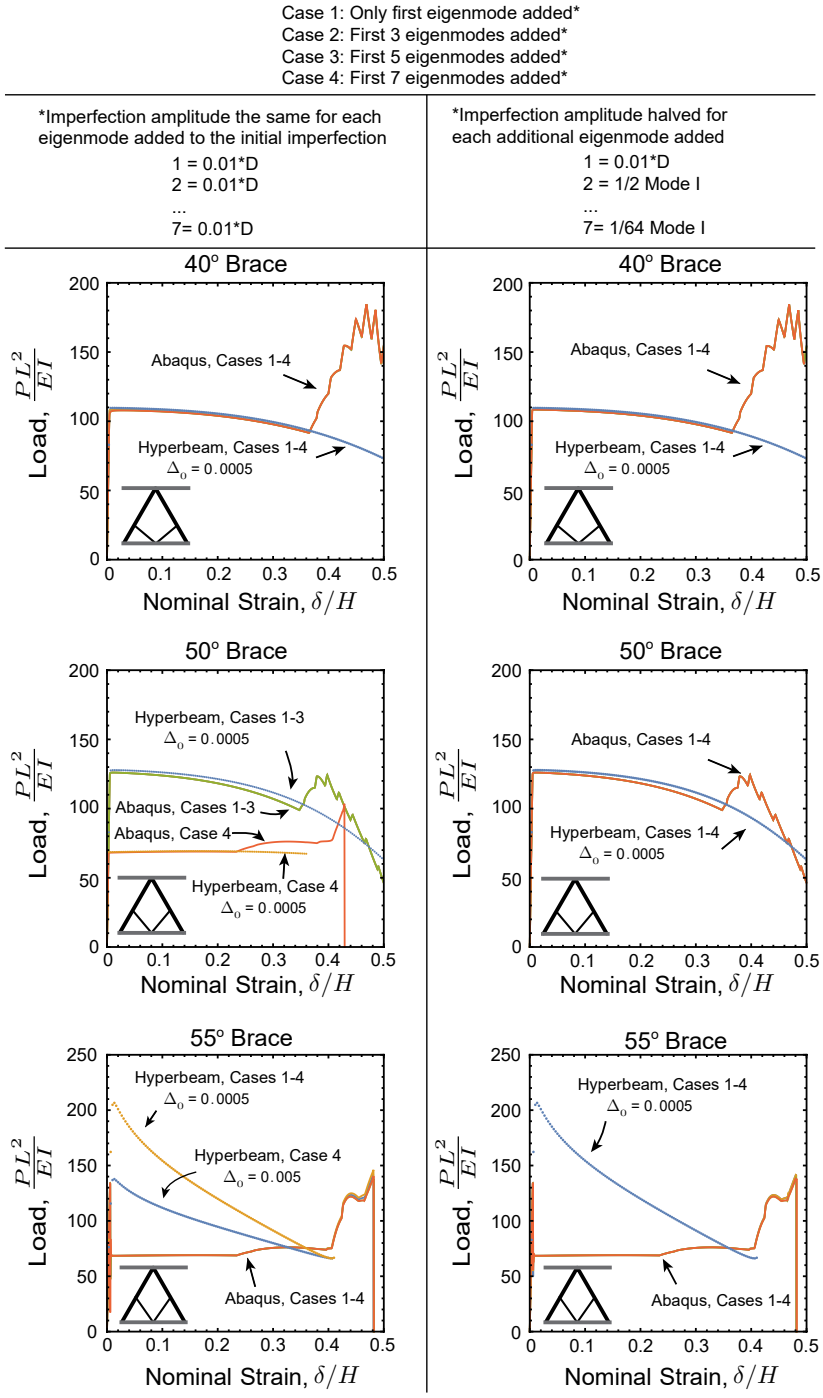

Figure 4.7: Results for the additional study of angled struts, performed to verify results are not due to imperfection sensitivity. Results compared with an independent large rotation code, which shows very good agreement overall; note the independent code does not account for self-contact. In all cases, both codes predicted the same peak load; in two of them, the post-buckling load path is different. The load-step for independent incremental code that produced the best agreement was $\delta/H = 5x10^{-4}$.

strength, thus smoothing out the results in Figure 4.6, it is difficult to rationalize a selective choice of imperfections on a structure-by-structure basis. Rather, it is likely that the highly non-linear response of structures with very slender interior members is highly sensitive to the orientation of the interior struts. Simply put, smooth variations in response with changes in geometry are often not present.

This indicates that numerical solution algorithms will play a critical role in the development of structures designed to suppress buckling. As an implicit code, in many cases, Pro's independent code can be several orders of magnitude faster than commercial codes. However, consistent numerical parameters (i.e. incrementation schemes) can be difficult to identify, supporting the broad arguments outlined in Chapter 2. Several different load steps were used to make sure results were converged, and in general, a load-step of $\delta/H = 0.0005$ produced very similar results to Abaqus/Explicit. However, the 55° brace does show some notable differences; with the load-step of $\delta/H = 0.0005$, Pro's code found a higher mode solution which buckled around $PL^2/EI = 200$, whereas the solution from Abaqus buckled around $PL^2/EI = 135$. Using a larger load-step, Pro's code was able to find a similar buckling load, but post-buckling solution path without sharp load drops seen in the dynamic simulations. Also note that for both Abaqus and Pro's code, using equal imperfection amplitudes for each mode produced the lowest peak load and lowest energy storage. Therefore, this imperfection strategy was used for the remainder of the simulations.

As one might expect, the response of structures with two sets of angled inner struts is even more complicated, due to the expansion of the design space (i.e. two angles as opposed to one). Figure 4.8 shows maps of peak strength and energy stoage for various strut angle combinations, for various size ratios D/d and two different mass distribution strategies. Again, as a general rule, Strategy A provides slightly better performance, owing to the fact that mass is simply added without reducing the outer strut diameter.

However, the differences are slight and not very systematic; the trend is inverted for some combinations of strut angle, presumably due to subtle interactions between the strut angle and size ratio.

The response across entire two-angle design space is shown in Figure 4.9; emphasis should be placed on normalized strength values above 2.0, since equivalent response below this level can be achieved with the one-angle structures. Considering the throughput of many additive manufacturing practices, adding struts with little gain is to be avoided. The orientations for two-angle structures that perform above this cut-off is also shown in Figure 4.9; there are more points in the complete map (left) than in the angle map (right) because several D/d ratios and mass distribution strategies are shown in the complete map. Broadly speaking, inner strut angles that divide the outer struts into near equal segments are the top performers. However, while this is a useful general rule, improvements can be achieved by angles that divide the outer struts into slightly different lengths. This is discussed in the following section, which presents a global comparison of relative performance across the entire design space (spanning multiple topologies).

4.6 Overview of the design space

An overview of the performance across the entire design space is shown in Figure 4.10 for a relative density of 5%.[7] The map clearly illustrates the trends noted earlier: horizontal braces improve energy storage but do not improve strength, while one-angle inner struts can improve strength by a factor of two and energy storage by 50%. The one-angle structures that are top performers provide mid-point bracing, i.e. 60^o inner struts. For the two-angled structures, the peak strength can be nearly tripled while the energy storage can be nearly doubled; there are clear trade-offs between these two quantities at

[7]While the relative density can vary slightly for mass distribution Strategy A, the variations are modest, and all fall in the range of $5 - 7\%$.

the outer edge of the performance envelope. This is illustrated by comparing the two labeled points, which involve the same large angle inner struts and slightly different small angle inner struts.

Since the peak strength is controlled by buckling and energy storage is controlled by stretching after buckling, the relative density naturally plays a critical role. To illustrate this, calculations were run for mass distribution Strategy C and various relative densities, for a select group of structures that are top (or near top) performers for their topology class. The results are shown in Figure 4.11. Clearly, the benefit of using inner struts is largest for low relative density structures; the effects at higher relative density are rather modest, particularly with regards to energy storage. Note in particular that the mass penalty of horizontal struts at higher relative density completely erases the large gains seen at low relative density.

It is also interesting to note that the single set of 60^o struts outperforms the same with a completed inner triangle, created by including an additional horizontal strut. This is not a relative mass effect; presumably, it is a consequence of the complicated change in buckling mode and subsequent stretching of the inner struts. It is likely that additional struts can promote rotations that reduce stretching after buckling, thereby reducing energy storage.

While great care was taken to include imperfections that promote finding the lowest energy state, it must be acknowledged that some of the complexity of the design space undoubtedly arises from significant differences in imperfection sensitivity associated with strut angle. This highlights the importance of future experiments to corroborate the predictions presented here, and to guide the development of future numerical approaches that correctly identify buckled states.

4.7 Concluding remarks

Numerical results have been presented for the compressive response of 'V' structures braced with different types of inner struts, spanning multiple mass distribution strategies. Despite the sensitivity of the response to small relative changes in inner strut properties, the results support several general conclusions:

1. Placing all of the mass in the main struts of a lattice does not necessarily yield the optimal design for low density, elastic structures whose response is dominated by buckling. Removing mass from the outer struts to form inner struts can lead to higher strengths and higher energy storage relative to the base structure.

2. Horizontal braces do not increase the initial buckling stress, but allow for more energy storage because of a positive tangent modulus (geometric hardening) after the onset of buckling. This is presumably a consequence of stretching induced by asymmetric buckling shapes. Even highly slender horizontal struts can be effective, increasing the energy storage by a factor of two. On a per weight basis, optimal performance is achieved with three struts, due to the fact that inner struts near the ends of the outer struts do not experience significant deformation (and hence represent an inefficient use of mass).

3. Angled braces lead to improvements in both strength and energy storage. Most notably, a single set of 60° inner struts leads to a doubling of the buckling stress due to suppression of the first buckling mode. That said, a single set of struts does not significantly improve post-buckling stability, leading to modest gains in energy storage. In contrast, inner struts with 30^o angles provide more greater post-buckling stability and hence energy storage, without significant improvement in strength.

4. Structures with braces at multiple angles produce the largest gains in performance, offering both increase in peak strength and post-buckling stability (energy storage). For instance, adding braces at both 40° and 70° leads to a factor of about three strength increases and almost a factor of two for energy storage. For topologies with multiple angles, there are likely significant trade-offs between strength and energy storage due to subtle differences in buckling mode and post-buckling stretching of interior struts.

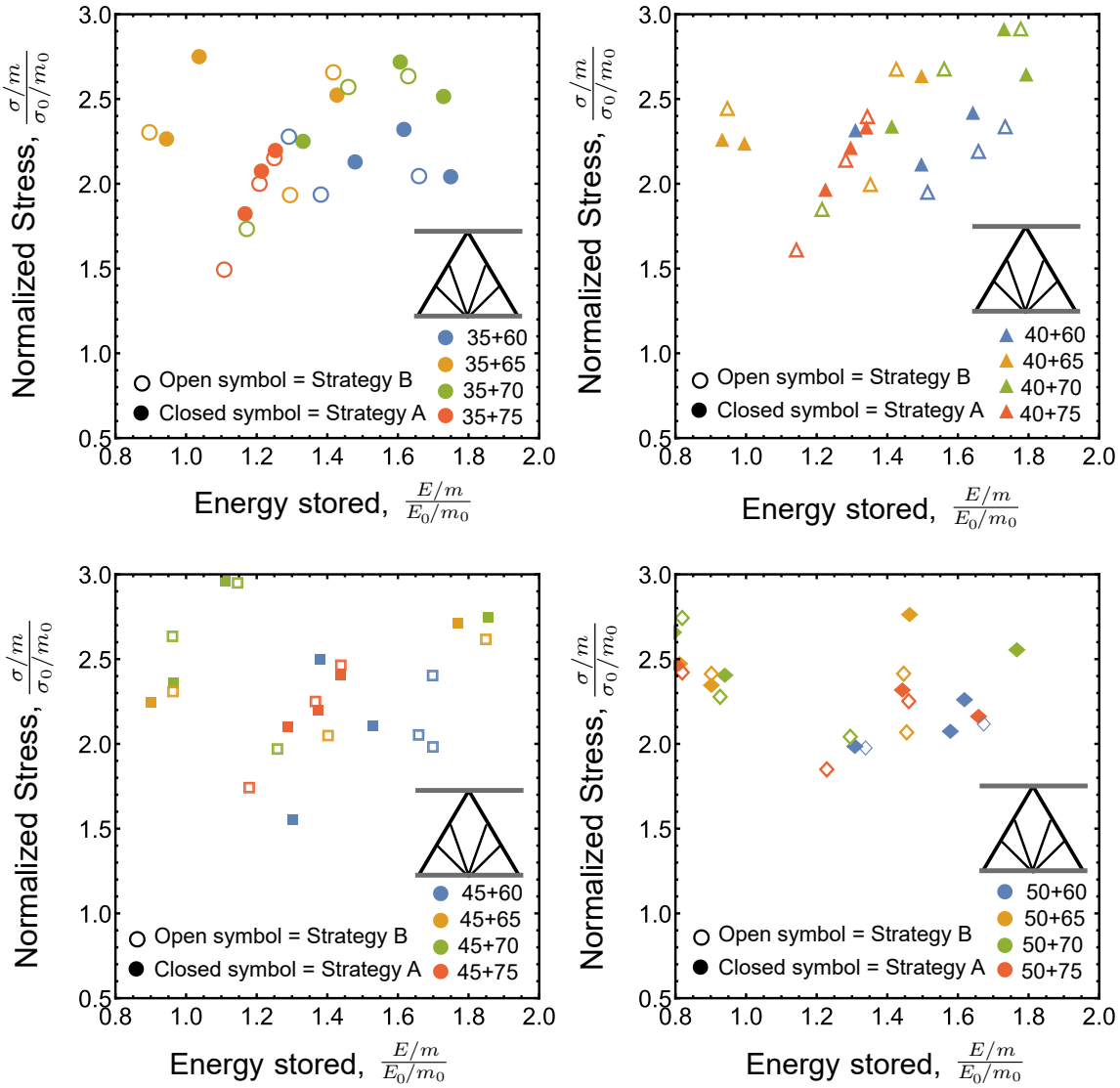

Figure 4.8: Map illustrating peak load and energy stored for several combinations of various two angled interior struts, and $D/d = 2, 4, 8$, using mass distribution strategy A and B.

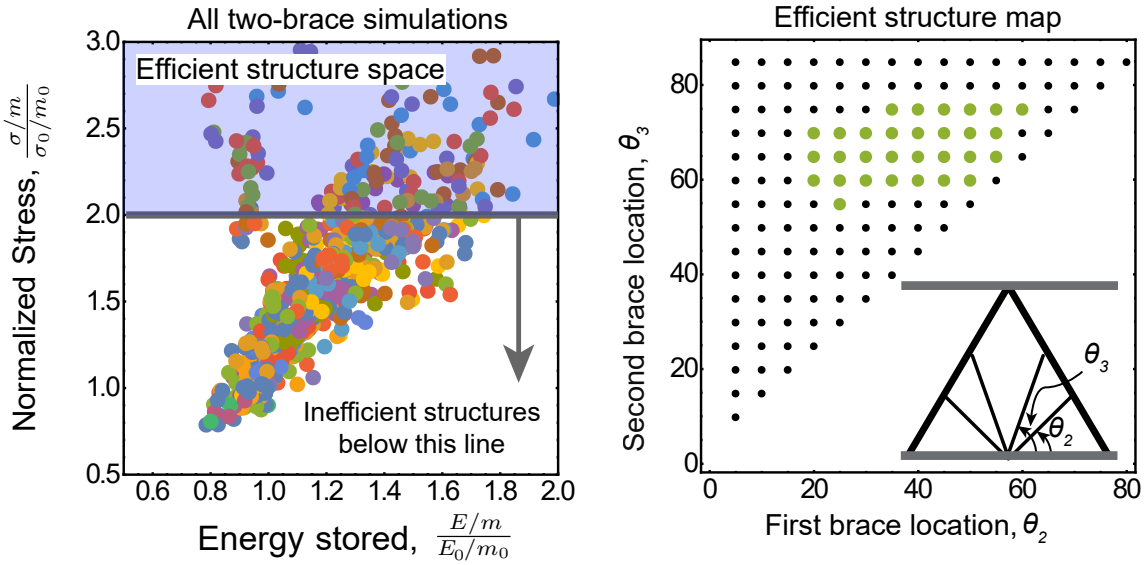

Figure 4.9: Simulations for two angled interior struts at all possible combinations between 5^o and 85^o in 5^o increments. Emphasis placed on obtaining results above the 2.0 line on the ordinate (left) for improved performance over the one brace structures. When that filter is applied, combinations highlighted in green (right) are classified as efficient.

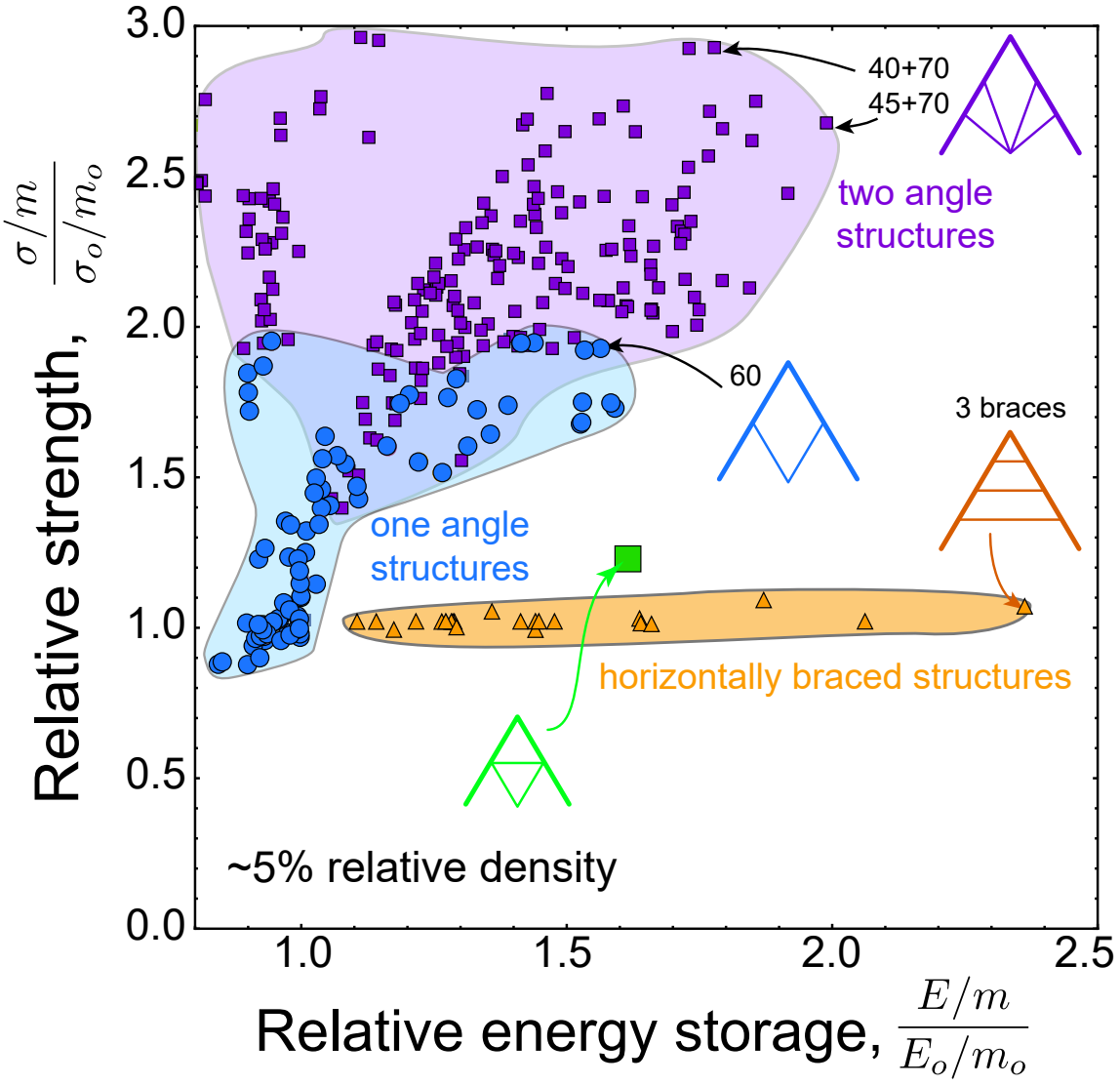

Figure 4.10: Global design map showing the performance of each topology class examined. Two angle brace structures show the highest specific performance in strength due to the first buckling mode suppression.

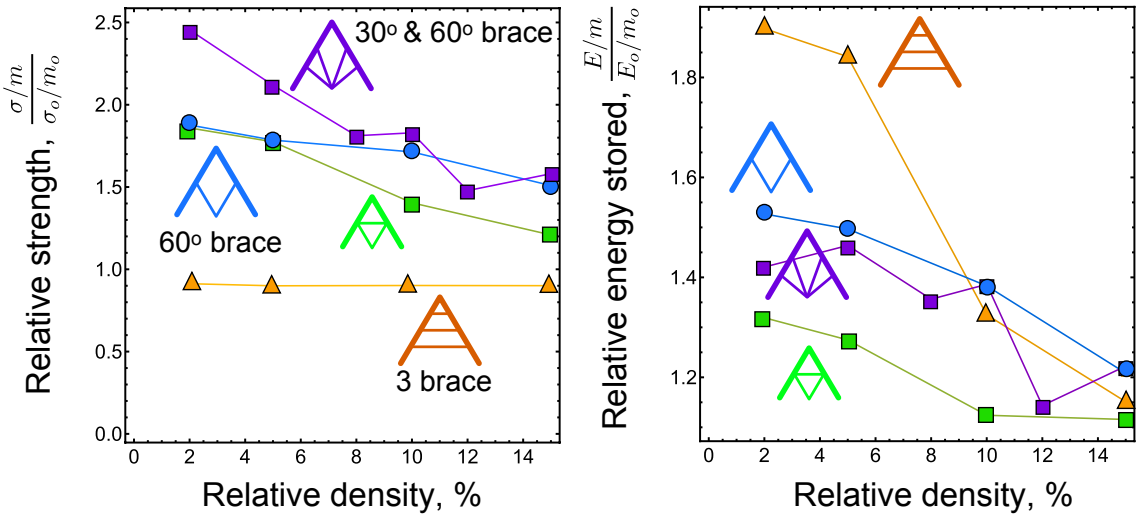

Figure 4.11: Performance metrics as a function of relative density, for mass distribution Strategy C, illustrating that inner struts provide the largest relative benefit for low density structures.

Chapter 5

Damping in cellular materials made from composite struts with elastic and viscoelastic phases

5.1 Introduction

While the static response of cellular materials has been exhaustively studied, their structural dynamic response is far less characterized. Given that additive manufacturing enables a virtually limitless range of component shapes comprising lattices, there is a critical need to understand their dynamic response for applications such as vibration isolation and noise reduction. Further, the ability to make composite walls (struts) – by coating members, filling hollow members with a second phase, or direct co-printing of two materials [68–70] – creates new opportunities to integrate viscoelastic material to improve damping performance. This work addresses two central questions in this area: (*i*) what are the properties of composite walls and struts that lead to significant increases in damping in cell walls, and (*ii*) what is the macroscopic, steady-state dynamic response

of honeycombs comprising such walls?

The focus of this work is on the steady-state structural response of cellular structures subjected to harmonic loading, where the structures consist of dozens (or at most hundreds) of cells. This is in contrast to applications that utilize cells at a finer scale (e.g. thousands to millions of cells) to control higher frequency wave propagation. With this focus, it is important to note that structural dynamic response is inherently tied to component dimensions, which dictate natural frequencies associated with vibration. These frequencies are typically much lower than those associated with wave propagation through a lattice.

In typical analyses of structural vibration, damping is introduced as a heuristic structural property without explicit connections to intrinsic material properties. For instance, a common approach is to include 'proportional damping', which introduces a velocity-dependent dissipative term to discretized dynamics equations that are proportional to the mass or stiffness matrix (or both). A fundamental limitation of such global approaches is that they make it exceedingly difficult to independently identify the impact of specific changes to lattice topology and material composition.

To overcome this limitation, we develop a mechanics-based model for walls (struts) that are made up of a purely elastic phase and a viscoelastic phase. By describing damping as arising from material models, the extrinsic dynamic response of a structure can be determined while holding other intrinsic factors constant. That is, damping is introduced through the dissipative property of the viscoelastic material, which can be characterized independently from vibration experiments conducted at the component level. This effectively decouples the source of damping from the global structural response, such that one can evaluate the performance of various geometries with the same, unambiguous, and independently measurable 'source' of damping.

The paper that follows includes details of the response of composite struts, the fre-

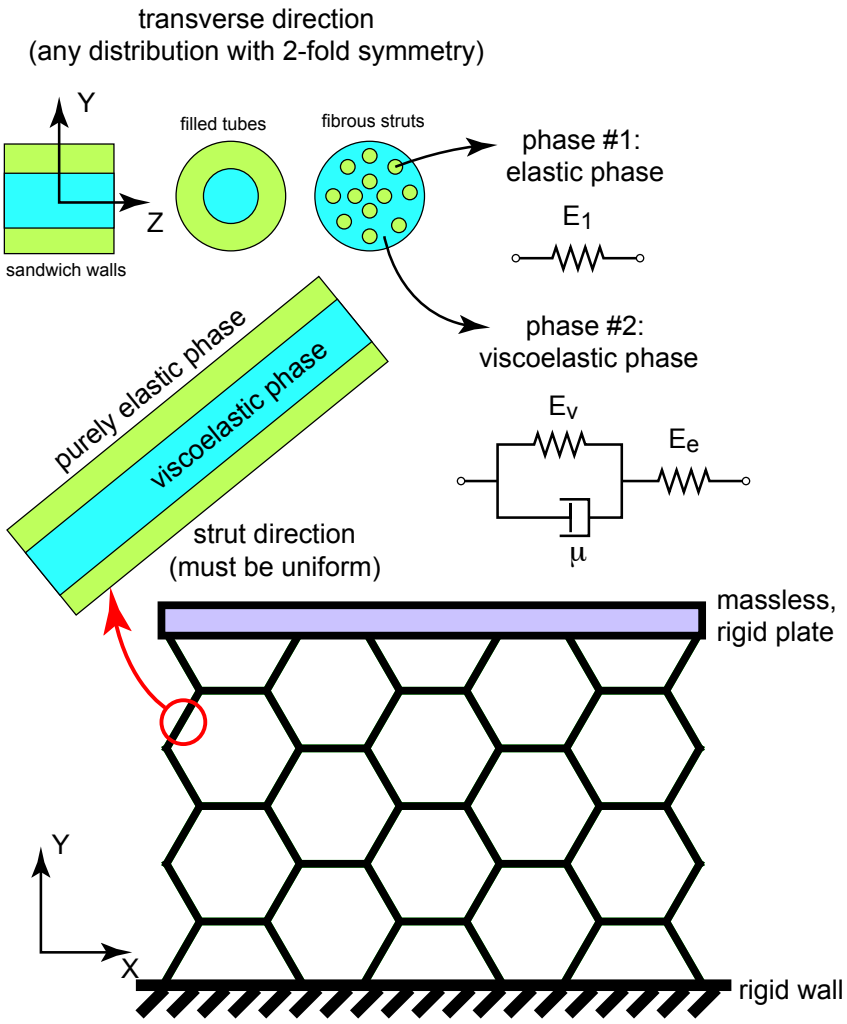

Figure 5.1: A schematic of a two-dimensional prismatic honeycomb with composite walls; the composite consists of a purely elastic phase and a viscoelastic phase. The wall (strut) description developed here is applicable to any wall cross-section with two fold symmetry in a given cross-section, including face sheets separated by a viscoelastic core, filled tubes, etc. The focus of this paper is on the response of the honeycomb when loaded in the (X, Y) plane; the analysis of single walls gives the response loaded in the $Z-$direction.

quency response of individual struts, and a finite element framework that enables efficient simulations of structural dynamic response involving large numbers of cells. These are then used to identify key scaling factors for damping pertinent to cellular structures (in terms of constituent material properties), and illustrations of the effect of composite struts on vibration of honeycomb structures. The analyses presented here focus on compression of prismatic cellular materials in the plane of the cells, as shown in Figure 5.1. Compression parallel to the walls in the $Z-$direction can be predicted using the analysis of the single wall, as elucidated in the sections that follow. Finally, while 2D analyses are presented, the method can be trivially extended to 3D structures with strut-like features.

5.2 Material model

In the following, phase #1 is elastic and has an elastic modulus E_1 and density ρ_1. With suitable interpretation of moduli, the results are applicable for either plate-like walls in prismatic honeycombs, or beam-like struts in open-celled architectures. Phase #2 is a viscoelastic phase that obeys a 'standard linear solid' (or SLS) model, i.e. an elastic spring with modulus E_e in series with a Kelvin-Voigt viscoelastic element, defined by a spring of modulus E_v in parallel with a dashpot with viscosity μ.[1] For this material, the constitutive relationship is given by:

$$\left(1+\frac{E_v}{E_e}\right)\sigma+\frac{\mu}{E_e}\dot{\sigma}=\mu\dot{\epsilon}+E_v\epsilon \tag{5.1}$$

[1]This is the so-called Kelvin representation of the standard linear solid; placing a Maxwell element in parallel with a spring is different representation of the SLS model, but yields virtually identical behaviors.

Alternatively, the above constitutive law can be written as:

$$\sigma = E_e\left(\epsilon - \epsilon_{cr}\right) \tag{5.2}$$

$$\mu\dot{\epsilon}_{cr} + \left(E_v + E_e\right)\epsilon_{cr} = E_e\epsilon \tag{5.3}$$

where ϵ is the total strain, and ϵ_{cr} is the strain in the viscous component. This second form is advantageous for numerical simulations, which track creep strains as a discretized variable and utilize eq. (5.3) as the evolution law for those variables.

The standard linear solid (SLS) model is attractive because it combines the best features of the classical Maxwell and Kelvin-Voigt models. Specifically, it captures: *(i)* an instantaneous elastic response to sudden loading, enabling modeling both creep and relaxation scenarios, *(ii)* reversal of viscoelastic deformations (i.e. eventual full recovery upon full unloading), and *(iii)* a finite limit to deformation under constant loading. This can be understood by recognizing that one recovers a pure Maxwell model in the limit of $E_v \to 0$, such that $\dot{\epsilon} = \dot{\sigma}/E_e + \sigma/\mu$. Conversely, one recovers the Kelvin-Voigt model in the limit that $E_e >> E_v$, such that $\sigma = E_e\epsilon + \mu\dot{\epsilon}$. In the limit of both small E_e and small E_v, the model produces a purely Newtonian viscous response with $\sigma \sim \mu\dot{\epsilon}$.

The parameters of the standard linear solid can be related to storage and loss moduli and the material loss factor η_{mat} as follows. Imposition of a harmonic strain $\epsilon(t) = \epsilon_o e^{i\omega t}$ produces a steady-state stress amplitude with a phase shift, i.e. $\sigma(t) = \sigma_o e^{i(\omega t+\delta)}$. The complex modulus is defined such that:

$$\left(E' + iE''\right)\epsilon_o e^{i\omega t} = \sigma_o e^{i(\omega t+\delta)} \tag{5.4}$$

where E' is the storage modulus, E'' is the loss modulus, and the loss factor is $\eta_{mat} =$

$\tan\delta \equiv E''/E'$. This implies:

$$E' + iE'' = \frac{\sigma_o}{\epsilon_o} e^{i\delta} = \frac{\sigma_o}{\epsilon_o}\cos\delta + i\frac{\sigma_o}{\epsilon_o}\sin\delta \tag{5.5}$$

Solving the differential equation given as eq. (1) for a harmonic strain input allows one to equate the real and imaginary parts of both sides to compute $E' = \sigma_o \cos\delta/\epsilon_o$ and $E'' = \sigma_o \sin\delta/\epsilon_o$. Using the harmonic forms for stress and strain in eq. (1) produces the following:

$$E' + iE'' = \frac{E_v + i\,(\mu\omega)}{1 + \frac{E_v}{E_e} + i\left(\frac{\mu\omega}{E_e}\right)} \tag{5.6}$$

Simplifying the righthand side of the above, the complex moduli and loss factor are given by:

$$E' = \frac{E_e E_v (E_e + E_v) + E_e\,(\mu\omega)^2}{(E_e + E_v)^2 + (\mu\omega)^2};\; E'' = \frac{E_e^2 \mu\omega}{(E_e + E_v)^2 + (\mu\omega)^2};$$
$$\eta_{mat} = \frac{E_e \mu\omega}{E_v(E_e + E_v) + (\mu\omega)^2} \tag{5.7}$$

The loss factor for the viscoelastic material η_{mat} is identical to the conventional loss parameter $\tan\delta$, which reflects the phase shift between input and output for a monolithic material. For the composite *structures* considered in subsequent sections, a structural loss factor will be introduced, which can be, but is not necessarily, the same as the loss factor for the viscoelastic phase itself.

While the frequency dependence of the standard linear material does not closely match that of many materials over all frequencies, it captures the essential trends. Interpreting the inverse of frequency as temperature, the storage modulus E'' falls from E_e at low temperatures (high frequencies) to $E_e E_v/(E_e + Ev)$ at high temperatures (low

frequencies). It should be noted that the elastic response of the material at very low loading frequencies, i.e. when $\mu\omega << \sqrt{E_v(E_e + E_v)}$, is given by:

$$E_2 = \frac{E_e E_v}{E_e + E_v} \tag{5.8}$$

where E_2 is the effective elastic modulus of phase #2 when dissipation is negligible. In the limit of low frequencies, the loss modulus scales with $\mu\omega$. The SLS loss modulus is small at both low and high frequencies (high and low temperatures); it exhibits a peak at the frequency given by:

$$\omega_{max} = \frac{\sqrt{E_v(E_e + E_v)}}{\mu}; \quad \eta_{mat}^{max} = \frac{E_e}{2\sqrt{E_v(E_e + E_v)}} \tag{5.9}$$

If one assumes that the loss factor η_{mat} is known at the frequency associated with maximum dissipation (i.e. the stated loss factor is η_{mat}^{max}), and quasi-static modulus is known, then one can show that that the SLS parameters are defined as:

$$E_e = E_2 \left[1 + 2\eta_{mat}^2 + \sqrt{1 + \eta_{mat}^2}\right] \sim E_2(1 + \eta_{mat}) \tag{5.10}$$

$$E_v = E_2 \left(\frac{1}{2} + \frac{\sqrt{1 + \eta_{mat}^2}}{\eta_{mat}}\right) \sim E_2 \left(\frac{1 + \eta_{mat}}{2\eta_{mat}}\right) \tag{5.11}$$

It should be noted that for a structure made from a composite material, maximum damping may not occur at the frequency associated with maximum dissipation of the viscoelastic phase. Indeed, it will be shown that the maximum damping for composite cell walls occurs at the frequency that maximizes the loss modulus of the viscous phase, not necessarily the frequency that maximizes η_{mat}.

5.3 Strut mechanics

As shown in Figure 5.1, a composite member is considered which consists of purely elastic material defined by an elastic modulus E_1 and density ρ_1, combined with a second material described using the standard linear solid model outlined above with density ρ_2. Internal damping of phase #1 is neglected entirely. The results are completely general in that they can be used to describe any distribution of the two materials, provided each phase has an identical neutral axis. (This is tantamount to the fact that their centers of area are identical.) Hence, the formulation applies to any cross-sectional shape, including filled tubes of circular or rectangular cross-section, struts with embedded continuous viscous fibers, or vice versa (viscoelastic struts with embedded continuous elastic fibers). The results are cased in terms of effective bending stiffness, stretching stiffness, and loss parameters, which can be computed for any phase distribution and any shape.

It is worth noting that a monolithic wall consisting of a viscoelastic material can be modeled simply by defining phase #1 as empty space and utilizing phase #2 properties to describe the wall. This allows one to extract material parameters from structural vibration experiments, although one must naturally take care to consider the presence of other dissipative mechanisms. For two-phase composites, the limitation of the present wall definition is that it neglects damping arising from one of the phases, which is obviously less than desirable if the damping properties of both phases are comparable. That being said, one could extend the present analysis to include multiple viscoelastic phases, at the expense of more extensive bookkeeping. This might be desirable for future work that explores using multiple dissipative materials with different characteristic frequencies to dampen a broader range of frequency space.

For brevity's sake, the focus here is on two-dimensional frameworks, such that the lattice is comprised of plate-like walls rather than struts typical of open-celled structures.

However, the analysis can be easily extended to three-dimensional cases (i.e. struts) simply by repeating the derivation to include additional displacements.

The walls are assumed to obey Bernoulli-Euler beam kinematics in the limit of small deformation; the *total* strain in the wall is $\epsilon(x) = \epsilon_o - \kappa(x)y = u'(x) - w''(x)y$, where $u(x)$ is the axial displacement of the beam centerline, $w(x)$ is the transverse displacement of the beam center line, y is the distance from the neutral axis, x is the distance along the wall axis and primes denote derivatives with respect to space. In the dynamic analysis that follows, rotational inertia is neglected (as consistent with the small slope assumption embedded in small deformation frameworks), but axial and transverse inertia are both included.

The constitutive description given as eqs. (2-3) dictate that the creep strain must also obey a linear distribution through the beam. To see this, consider the response at time zero (corresponding to zero load), when creep strains are zero. Upon an increment in loading over infinitesimal time, the response is purely elastic and stress and strain distributions are linear with respect to the $y-$direction. The evolution equation given as eq. (3) dictates that the initial creep strain rate is therefore also linear, and as such the updated creep strains will also be linear. Hence, the stress in the viscoelastic phase can be written as:

$$\sigma(x, y, t) = E_e \left[u'(x, t) - u'_{cr}(x, t) - \left(w''(x, t) - w''_{cr}(x, t) \right) y \right] \tag{5.12}$$

where $u_{cr}(x, t)$ is an 'axial creep displacement' whose derivative defines the creep strain at the neutral axis (i.e. stretching), and $w''_{cr}(x, t)$ is a 'transverse creep displacement' whose second derivative defines the linear distribution of creep strain (i.e. bending).

Using the above assumptions, the corresponding statement of virtual work is:

$$\int_0^L \left(\int_A \left[\sigma(x,t)\delta\epsilon(x,t) + \rho\ddot{w}(x,t)\delta w(x) + \rho\ddot{u}(x,t)\delta u(x,t) \right] dA \right) dx =$$
$$\int_0^L p(x,t)\delta w(x,t)dx + N_o\delta u_L + N_L\delta u_L + M_o\delta w'_o + M_L\delta w'_L + V_o\delta w_o + V_L\delta W_L \quad (5.13)$$

where $p(x,t)$ is a transverse pressure load applied to the beam, and the last terms reflect externally applied axial forces (N), transverse forces (V) and moments (M) at the ends of the beam.

The neutral axis for each phase is defined by the condition:

$$\int_A E_i y dA = 0 \quad (5.14)$$

where A is the cross-section of the beam and $E_i = E_1$ for the elastic phase and $E_i = E_{e,v}$ for the viscoelastic phase. Here, it is assumed transverse phase distribution has two-fold symmetry about the strut axis, such that both phases have identical neutral axes. With this assumption, the axial and bending responses are decoupled for small deformation, such that the statement of virtual work reduces to two independent equations:

$$\int_0^L \left(\int_{A_t} \left[E_1 u' \, \delta u' + \rho_t \ddot{u} \, \delta u \right] dA + \int_{A_f} \left[E_e (u' - u'_{cr}) \, \delta u' + \rho_f \ddot{u} \, \delta u \right] dA \right) dx$$
$$= N_0 \delta u_0 + N_L \delta u_L \quad (5.15)$$

$$\int_0^L \left(\int_{A_t} \left[E_1 w'' \, y^2 \, \delta w'' + \rho_t \ddot{w} \, \delta w \right] dA + \int_{A_f} \left[E_e (w'' - w''_{cr}) y^2 \, \delta w'' + \rho_f \ddot{w} \, \delta w \right] dA \right) dx$$
$$= \int_0^L p \delta w \, dx + M_o \delta w'_o + M_L \delta w'_L + V_o \delta w_o + V_L \delta w_L \quad (5.16)$$

where the explicit reference to time and position has been dropped. A_1 is the cross-sectional area of the elastic phase, while A_2 is that of the viscoelastic phase. Let $\overline{EI} =$

$E_1 I_1 + E_e I_2$ present a composite bending stiffness of the beam with $I_{1,2}$ defined in the usual fashion[2]. Further, let $\overline{EA} = E_1 A_1 + E_e A_2$ represent a composite stretching stiffness of the beam, while $\overline{\rho A} = \rho_1 A_1 + \rho_2 A_2$ is the composite mass per unit length of the beam. In this case, the above simplifies to:

$$\int_0^L \left[\left(\overline{EA} u' - E_e A_2 u'_{cr} \right) \delta u' + \overline{\rho A} \ddot{u} \delta u \right] dx = N_o \delta u_L + N_L \delta u_L \tag{5.17}$$

$$\int_0^L \left[\left(\overline{EI} w'' - E_e I_2 w''_{cr} \right) \delta w'' + \overline{\rho A} \ddot{w} \delta w \right] dx =$$

$$\int_0^L p \, \delta w \, dx + M_o \delta w'_o + M_L \delta w'_L + V_o \delta w_o + V_L \delta w_L \tag{5.18}$$

These equations can be integrated by parts to yield the coupled space-time PDEs that govern the response; in addition, they provide the basis for a finite element representation described later. In bending, integration by parts yields the governing equations:

$$\overline{EI} w'''' - E_e I_2 w''''_{cr} + \overline{\rho A} \ddot{w} = p \tag{5.19}$$

$$\mu \dot{w}''_{cr} + (E_e + E_v) w''_{cr} - E_e w'' = 0 \tag{5.20}$$

where the second equation is the evolution of transverse creep displacements, obtained from the constitutive law for the material. The boundary conditions are given by:

$$\overline{EI} w''(0,t) - E_e I_2 w''_{cr}(0,t) = M_0(t); \quad \overline{EI} w''(L,t) - E_e I_2 w''_{cr}(L,t) = M_L(t) \tag{5.21}$$

$$\overline{EI} w'''(0,t) - E_e I_2 w'''_{cr}(0,t) = V_0(t); \quad \overline{EI} w''(L,t) - E_e I_2 w''_{cr}(L,t) = V_L(t) \tag{5.22}$$

The axial governing equations are obtained in a similar fashion, and yield the following

[2]Note that this is not the bending stiffness of the beam at zero frequency; this would be $E_1 I_1 + E_2 I_2$.

governing equations:

$$\overline{EA}u'' - E_e A_2 u''_{cr} + \overline{\rho A}\ddot{u} = 0 \tag{5.23}$$

$$\mu\dot{u}'_{cr} + (E_e + E_v)u'_{cr} - E_e u' = 0 \tag{5.24}$$

with boundary conditions given by:

$$\overline{EA}u'(0,t) - E_e A_2 u'_{cr}(0,t) = N_0(t); \quad \overline{EA}u'(L,t) - E_e A_2 u'_{cr}(L,t) = N_L(t) \tag{5.25}$$

Despite their simplicity, the partial differential equations described above do not have analytical solutions except in highly idealized loading scenarios, notably boundary conditions that are independent of time. Even the simple case of a wall subjected to harmonic end forces or moments defies an exact solution, due to the non-homogeneous boundary conditions implied by time-dependent boundary conditions. The difficulty can be realized immediately by comparing the quasi-static bending response with the first natural frequency. For example, consider a wall pinned at both ends and subjected to applied moments; this is identical to a 4-point bending experiment. The static bending deflection varies as $\bar{x}(1-\bar{x})$, while the first mode shape varies as $\sin \pi\bar{x}$. Hence, the spatial response depends on the loading frequency in a non-trivial way. For this reason, approximate solutions are developed to provide insight regarding the scaling controlling wall dynamics. Then, a framework for full numerical solutions is presented in later sections.

5.4 Bending vibration of a cell wall: approximate solution

We consider the response of a wall that is pinned at both ends and subjected to harmonic applied moments at the ends. To illustrate the nature of coupling between inertial and viscous time scales, the SLS model is used to describe a uniform wall; the impact of composite walls is considered in subsequent sections. For small deformations, axial and transverse displacements are decoupled and can be dealt with separately. As stated above, the PVW for the bending response is:

$$\int_0^L \left[E_e I \left(w'' - w''_{cr}\right) \delta w'' + \rho A \ddot{w} \delta w\right] dx = M_o \delta w'_o + M_L \delta w'_L \tag{5.26}$$

$$\mu \dot{w}''_{cr} + (E_e + E_v) w''_{cr} - E_e \bar{w}'' = 0 \tag{5.27}$$

where $(\,)'$ denotes spatial derivatives and $\dot{(\,)}$ denotes derivatives with respect to time; M_o and M_L are the applied moments at the ends. An approximation solution is developed based on assuming a fixed spatial variation in displacements with a time-dependent amplitude, e.g. $w(x,t) = w_o(t) f(x)$.

The principal focus is on wall responses to excitation frequencies that are below the second natural frequency of the wall, where one can expect the first mode-shape to be a dominant contributor to the response. Assume that $w(x,t) = w_o(t) \sin \pi x/L$, i.e. the spatial distribution of displacements agrees with the first free vibration mode shape. Similarly, assume $w_{cr}(x,t) = w_o^{cr}(t) \sin \pi x/L$. Using this in the above, we obtain:

$$\frac{\pi^4}{2} \frac{E_e I}{L} \left(w_o - w_o^{cr}\right) + \frac{1}{2} \rho A L \ddot{w}_o = 2 \frac{\pi}{L} M_a \tag{5.28}$$

$$\mu \dot{w}''_{cr} + (E_e + E_v) w''_{cr} - E_e \bar{w}'' = 0 \tag{5.29}$$

where M_a is the magnitude of the moments applied to the ends, which cause opposite rotations; the pre-factor π on the righthand side arises from $\delta w_o' = \delta w_o(\sin \pi x/L)'$. Define the following:

$$\omega_o = \pi\sqrt{\frac{E_e I}{\rho A L^4}}; \quad r = \frac{E_e}{E_v}; \quad \xi = \frac{\mu\omega_o}{E_e(1+r)} = \frac{\mu\omega_o}{E_e + E_v}; \quad \tilde{M} = \frac{4}{\pi^3}\frac{M_a L}{E_e I} \tag{5.30}$$

Note that ω_o is the first natural frequency for an undamped pinned-pinned beam. Further, let $\Delta = w_o/L$ and $\Delta_{cr} = (1+r)w_o^{cr}/L$. The governing equations stated above simplify to:

$$\Delta - \frac{1}{1+r}\Delta_{cr} + \ddot{\Delta} = \tilde{M} \tag{5.31}$$

$$\xi\dot{\Delta}_{cr} + \Delta_{cr} - r\Delta = 0 \tag{5.32}$$

Note that the quasi-static response is given by:

$$\left(1 - \frac{r}{1+r}\right)\Delta = \tilde{M} \tag{5.33}$$

$$\Delta = \frac{4}{\pi^3}(1+r)\frac{M_a L}{E_e I} \tag{5.34}$$

$$\Delta = \frac{4}{\pi^3}\left(\frac{E_e + E_v}{E_v}\right)\frac{M_a L}{E_e I} \tag{5.35}$$

$$\Delta = \frac{4}{\pi^3}\frac{M_a L}{EI} \tag{5.36}$$

where $E = E_e E_v/(E_e + E_v)$ is the elastic modulus of the SLS model at zero loading rate. The pre-factor for the exact elasticity solution is 1/8; hence, the approximate quasi-static solution with its pre-factor of $4/\pi^3 \approx 1/7.75$ is within 3.3% of the exact quasi-static solution.

The solution for steady-state harmonic excitation can be found as follows. It is

convenient to write the dynamic governing equations as:

$$\begin{bmatrix} 1 & 0 \\ 0 & 0 \end{bmatrix} \begin{pmatrix} \ddot{W} \\ \ddot{W}_{cr} \end{pmatrix} + \begin{bmatrix} 0 & 0 \\ 0 & \xi \end{bmatrix} \begin{pmatrix} \dot{W} \\ \dot{W}_{cr} \end{pmatrix} + \begin{bmatrix} 1 & 1/(1+r) \\ -r & 1 \end{bmatrix} \begin{pmatrix} W \\ W_{cr} \end{pmatrix} = \begin{pmatrix} \widetilde{M}(\tau) \\ 0 \end{pmatrix} \quad (5.37)$$

Consider the steady-state response to harmonic applied moments at the ends, e.g. $\tilde{M}e^{i\Omega\tau}$, where $\tilde{M}$ now represents the amplitude of the applied moment and $\Omega = \omega_{ex}/\omega_n$ is the dimensionless excitation frequency. The response can be written as $\Delta e^{i(\Omega\tau)}$ where $\Delta = C_r + iC_i$ now represents the output displacement amplitude in complex form; C_r is interpreted as the storage compliance, and C_i is interpeted as the loss compliance. It is a compliance since the output displacement will be $(C_r + iC_i)\tilde{M}e^{i\Omega\tau}$. This is equivalent to stating that the output will have amplitude $|\Delta| = \sqrt{C_r^2 + C_i^2}$ and phase shift given by $\tan\delta = C_i/C_r$. Similarly, the output creep displacement can be described by $\Delta_{cr}e^{i\Omega\tau}$ where $\Delta_{cr} = D_r + iD_i$ its the output creep displacement in complex form.

Using these assumed forms of the solution in the above governing equations, one obtains:

$$\begin{bmatrix} -\Omega^2 & 0 \\ 0 & 0 \end{bmatrix} \begin{pmatrix} \Delta \\ \Delta_{cr} \end{pmatrix} + \begin{bmatrix} 0 & 0 \\ 0 & i\Omega\xi \end{bmatrix} \begin{pmatrix} \Delta \\ \Delta_{cr} \end{pmatrix} + \begin{bmatrix} 1 & 1/(1+r) \\ -r & 1 \end{bmatrix} \begin{pmatrix} \Delta \\ \Delta_{cr} \end{pmatrix} = \begin{pmatrix} \widetilde{M} \\ 0 \end{pmatrix} \quad (5.38)$$

This can be solved to obtain complex expressions for Δ and Δ_{cr}. Note that they assured to have both real and complex components because of the presence of the imaginary number in the damping matrix.

The solution, in terms of the output displacement amplitude and phase shift, is put into its most compact form by defining $\beta = 1 + r$. Also, note that the true static displacement (without any approximation) is given by:

$$\frac{w_{st}}{L} = \frac{1}{8}\frac{ML}{EI} = \frac{\pi^3}{32}\beta\tilde{M} \tag{5.39}$$

The ratio of output displacement to the exact static result is given by the frequency response function:

$$FRF = \frac{w}{w_{st}} = \frac{32}{\pi^3}\sqrt{\frac{1+\xi^2\Omega^2}{\xi^2\beta^2\Omega^2\left(1-\Omega^2\right)^2 + \left(1-\beta\Omega^2\right)^2}} \tag{5.40}$$

The pre-factor is $32/\pi^3 \approx 1.03$. This allows for direct comparison with FEA results presented later, which are expected to accurately describe both quasi-static and dynamic results. The phase shift between displacement and applied moment is given by:

$$\tan\delta = -\frac{\left(\beta-1\right)\beta\xi\Omega}{1+\beta\Omega^2\left(\beta\left[\Omega^2+\xi\left(1-\Omega^2\right)^2\right]-2\right)} \tag{5.41}$$

In the limit of zero frequency, one obtains $FRF = 1$, as expected. More generally, the frequency response is analogous to that of a spring-mass-damper system, rising to a peak and then falling, as shown in Figure 5.2A. However, there is a critical and substantial difference; increasing the viscosity parameter ξ does not decrease the resonant peak for all values of ξ. This is shown in Figure 5.2B. Unlike a conventional mass-spring-damper system, there is an optimal viscosity that minimizes the resonance response, and increasing the viscosity past this optimal point leads to *increases* in peak response. While one can solve for the damped natural frequency and peak response with *Mathematica* or something similar, the analytical result is unwieldy and not very insightful. (The reason for this is that it involves a cubic polynomial in Ω^2, not quadratic as for a convential

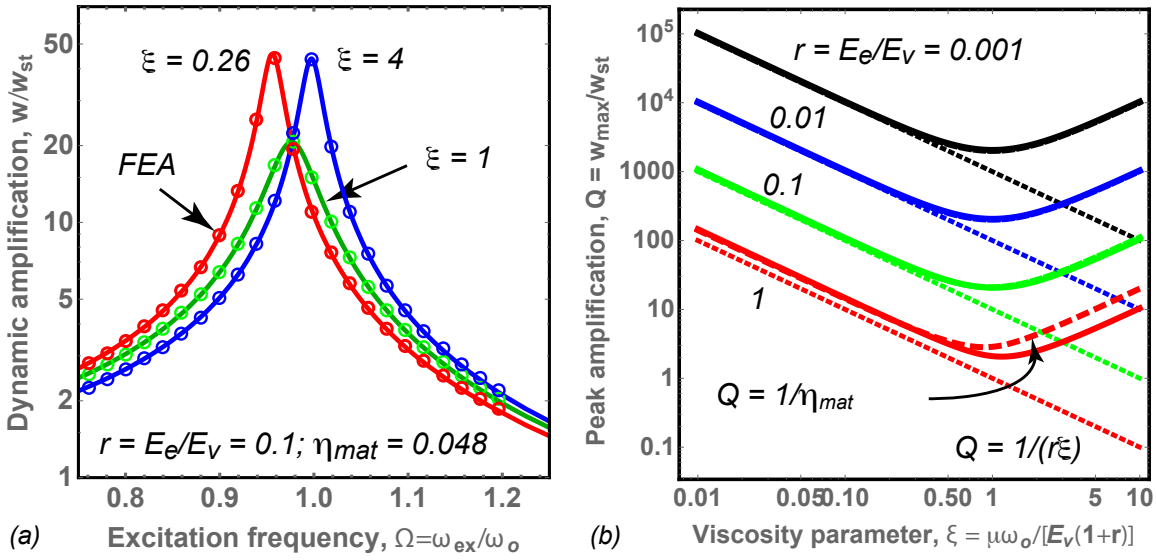

Figure 5.2: (A) The frequency response of a single wall, pinned at both ends and subjected to pure bending; the lines represent the 1DOF model, the circles represent full FEA results. Several levels of viscosity $\xi = \mu\omega_o/(E_e + E_v)$ are shown. (B) The peak amplification Q as a function of viscosity parameter and various $r = E_e/E_v$ values. The solid lines are the 1DOF model, the dashed lines are $Q = 1/\eta_{mat}$ and the dotted lines are $Q = 1/(r\xi)$.

damped oscillator.) For this reason, the results shown in Figure 5.2 were determined numerically by maximizing the analytical FRF.

It should be noted that the *structural* phase shift goes through zero at resonance, unlike the *material* loss factor η_{mat}. Hence, to compare the level of damping in the structure to that of the material, the effective damping level should be estimated from Q, the peak (resonant) amplification. One can re-cast the *material* description in terms of r and ξ as follows:

$$\eta_{mat} = \frac{r\xi\Omega}{1 + (1+r)\,\xi^2\Omega^2} \tag{5.42}$$

Figure 5.2 illustrates that for light damping, the 1DOF approximation is virtually identical to $Q \approx 1/\eta_{mat}$. Furthermore, when $\xi << 1$, the system is 'de-tuned' in the sense

that the natural frequency of material is much smaller than that of the structure; in this limit, the Q-factor is well approximated by $Q = 1/(r\xi) = 1/\eta_{mat}$.

A comparison between the structural loss factor Q^{-1} and material loss factor η_{mat} is shown in Figure 5.3, based on the 1DOF model and finite element results (obtained via the framework in subsequent sections). To create the figure, the loss factor of the material η_{mat} and its elastic modulus $E_eE_v/(E_e+E_v)$ were prescribed and then used to solve for E_e and E_v explicitly. The viscosity parameter was then chosen such $\xi = \mu\omega_o/(E_e + E_v) = 1$, such that the characteristic material and structural frequencies are matched. The ratio $r = E_e/E_v$ (or $\beta = 1 + r$) used in the analytical FRF expression given above are fully defined through E_e and E_v. The analytical FRF expression was then solved numerically for the maximum amplification factor, Q. These results reflect the optimal level of structural damping that can be achieved, i.e. peak responses near the minimum shown in Figure 5.2b.

The results clearly show the 1DOF model is in excellent agreement with FEA results, with less than 1% error. Further, it is clear that the approximation that structural damping scales as $Q^{-1} \sim \eta_{mat}$ is only valid for $\eta_{mat} < \sim 0.1$. It should be kept in mind that these results are for bending near the first natural frequency. The axial response is similar, with slight variations illustrated in the next section.

5.5 Axial vibration of a viscoelastic wall

Here, the analysis of a wall subjected to pure bending is repeated for a wall subjected to purely axial response. Consider a uniform bar of a viscoelastic material subjected to a cyclic force at its end; again, the material is described with the standard linear model, defined by two moduli, E_e and E_v and a viscosity μ. For axial vibrations, the statement

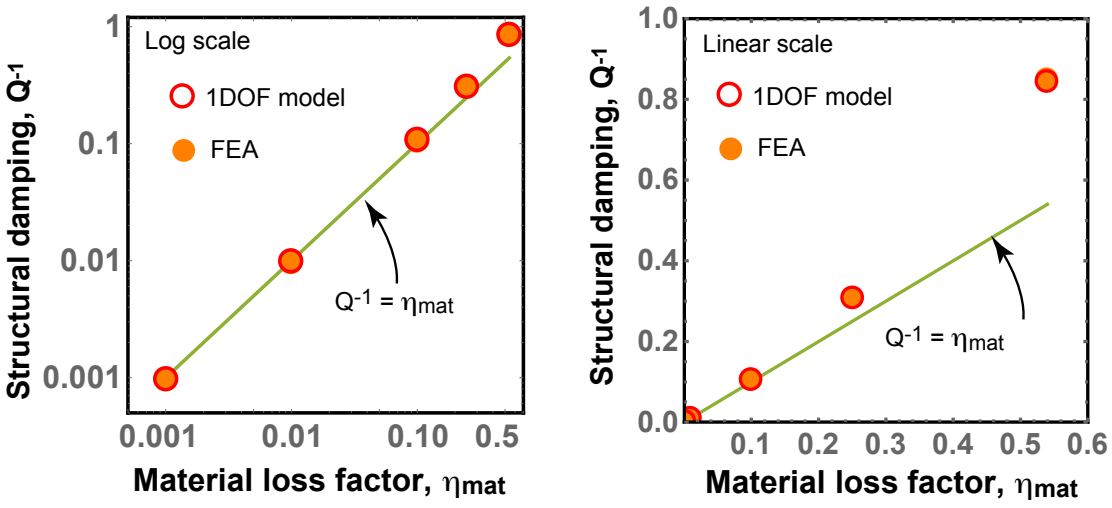

Figure 5.3: A comparison of structural damping in bending with the material loss factor, for 'tuned' structures where $\xi = \mu\omega_o/(E_e + E_v) = 1$. The moduli E_e and E_v are found by prescribing the zero-rate elastic modulus $E_eE_v/(E_e+E_v)$ and η_{mat}, then solving for the μ value that matches the $\xi = 1$ condition. The 1DOF model has less than 1% error as compared to a convergent FEA analysis (10 elements). For materials with loss factors $\eta_{mat} > \sim 0.56$, bending vibration is over-damped, i.e. the static displacement represents the peak response.

of PVW is:

$$\int_0^L \left[E_e A\left(u' - u'_{cr}\right)\delta u' + \rho A \ddot{u}\delta u\right] dx = N_0\delta u_0 + N_L \delta u_L \tag{5.43}$$

$$\mu \dot{u}'_{cr} + (E_e + E_v)u'_{cr} = E_e u' \tag{5.44}$$

A simple approximation for the dynamic response of the bar can be developed as follows. Let $\bar{x} = x/L$, $u = u_o \sin \pi\bar{x}/2$ and $u_{cr} = u^o_{cr} \sin \pi\bar{x}/2$. This is, in essence, a finite element model with one element that uses an interpolation function consisting of a half-wave in the bar. The variables $u_o(t)$ and $u^o_{cr}(t)$ define the amplitude of the total displacement and axial creep displacement, respectively. Eq. (5.43) becomes:

$$\frac{\pi^2}{8}\frac{E_e A}{L}\left(u_o - u^o_{cr}\right) + \frac{1}{2}\rho A L \ddot{u}_o = N_L \tag{5.45}$$

$$\mu \dot{u}^o_{cr} + (E_e + E_v)u^o_{cr} = E_e u_o \tag{5.46}$$

In a similar fashion to the earlier bending analysis, let $\Delta = u_o/L$ and $\tilde{N} = N_L/E_e A$. Define $r = E_e/E_v$, and $\Delta_{cr} = (1 + r)u^o_{cr}/L$, along with the following dimensionless parameters:

$$\omega_o = \frac{\pi}{2}\sqrt{\frac{E_e A}{\rho A L^2}}; \quad \tau = \omega_o t; \quad \xi = \frac{\mu\omega_o}{E_e(1+r)} = \frac{\mu\omega_o}{E_e + E_v}; \quad \tilde{N} = \frac{8}{\pi^2}\frac{N}{E_e A} \tag{5.47}$$

In their final form, governing equations are identical to the bending case:

$$\Delta - \frac{\Delta_{cr}}{1+r} + \ddot{\Delta} = \tilde{N} \tag{5.48}$$

$$\xi\dot{\Delta}_{cr} + \Delta_{cr} - r\Delta = 0, \tag{5.49}$$

and as a result, the frequency response solution is identical to the bending case presented earlier.

There is one critical difference, however; the frequency response ratio (i.e. the ratio of output displacement to the exact static result) is given by:

$$FRF = \frac{u}{u_{st}} = \frac{8}{\pi^2}\sqrt{\frac{1+\xi^2\Omega^2}{\xi^2\beta^2\Omega^2\left(1-\Omega^2\right)^2+\left(1-\beta\Omega^2\right)^2}} \tag{5.50}$$

The pre-factor of $8/\pi^2 \approx 0.81$ arises from the difference between the approximation and the exact solution in the quasi-static limit. Again, using the exact static result to normalize the output allows for direct comparison with FEA results (generated via the framework described in a subsequent section), which are accurate in both quasi-static and dynamic scenarios.

Following the analysis done for bending, this implies the structural loss factor for axial deformation is given by $Q^{-1} = (\pi^2/8)\eta_{mat} = 1.23\eta_{mat}$. That is, the structural loss factor for axial deformation is slightly higher than for bending, and interestingly, slightly higher than the material's loss factor. This somewhat surprising result from the 1DOF model is fully confirmed by finite element calculations; Figure 5.4 shows a comparison of the structural loss factor obtained from the 1DOF model and FEA, as a function of the material loss factor. Again, these results were created by specifying the zero-rate elastic modulus of the rod and the material loss factor in order to compute E_e and E_v. Once E_e and E_v are obtained, the viscosity is set to 'tune' the material damping frequency that of the rod, such that $\xi = \mu\omega_o/(E_e + E_v) = 1$. Clearly, the 1DOF damping estimate is in excellent agreement with the FEA; both show slightly higher effective damping levels than η_{mat} by the exact amount predicted by the half-sine approximation. Though not shown, the spatial distribution of displacements and creep strains obtained from the FEA are also virtually identical to the half-wave approximation of the 1DOF model. Furthermore, if one computes the ratio of work dissipated per cycle and maximum stored elastic energy during a cycle, and defines loss factor as $Q^{-1} = \Delta W_d/(2\pi W_e^{max})$,

one obtains the same result that $Q^{-1} = 1.23\eta_{mat}$. Simply put, the different pre-factor relating structural and material loss factors is not numerical error or inconsistencies with conventional loss-factors.

The slight increase in damping is clearly a result of distributed inertial forces within the damping material itself. If one analyzes a viscoelastic *but massless* bar that is connected to a lumped mass at the end, the above analysis produces $Q^{-1} = \eta_{mat}$ for low levels of damping. This is true regardless of the size of the lumped mass and whether the viscosity is 'tuned' to meet the natural frequency of the system. In this scenario, the strain in the massless rod is uniform at any instant of time, as demanded by the equilibrium description for the rod (which does not involve inertia). Hence, the root cause of the pre-factor lies in the difference between the static displacement distribution $u \sim \bar{x}$ (which occurs in the lumped mass scenario) and the wave displacement distribution $u \sim \sin \pi\bar{x}/2$ (which occurs in the distributed mass scenario). Note that the average displacement from the dynamic profile is $4/\pi$, which is 27% higher than that from for the static case (assuming the end displacements from both models are matched). Hence, the distributed mass case has higher average deformation than that predicted by assuming strains are uniform (e.g. neglecting inertia). By comparison, for a pinned-pinned beam, the quasi-static and dynamic displacement are virtually identical; hence, inertial effects have a negligible impact on damping for bending.

5.6 Finite element implementation

The finite element model developed here mirrors the derivation of strut behavior presented earlier, and uses conventional interpolation functions for displacements. That is, linear interpolation functions are used for axial displacements and cubic interpolation are used for transverse displacements, typical of Bernoulli-Euler beam elements.

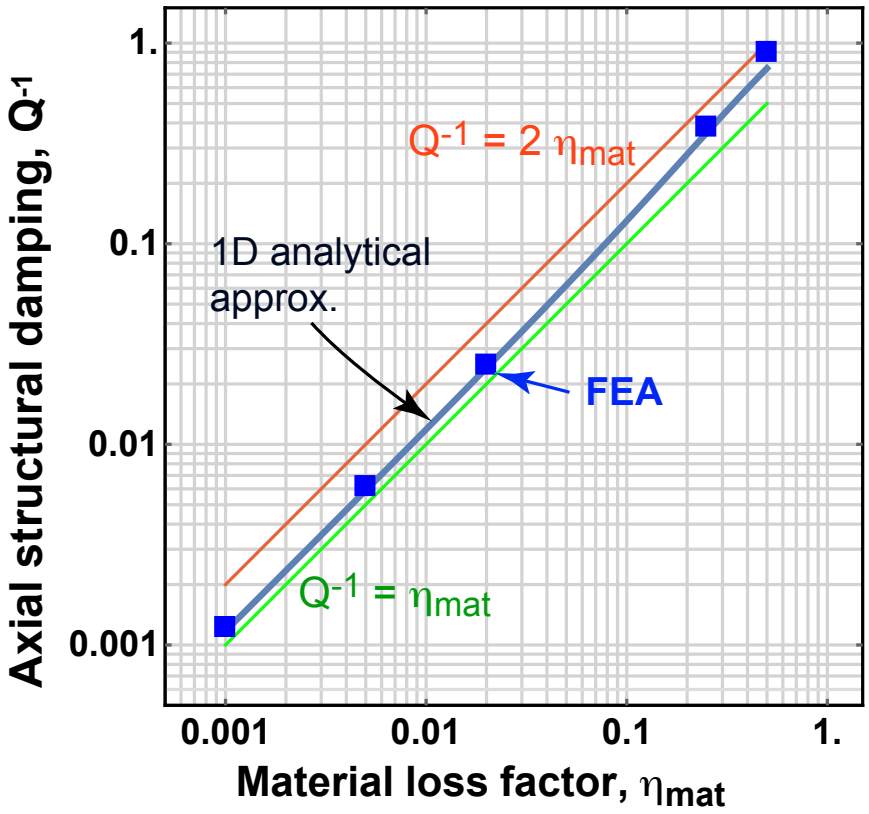

Figure 5.4: Structural loss factors for axial vibration in a wall that is pinned at one end and loaded at the other end with a harmonic force, assuming "tuned" damping where $\xi = \mu\omega_n/(E_e + E_v) = 1$. The resonant amplification factor (i.e. the output displacement amplitude normalized by the quasi-static result) was found by sweeping through frequencies and choosing the largest amplitudes. Results are for a constant value of $E_2 = E_e E_v/(E + e + Ev)$ and various η_{mat} values.

The presence of creep (viscoelastic) displacements in the formulation implies that the beam elements will have six degrees of freedom per node: u, w, θ representing total displacements, and $u_{cr}, w_{cr}, \theta_{cr}$ representing creep displacements that account for internal dissipation.

5.6.1 Elemental matrices for walls in local coordinates

First, consider discretization of the axial equation. Let $\xi = x/\ell$ be a dimensionless coordinate along the beam, and use linear interpolation for the axial displacements, i.e. $u(\xi) = u_1(1-\xi) + u_2\,\xi$. We use an identical interpolation for the creep displacements, i.e. $u_{cr}(\xi) = u_1^{cr}(1-\xi) + u_2^{cr}\,\xi$. Noting that $\ell d/dx = d/d\xi$, and $\delta u_o = \delta u_1$, and $\delta u_\ell = \delta u_2$, integration of the statement of virtual work for axial displacements produces the following two equations:

$$\frac{\overline{EA}}{\ell}\begin{bmatrix} 1 & -1 \\ -1 & 1 \end{bmatrix}\begin{bmatrix} u_1 \\ u_2 \end{bmatrix} - \frac{E_e A_2}{\ell}\begin{bmatrix} 1 & -1 \\ -1 & 1 \end{bmatrix}\begin{bmatrix} u_1^{cr} \\ u_2^{cr} \end{bmatrix} + \overline{\rho A}\,\ell\begin{bmatrix} 1/3 & 1/6 \\ 1/6 & 1/3 \end{bmatrix}\begin{bmatrix} \ddot{u}_1 \\ \ddot{u}_2 \end{bmatrix} = \begin{bmatrix} N_1 \\ N_2 \end{bmatrix} \tag{5.51}$$

We use a weighted residual method to minimize the average error of the evolution equation describing creep displacements. This effectively translates the spatially-dependent evolution equation into corresponding evolution equations for nodal values. The weight functions in the weight residual approach are chosen as the derivatives of the shape functions, which are orthogonal to the assumed spatial variation in axial creep strains. This implies:

$$E_i = \int_0^\ell \left[\int_{A_2} \left(\mu \dot{u}'_{cr} + (E_e + E_v)u'_{cr} - E_e u'\right) N'_i(x)\right] dx \tag{5.52}$$

Setting the errors to zero produces the following two equations:

$$\frac{\mu A_2}{\ell}\begin{bmatrix} 1 & -1 \\ -1 & 1 \end{bmatrix}\begin{bmatrix} \dot{u}_1^{cr} \\ \dot{u}_2^{cr} \end{bmatrix} + \frac{(E_e+E_v)A_2}{\ell}\begin{bmatrix} 1 & -1 \\ -1 & 1 \end{bmatrix}\begin{bmatrix} u_1^{cr} \\ u_2^{cr} \end{bmatrix} - \frac{E_e A_2}{\ell}\begin{bmatrix} 1 & -1 \\ -1 & 1 \end{bmatrix}\begin{bmatrix} u_1 \\ u_2 \end{bmatrix} = \begin{bmatrix} 0 \\ 0 \end{bmatrix} \tag{5.53}$$

These two sets of equations can be written as a single matrix equation involving nodal variables. To show this, we use the conventional mass and stiffness matrices for axial behavior in the wall:

$$[k_a] = \frac{\overline{EA}}{\ell}\begin{bmatrix} 1 & -1 \\ -1 & 1 \end{bmatrix}; \quad [m_a] = \overline{\rho A}\,\ell\begin{bmatrix} 1/3 & 1/6 \\ 1/6 & 1/3 \end{bmatrix} \tag{5.54}$$

With these definitions, the four equations governing nodal variables (for axial response) are given by:

$$\begin{bmatrix} [k_a]_{2x2} & -\alpha_a [k_a]_{2x2} \\ -\alpha_a [k_a]_{2x2} & \beta_a [k_a]_{2x2} \end{bmatrix}\begin{bmatrix} q_{2x1} \\ q_{2x1}^{cr} \end{bmatrix} + \begin{bmatrix} [0]_{2x2} & [0]_{2x2} \\ [0]_{2x2} & \tilde{\eta}_a [k_a]_{2x2} \end{bmatrix}\begin{bmatrix} \dot{q}_{2x1} \\ \dot{q}_{2x1}^{cr} \end{bmatrix} + \begin{bmatrix} [m_a]_{2x2} & [0]_{2x2} \\ [0]_{2x2} & [0]_{2x2} \end{bmatrix}\begin{bmatrix} \ddot{q}_{2x1} \\ \ddot{q}_{2x1}^{cr} \end{bmatrix} + \begin{bmatrix} F_{2x}^a \\ 0_{2x1} \end{bmatrix} \tag{5.55}$$

where $q_{2x1} = [u_1\, u_2]$ are the nodal (total) displacements, $r_{2x1}^{cr} = [u_1^{cr}\, u_2^{cr}]$ are the nodal creep displacements, and $F_{2x1}^a = [N_1\, N_2]$ are the applied nodal forces. Dots denote derivatives with resect to time. The composite parameters controlling the role of the

viscoelastic phase for axial deformation are:

$$\alpha_a = \frac{E_e A_2}{\overline{EA}}; \quad \beta_a = \frac{(E_e + E_v)A_2}{\overline{EA}}; \quad \tilde{\eta}_a = \frac{\mu A_2}{\overline{EA}} \tag{5.56}$$

Next, consider discretization of the bending equation. The interpolation is given by:

$$w(\xi) = w_1(1 - 3\xi^2 + 2\xi^3) + \ell\theta_1(\xi - 2\xi^2 + \xi^3) + w_2(3\xi^2 - 2\xi^3) + \ell\theta_2(\xi^3 - \xi^2) \tag{5.57}$$

where $w_{1,2}$ are the transverse displacements at the two nodes, and $\theta_{1,2}$ are the nodal rotations. We use identical interpolation for the creep displacements, with analogous nodal variables. The PVW statement for bending produces the following:

$$\frac{\overline{EI}}{\ell^3}\begin{bmatrix} 12 & 6\ell & -12 & 6\ell \\ 6\ell & 4\ell^2 & -6\ell & 2\ell^2 \\ -12 & -6\ell & 12 & -6\ell \\ 6\ell & 2\ell^2 & -6\ell & 4\ell^2 \end{bmatrix}\begin{bmatrix} w_1 \\ \theta_1 \\ w_2 \\ \theta_2 \end{bmatrix} - \frac{E_e I_2}{\ell^3}\begin{bmatrix} 12 & 6\ell & -12 & 6\ell \\ 6\ell & 4\ell^2 & -6\ell & 2\ell^2 \\ -12 & -6\ell & 12 & -6\ell \\ 6\ell & 2\ell^2 & -6\ell & 4\ell^2 \end{bmatrix}\begin{bmatrix} w_1^{cr} \\ \theta_1^{cr} \\ w_2^{cr} \\ \theta_2^{cr} \end{bmatrix} +$$
$$\overline{\rho A}L\begin{bmatrix} 13/35 & 11L/210 & 9/70 & -13L/420 \\ 11L/210 & L^2/105 & 13L/420 & -L^2/140 \\ 9/70 & 13L/420 & 13/35 & -11L/210 \\ -13L/420 & -L^2/140 & -11L/210 & L^2/105 \end{bmatrix}\begin{bmatrix} \ddot{w}_1 \\ \ddot{\theta}_1 \\ \ddot{w}_2 \\ \ddot{\theta}_2 \end{bmatrix} = \begin{bmatrix} V_1 \\ M_1 \\ V_2 \\ M_2 \end{bmatrix} \tag{5.58}$$

Again using the derivatives of the shape functions that are orthogonal to the assumed spatial variation in bending creep strains, the weighted residual statement for the creep evolution equation is:

$$E_i = \int_0^\ell \left[\int_{A_2} \left(\mu\dot{w}''_{cr} + (E_e + E_v)w''_{cr} - E_e w''\right) N_i''(x)\right] dx \tag{5.59}$$

Setting the errors to zero produces the following four equations:

$$
\begin{aligned}
&-\frac{E_e I_2}{\ell^3}\begin{bmatrix} 12 & 6\ell & -12 & 6\ell \\ 6\ell & 4\ell^2 & -6\ell & 2\ell^2 \\ -12 & -6\ell & 12 & -6\ell \\ 6\ell & 2\ell^2 & -6\ell & 4\ell^2 \end{bmatrix}\begin{bmatrix} w_1 \\ \theta_1 \\ w_2 \\ \theta_2 \end{bmatrix} + \\
&\frac{(E_e+E_v)I_2}{\ell^3}\begin{bmatrix} 12 & 6\ell & -12 & 6\ell \\ 6\ell & 4\ell^2 & -6\ell & 2\ell^2 \\ -12 & -6\ell & 12 & -6\ell \\ 6\ell & 2\ell^2 & -6\ell & 4\ell^2 \end{bmatrix}\begin{bmatrix} w_1^{cr} \\ \theta_1^{cr} \\ w_2^{cr} \\ \theta_2^{cr} \end{bmatrix} + \\
&\frac{\mu I_2}{\ell^3}\begin{bmatrix} 12 & 6\ell & -12 & 6\ell \\ 6\ell & 4\ell^2 & -6\ell & 2\ell^2 \\ -12 & -6\ell & 12 & -6\ell \\ 6\ell & 2\ell^2 & -6\ell & 4\ell^2 \end{bmatrix}\begin{bmatrix} \dot{w}_1^{cr} \\ \dot{\theta}_1^{cr} \\ \dot{w}_2^{cr} \\ \dot{\theta}_2^{cr} \end{bmatrix} = \begin{bmatrix} V_1 \\ M_1 \\ V_2 \\ M_2 \end{bmatrix}
\end{aligned}
\tag{5.60}
$$

As before, we can combine the above equations to produce a single matrix equation for the nodal variables. The conventional stiffness and mass matrices associated with

transverse displacements are given by:

$$[k_b] = \frac{\overline{EI}}{\ell^3}\begin{bmatrix} 12 & 6\ell & -12 & 6\ell \\ 6\ell & 4\ell^2 & -6\ell & 2\ell^2 \\ -12 & -6\ell & 12 & -6\ell \\ 6\ell & 2\ell^2 & -6\ell & 4\ell^2 \end{bmatrix} \tag{5.61}$$

$$[m_b] = \overline{\rho A}\,\ell\begin{bmatrix} 13/35 & 11\ell/210 & 9/70 & -13\ell/420 \\ 11L/210 & \ell^2/105 & 13\ell/420 & -\ell^2/140 \\ 9/70 & 13\ell/420 & 13/35 & -11\ell/210 \\ -13\ell/420 & -\ell^2/140 & -11L/210 & \ell^2/105 \end{bmatrix} \tag{5.62}$$

The above equations can be combined into the following single matrix equation:

$$\begin{bmatrix} [k_b]_{4x4} & -\alpha_b\,[k_b]_{4x4} \\ -\alpha_b\,[k_b]_{4x4} & \beta_b\,[k_b]_{4x4} \end{bmatrix}\begin{bmatrix} q_{4x1} \\ q^{cr}_{4x1} \end{bmatrix} + \begin{bmatrix} [0]_{4x4} & [0]_{4x4} \\ [0]_{4x4} & \tilde{\eta}\,[k_b]_{4x4} \end{bmatrix}\begin{bmatrix} \dot{q}_{4x1} \\ \dot{q}^{cr}_{4x1} \end{bmatrix}$$

$$+ \begin{bmatrix} [m_b]_{4x4} & [0]_{4x4} \\ [0]_{4x4} & [0]_{4x4} \end{bmatrix}\begin{bmatrix} \ddot{q}_{4x1} \\ \ddot{q}^{cr}_{4x1} \end{bmatrix} = \begin{bmatrix} F^b_{4x1} \\ 0_{4x1} \end{bmatrix} \tag{5.63}$$

(5.64)

where $q_{4x1} = [w_1\,\theta_1\,w_2\,\theta_2]$ are the nodal transverse (total) displacements and rotations, $q^{cr}_{4x1} = [w^{cr}_1\,\theta^{cr}_1\,w^{cr}_2\,\theta^{cr}_2]$ are the nodal creep displacements and rotations, and $F^b_{4x1} = [V_1\,M_1\,V_2\,M_2]$ are the associated nodal shear forces and moments. The composite parameters for bending are given by:

$$\alpha_b = \frac{E_e I_2}{\overline{EI}}; \quad \beta_b = \frac{(E_e + E_v)I_2}{\overline{EI}}; \quad \tilde{\eta} = \frac{\mu I_2}{\overline{EI}} \tag{5.65}$$

Complete elemental matrices can be constructed from the above equations. Let the

list of nodal variables be re-defined as:

$$[q] = \begin{bmatrix} u_1 & u_2 & u_1^{cr} & u_2^{cr} & w_1 & \theta_1 & w_2 & \theta_2 & w_1^{cr} & \theta_1^{cr} & w_2^{cr} & \theta_2^{cr} \end{bmatrix} \tag{5.66}$$

$$[f] = \begin{bmatrix} N_1 & N_2 & 0 & 0 & V_1 & M_1 & V_2 & M_2 & 0 & 0 & 0 & 0 \end{bmatrix} \tag{5.67}$$

The complete set of equations for the element is written as:

$$[m_e]_{12x12} \{\ddot{q}\}_{12x1} + [c_e]_{12x12} \{\dot{q}\}_{12x1} + [k_e]_{12x12} \{q\}_{12x1} = [f]_{12x1} \tag{5.68}$$

where the total elemental mass, damping and stiffness matrices are given by:

$$[m_e]_{12x12} = \begin{bmatrix} (m_a)_{2x2} & 0_{2x2} & 0_{2x4} & 0_{2x4} \\ 0_{2x2} & 0_{2x2} & 0_{2x4} & 0_{2x4} \\ 0_{4x2} & 0_{4x2} & (m_b)_{4x4} & 0_{4x4} \\ 0_{4x2} & 0_{4x2} & 0_{4x4} & 0_{4x4} \end{bmatrix} \tag{5.69}$$

$$[c_e]_{12x12} = \begin{bmatrix} 0_{2x2} & 0_{2x2} & 0_{2x4} & 0_{2x4} \\ 0_{2x2} & \tilde{\eta}_a(k_a)_{2x2} & 0_{2x4} & 0_{2x4} \\ 0_{4x2} & 0_{4x2} & 0_{4x4} & 0_{4x4} \\ 0_{4x2} & 0_{4x2} & 0_{4x4} & \tilde{\eta}_b(k_b)_{4x4} \end{bmatrix} \tag{5.70}$$

$$[k_e]_{12x12} = \begin{bmatrix} (k_a)_{2x2} & -\alpha_a(k_a)_{2x2} & 0_{2x4} & 0_{2x4} \\ -\alpha_a(k_a)_{2x2} & \beta_a(k_a)_{2x2} & 0_{2x4} & 0_{2x4} \\ 0_{2x2} & 0_{2x2} & (k_b)_{4x4} & -\alpha_b(k_b)_{4x4} \\ 0_{4x2} & 0_{4x2} & -\alpha_b(k_b)_{4x4} & \beta_b(k_b)_{4x4} \end{bmatrix} \tag{5.71}$$

Since each node has six degrees of freedom, and an element consists of two nodes; the elemental matrices are $12x12$. Note that these equations describe the behavior of an

element lying on the local $x-$axis; they must be converted into global coordinates and assembled into systems-level matrices for analysis of multi-element systems.

5.6.2 Translation to global coordinates and global assembly

The elemental matrices defined above can be transformed into a global coordinate system that translates the axial and transverse displacements into global displacements and rotations. The displacement quantities transform as conventional vector components, while the rotation quantities are unchanged. Define $\{Q\} = [U_1, U_2, U_2^{cr} \ldots]$ as the global nodal variables; let $[A]_{12x12}$ be the global-to-local transformation matrix such that $\{q\} = [A]\{Q\}$. The only non-zero terms of $[A]$ are:

$$\begin{array}{cccc} A_{1,1} = \cos\theta & A_{1,5} = -\sin\theta & A_{2,2} = \cos\theta & A_{2,7} = -\sin\theta \\ A_{3,3} = \cos\theta & A_{3,9} = -\sin\theta & A_{4,4} = \cos\theta & A_{4,11} = -\sin\theta \\ A_{5,1} = \sin\theta & A_{5,5} = \cos\theta & A_{6,6} = 1 & A_{7,2} = \sin\theta \\ A_{7,7} = \cos\theta & A_{8,8} = 1 & A_{9,3} = \sin\theta & A_{9,9} = \cos\theta \\ A_{10,10} = 1 & A_{11,4} = \sin\theta & A_{11,11} = \cos\theta & A_{12,12} = 1 \end{array} \tag{5.72}$$

The elemental matrices associated with the global system are then computed as $[M_e] = [A]^T [m_e] [A]$, $[C_e] = [A]^T [c_e] [A]$, and $[K_e] = [A]^T [k_e] [A]$.

Global assembly of system-level mass, damping and stiffness matrices follows the usual procedure. In the code accompanying this text, the global degrees of freedom for node n are defined as:

$$Q_{6n-5} = U_n;\ Q_{6n-4} = W_n;\ Q_{6n-3} = \theta_n;\ Q_{6n-2} = U_n^{cr};\ Q_{6n-1} = W_n^{cr};\ Q_{6n} = \theta_n^{cr} \tag{5.73}$$

That is, each node has six degrees of freedom; the first three are the conventional nodal quantities corresponding to *total* displacements, which are used to impose boundary

conditions. For each node, the second three degrees of freedom are the corresponding creep displacements, which are left to evolve with time.

After global assembly, the final form of the discretized FEA equations is as follows:

$$[M]\{\ddot{Q}\} + [C]\{\dot{Q}\} + [K]\{Q\} = [F] \tag{5.74}$$

Following imposition of boundary conditions on total displacements, these can be directly integrated to obtain the time-history of nodal variables. In the next section, we illustrate the solution for steady-state response to harmonic loading.

5.6.3 Steady-state response of lattices subjected to harmonic loading

The finite element framework described in the previous section can be used to extract the steady-state response of cellular materials when subjected to harmonic loading. In what follows, we assume the finite element equations have been assembled in the global system and prescribed degrees of freedom have been eliminated, resulting in the linear set of equations:

$$[M]\{\ddot{Q}\} + [C]\{\dot{Q}\} + [K]\{Q\} = [F] \tag{5.75}$$

Assume that harmonic nodal forces or displacements are imposed in the form $F_j = F_j^o e^{i\omega_{ex}t}$, where F_j^o is a real number representing the amplitude of the applied force corresponding to the given degree of freedom, and ω_{ex} is the excitation frequency. Let $Q_j = \tilde{Q}_j e^{i\omega_{ex}t}$, where $\tilde{Q}_j$ is a complex number that represents the amplitude and phase-shift of the degree of freedom Q_j.

This is equivalent to writing $Q_j = Q_j^o e^{i(\omega_{ex}t+\delta_j)}$, where Q_j^o is the steady-state amplitude

of the nodal variable and δ_j is the phase-shift associated with that nodal variable. That is, we can solve for a list of complex quantities describing the nodal variables, $\tilde{Q}_j$, and it contains information describing the magnitude of the steady-state response of that degree of freedom, and the phase shift of that variable with respect to the applied forces. To illustrate this, note that:

$$\begin{aligned} Q_j^o e^{i\omega_{ex}t+\delta_j} &= Q_j^o \left(cos[\omega_{ex}t + \delta_j] - i\sin[\omega_{ex}t + \delta_j]\right) \\ &= Q_j^o \left(cos\omega_{ex}t\cos\delta_j - \sin\omega_{ex}t\sin\delta_j\right) - i\left(\sin[\omega_{ex}t]\cos\delta_j] + \cos\omega_{ex}t\sin\delta_j\right) \\ \tilde{Q}_j e^{i\omega_{ex}t} &= \left(Re[\tilde{Q}]\cos\omega_{ex}t - Im[\tilde{Q}]\sin\omega_{ex}t\right) + i\left(Re[\tilde{Q}]\sin\omega_{ex}t + Im[\tilde{Q}]\cos\omega_{ex}t\right) \end{aligned}$$

Equating either the real or imaginary parts of the above representations shows that they are equivalent when:

$$\begin{aligned} Q_j^o\cos\delta_j = Re[\tilde{Q}_j]; \quad Q_j^o\sin\delta_j = Im[\tilde{Q}_j]; \\ \tan\delta_j = \frac{Im[\tilde{Q}_j]}{Re[\tilde{Q}_j]}; \quad Q_j^o = \sqrt{Re[\tilde{Q}_j]^2 + Im[\tilde{Q}_j]^2} \end{aligned} \tag{5.76}$$

Thus, without loss of generality, we can assume a complex form $Q_j = \tilde{Q}_j e^{i\omega t}$ of the solution; the generalized nodal velocities are therefore $\dot{Q}_j = i\omega_{ex}\tilde{Q}_j$ and the generalized nodal accelerations are $\ddot{Q}_j = -\omega_{ex}^2\tilde{Q}_j$. Plugging these expressions into the governing equations, the exponential terms cancel and one obtains the linear set of equations for the complex amplitudes of the nodal variables:

$$-\omega_{ex}^2\left[M\right]\left\{\tilde{Q}\right\} + i\omega_{ex}\left[C\right]\left\{\tilde{Q}\right\} + \left[K\right]\left\{\tilde{Q}\right\} = \left[F_o\right] \tag{5.77}$$

$$\left[-\omega_{ex}^2\left[M\right] + i\omega_{ex}\left[C\right] + \left[K\right]\right]\left\{\tilde{Q}\right\} = \left[F_o\right] \tag{5.78}$$

This linear equation can be solved to find the steady-state respone of nodal degrees of

freedom, $\tilde{Q}$. Clearly, since the coefficient of the damping matrix is complex, the nodal degrees of freedom $\tilde{Q}$ will also be complex, indicating phase shifts in displacements due to damping. Further, the coefficients of the mass and damping matrices are also a function of excitation frequency; hence we can expect different steady-state nodal motions at different frequencies.

In summary, after solving the matrix equation above, the amplitude of each node is found by the magnitude of the complex number $\tilde{Q}_j$ while the argument represents the phase shift of that node. The damped mode shape refers to a plot of the nodal motions at a given instant in time, using the amplitudes of $\tilde{Q}_j$; these shapes naturally depend on the excitation frequency. Animations of vibrations can be created by imposing harmonic time functions with phase shifts defined by the argument of $\tilde{Q}_j$. Since the phase shifts are generally different for each nodal variable, different parts of a structure can move out of phase with each other and the applied loading.

This finite element framework is therefore completely analogous to a quasi-static finite element framework utilizing Bernoulli-Euler beam elements. Indeed, when the excitation frequency is zero, it produces identical quasi-static results. Steady-state displacement or force amplitudes can be applied to any of the nodes; such boundary conditions should be applied to the total nodal variables, not the creep terms.

5.6.4 Finite element verification and convergence

The finite element formulation has been verified by comparing analytical predictions for undamped natural frequencies for simple cases involving a single wall, with identical boundary conditions at both ends. The results are shown in Figure 5.5. The cases labelled "pinned-pinned" correspond to fixing the ends of the wall to have zero displacement, but free rotation. The cases labeled "clamped-clamped" have zero displacements and

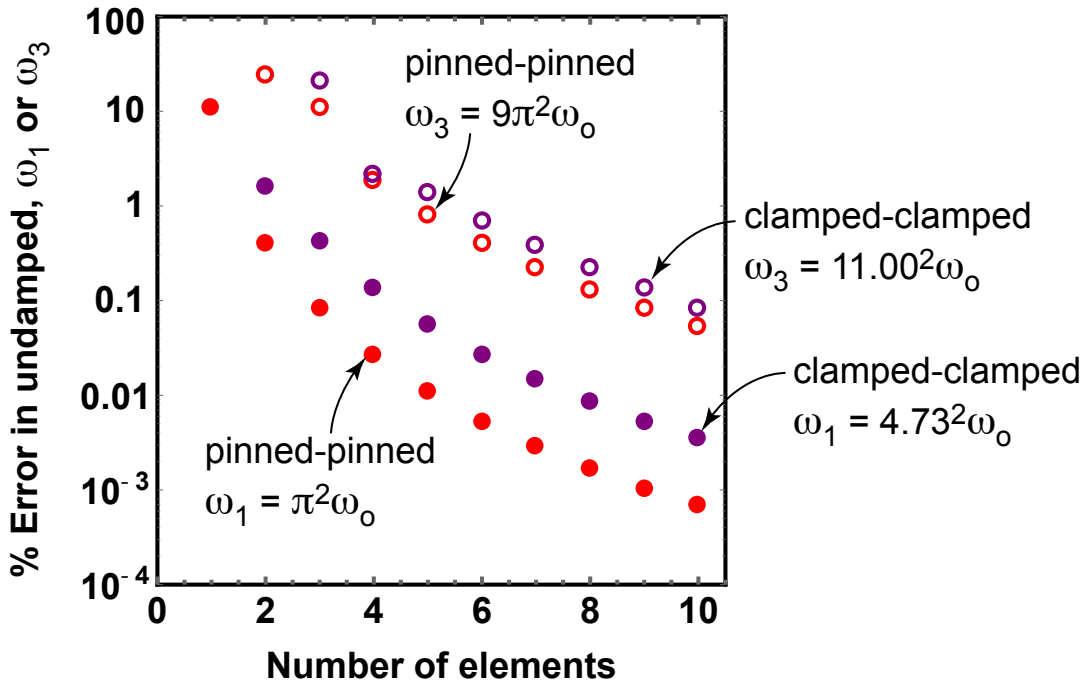

Figure 5.5: Percentage error in first and third natural frequency of pinned and clamped walls versus the number of elements used in the computation. Five elements produce less than ∼1% error.

zero rotation at both ends. Note that for the clamped-clamped condition, more than one element is needed; otherwise, all degrees of freedom in the system are prescribed to zero after imposition of the boundary conditions. For the pinned-pinned wall, the natural frequencies are $\omega_n = (n\pi)^2\omega_o$, with mode shapes defined by $\sin n\pi x/L$. For clamped-clamped walls, the mode shapes are defined by $\omega_n = \lambda_n^2\omega_o$, with λ_n defined by the solution to $\cos\lambda_n \cosh\lambda_n = 1$; the mode shapes are a combination of trigonometric functions and can be found in standard vibration texts.

Figure 5.5 clearly illustrates that the several lowest natural frequencies of a wall are captured to within a couple of percent with five or more elements. As the mode number increases, an increasing number of elements is needed to capture mode shapes described by higher harmonics; this is clearly illustrated in Figure 5.6, which plots the natural

frequencies for the first 25 modes for several different mesh densities. Note that for the discretized system, the maximum mode number that can be predicted is given by the active number of degrees of freedom in the model, i.e. $3n - 2i$, where n is the number of elements and i are the number of degrees of freedom eliminated at the ends. Hence, the cases with just a few elements per strut are incapable of predicting higher modes. As a general rule, the first $2n$ modes are accurately captured when there are n elements per strut.

The accuracy of forced vibration amplitudes in damped systems is more difficult to assess, due to the lack of analytical solutions. However, the formulation and implementation are clearly convergent. Numerical studies indicate that the predictions are independent of mesh density for $2n > m$, where n is the number of nodes and m is the highest mode of interest. Figure 5.2, which illustrates the 1DOF approximation outlined previously, also shows the results from the present finite element framework for pinned-pinned beams with four elements (plot points). Simulations with more elements are indistinguishable from those shown.

The striking agreement between the FEA results and the single degree of freedom model indicates two points: (i) the frequency response from the finite elements converges upon mesh refinement, and (ii) the single degree of freedom model is an excellent approximation to converged numerical results (for pinned-pinned walls). The excellent performance of the analytical single degree of freedom model is a consequence of the fact that the first mode shape was used to describe the spatial variation of displacements. (Recall that the approximation assumes $W(\bar{x}, \tau) = W_o(\tau) \sin \pi\bar{x}$.) Thus, the spatial distribution of displacements is highly accurate over the frequency range shown in Figure 5.2; the approximate model will of course fail to capture any peaks associated with higher modes.

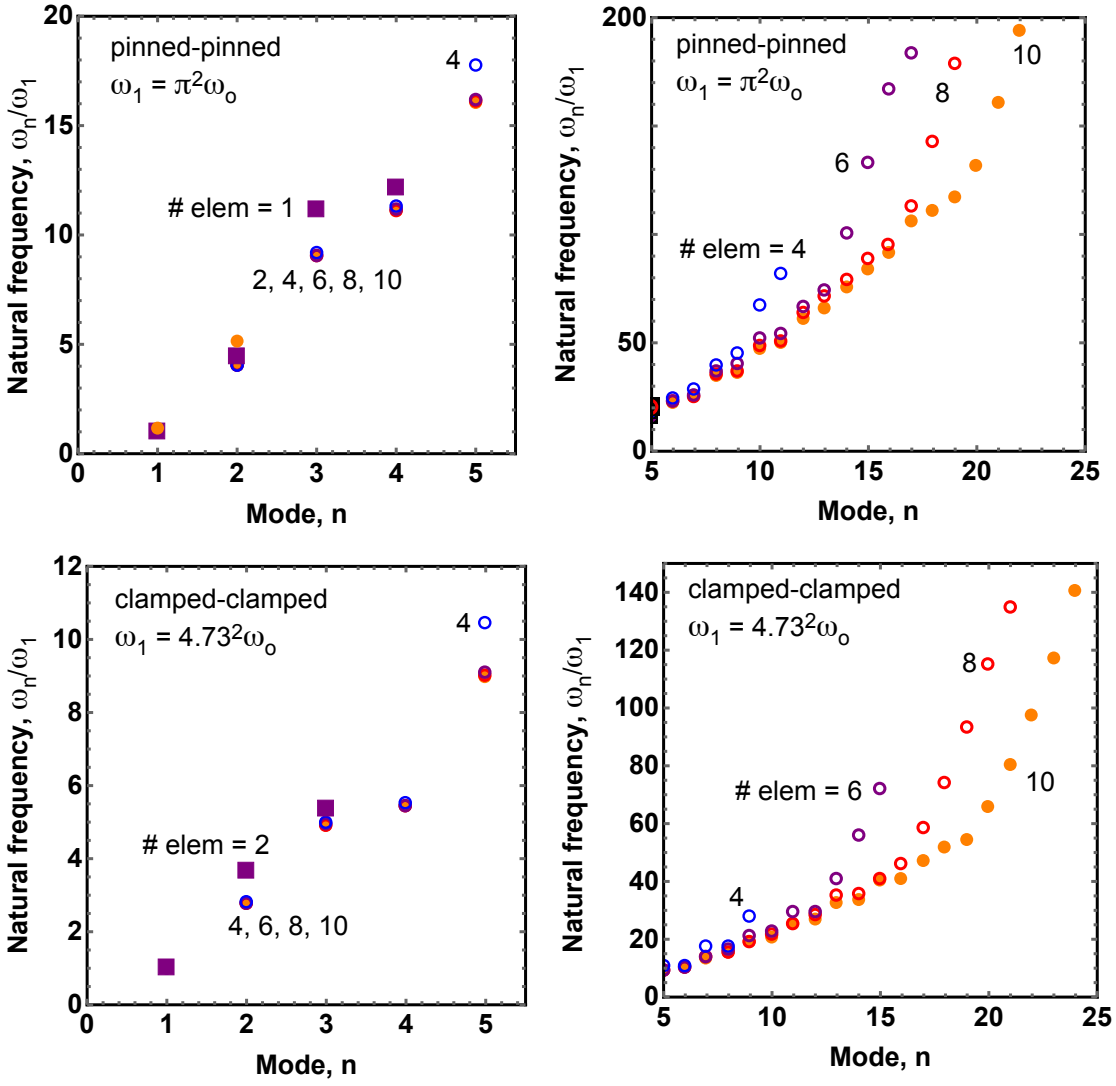

Figure 5.6: Natural frequencies of pinned and clamped walls, for several different mesh densities. Accurate computation of high frequency modes are increasingly expensive, due to the fact high resolution is needed to capture vibration modes with wavelengths much smaller than the wall size.

5.7 Frequency response of honeycombs

Here, we consider prismatic hexagonal honeycombs such as the one shown in Figure 5.1. To elucidate the basic scaling controlling dynamic response, we consider the simple case of uniaxial loading. A uniform distributed pressure (harmonic in time) is applied to wall along the top of the structure, while the bottom is fixed to have zero displacement and rotation. The wall along the top are set to have a bending stiffness that is 10^6 times higher than the remainder of the honeycomb, but zero mass[3]. This effectively constrains the top of the specimen to behave as a rigid, massless platen with uniform displacement and zero rotation of the connecting walls. Of central interest is the frequency response as a function of honeycomb dimensions and material properties, i.e. the output displacement of the top of the structure relative to the quasi-static response for the same pressure magnitude.

For solid walls and in the limit that the structure is much larger than the cell size, the modulus and relative density of a hexagonal honeycomb, denoted by E_H and ρ_H respectively, are given by [6]:

$$\frac{E_H a^3}{E t^3} = \frac{12}{1 + (16.2 + 4.5v)(t/a)^2}; \quad \frac{\rho_H}{\rho} = \frac{t}{a}\left(2 - \frac{t}{a}\right) \tag{5.79}$$

where a is the cell size (measured from one face to the parallel face), t is the wall thickness, E is the elastic modulus of the base material, v is the base Poisson's modulus, and ρ is the base density. This result takes into account shear deformation in the cell walls, while the finite element result does not; the two predictions should be in complete agreement when $16(t/a)^2 << 1$.

Consider a specimen that is infinitely wide and has a vertical height given by $H =$

[3]This was done merely to avoid tracking another parameter; the dynamic response will shift due to the mass of the top platen, and by dropping this term the honeycomb can be thought of as a spring with distributed mass taken into account.

aN_Y. A simple estimate for the first natural frequency of vibration *associated with stretching in the* $Y-$*direction*[4] is:

$$\omega_H = \frac{\pi}{2H}\sqrt{\frac{E_H}{\rho_H}} \approx \frac{\sqrt{6}\pi\, t}{2N_Y\, a^2}\sqrt{\frac{E}{\rho}} \tag{5.80}$$

Recall that the characteristic frequency associated with bending of the walls is given by:

$$\omega_o = \sqrt{\frac{EI}{\rho A a^4}} = \frac{t}{\sqrt{12}a^2}\sqrt{\frac{E}{\rho}} \tag{5.81}$$

Thus, ignoring shear deformation in the walls, the dimensionless natural frequency of a panel of dimension H can be written as:

$$\frac{\omega_H}{\omega_o} \approx \frac{6\pi}{\sqrt{2}N_Y} = \frac{6\pi}{\sqrt{2}}\frac{a}{H} \tag{5.82}$$

In the results that follow (based on the finite element predictions), deviations from this prediction arise from the fact that panels of finite width may or may not be large enough for the effective medium properties E_H and ρ_H to be accurate.

Figure 5.7 illustrates the undamped natural frequencies computed from the finite element framework for various honeycombs with different numbers of cells in each direction. The results are normalized by the scaling frequency given as eqn. 5.81. For each discretized structure, there are $3n$ natural frequencies (i.e. the number of degrees of freedom where n is the number of nodes. The results indicate that the simple effective medium estimate for first natural frequency is highly accurate when there are at least four cells in both directions. Though not shown, the lowest natural frequency of this particular structure is associated with a lateral vibration mode, due to the lack of constraint in this direction. This lateral vibration mode has vertical displacements of the top platens

[4]It will be shown the first fundamental natural frequency is actually associated with lateral movement.

that are virtually identical to the quasi-static result. In what follows, this mode is ignored in favor of the second highest natural frequency, which produces large resonant displacements in the loading direction.

The dynamic response of a honeycomb is shown in Figure 5.8 as a function of excitation frequency, for 'low' frequencies associated with the first six modes. Results are shown for a lightly damped material with a Q-factor of ~ 150; a complete discussion of material selection and associated damping is given in the next section. The frequency response curve depicts the steady-state output displacement amplitude normalized by that obtained from the quasi-static result (blue), and the maximum force transmitted to the base platens normalized by the quasi-static result (orange). The mode shapes associated with several resonant peaks are also shown; these shapes are scaled by an arbitrary factor that produces a clear image of wall deformation.

One can see from the top of Figure 5.8 that the first mode shape is virtually identical to the quasi-static deformation result; in essence, the top platen moves up and down with relatively uniform cell deformation throughout the structure. Note, however, that the resonant peak implies that the first vibration mode experiences an amplitude amplification, or Q factor, of ~ 150; hence the scaling factor for this mode shape in Figure 5.8 is quite small to avoid obfuscation. Note that resonance also dramatically increases the forces transmitted to the base.

Beyond the first natural frequency, the mode shapes illustrate that deformation is highly non-uniform. Note that resonant frequencies exist wherein the top platens essentially remains motionless; the case with $\omega_{ex}/\omega_o = 4.78$ has the same scaling factor as the quasi-static result, $A = 30$, yet the top platens don't move (in comparison to the quasi-static result). In this mode, the region of compressed cells oscillates from the bottom half of the structure (as shown) to the top half of the structure, while the platen remains largely motionless. A possibly helpful interpretation is that the top half of the

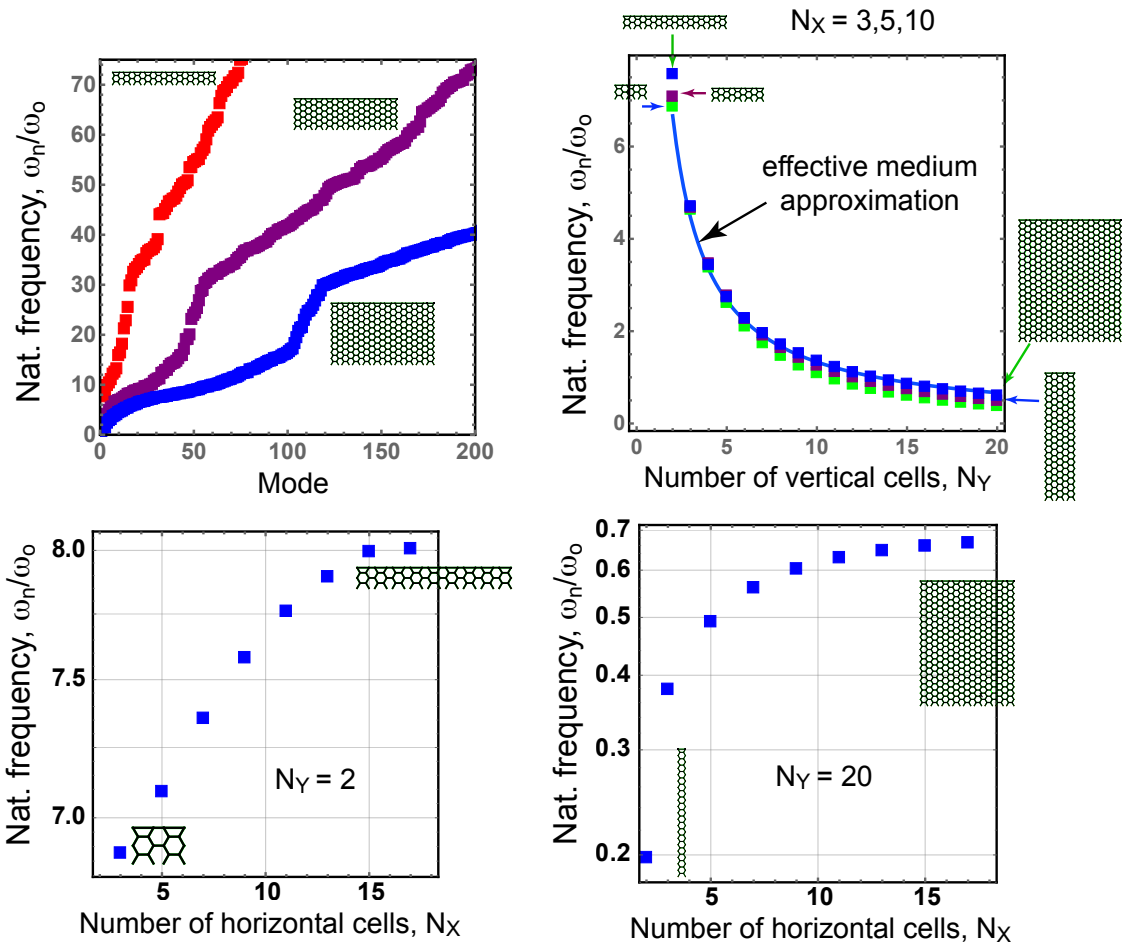

Figure 5.7: Illustration of the undamped natural frequencies of honeycombs with fixed cell size and various aspect ratios defined by the number of cells in the $X-$ and $Y-$directions.

structure moves out of phase with the bottom half, canceling the output displacement of the platens. At slightly higher frequency, the phase shift between the bottom and top halves of the structure is no longer in balance, and the top platen experiences large displacements as the compressed cells travel upwards; stretch of the bottom cells allows for platen movement. This alternating behavior (between platen motion and no movement) continues for the next several modes, with only subtle changes in the mode shape.

At higher frequencies, the vibration modes transition from coordinated movements of the cells to internal vibration of the walls, as shown in Figure 5.9. This transition occurs at a frequency of $\omega_{ex}/\omega_o \sim 35$, which is in reasonable agreement with the natural frequency of pinned beams; it is higher than this approximation due to the fact that intersections impose constraints on the wall rotations. Note from the bottom left of Figure 5.9 that $\omega_{ex}/\omega_o = 25.4$ involves compression/expansion of entire cells in the direction of loading, while $\omega_{ex}/\omega_o = 33.7$ does not; the latter is entirely an internal oscillation mode at the level of individual cells. As one would expect, this transition (which occurs at the kink seen in the natural frequency distribution of Figure 5.7) is relatively insensitive to number of cells in either direction. It should be kept in mind the cell size is fixed as the normalizing length-scale in this study.

Figure 5.9 also illustrates that the higher vibration modes involve dramatically lower amplitudes of the platen motion, as compared to those at lower frequencies. However, the forces transmitted at resonance (shown in orange) are still significantly amplified over the quasi-static result.

5.8 Damping in honeycombs with monolithic struts

The central question at hand is the relationship between material viscoelastic parameters and the damping exhibited by honeycomb structures. In this section, we examine

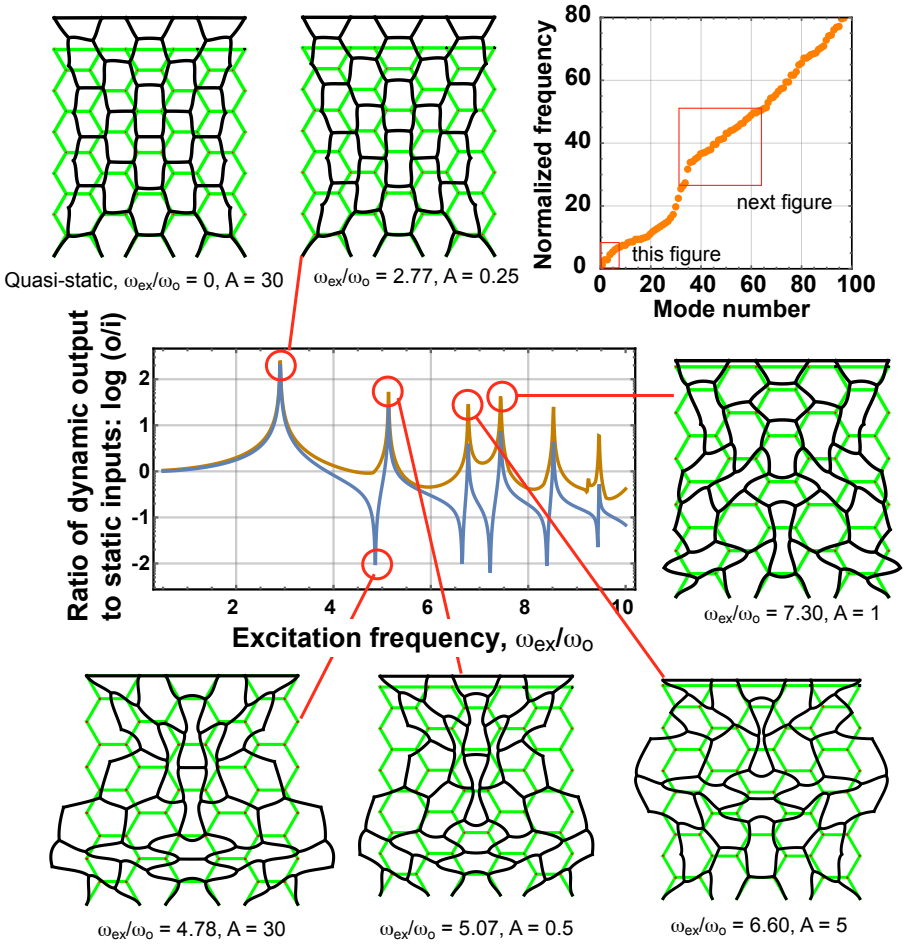

Figure 5.8: The frequency response of a $N_X = N_Y = 5$ honeycomb, with platen steady-state output displacement amplitude normalized by the quasi-static displacement; illustrations of mode shapes for the first six modes show deformation fields associated very different motions of the top platens.

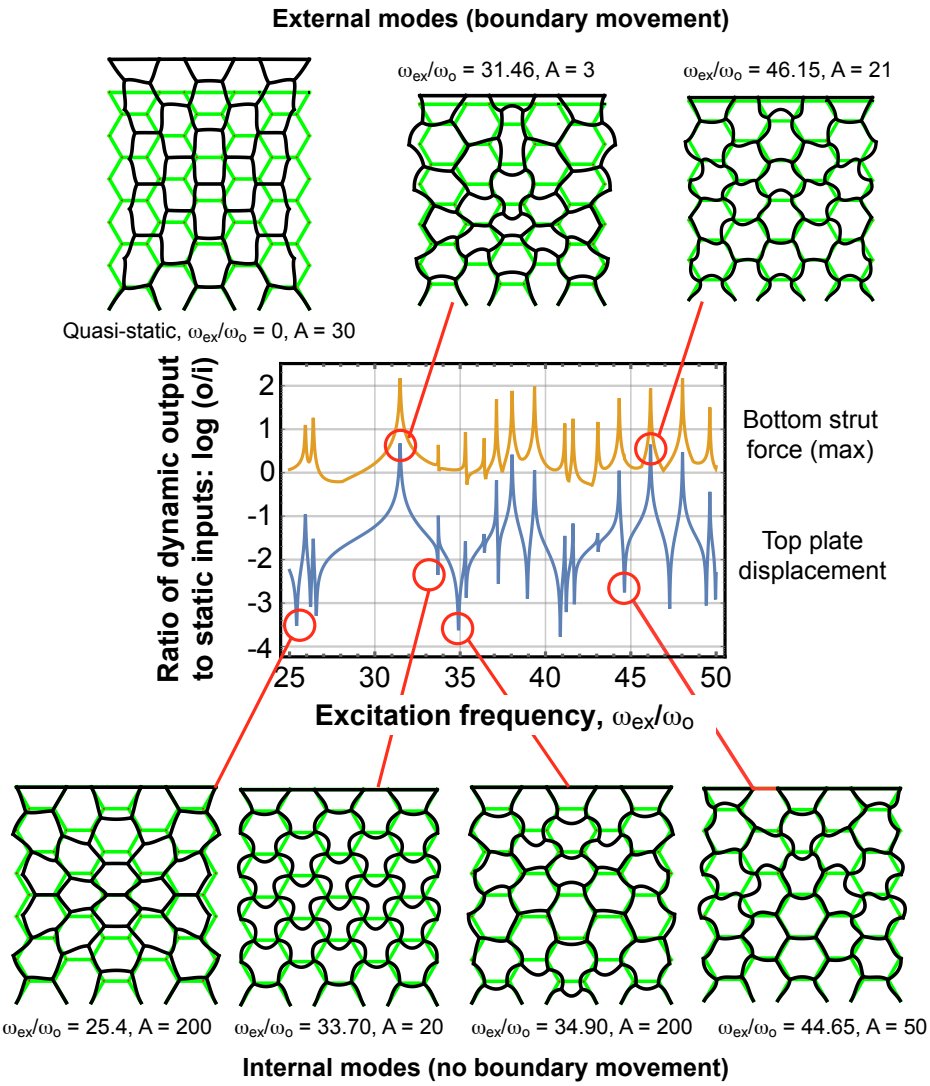

Figure 5.9: The frequency response of a $N_X = N_Y = 5$ honeycomb, with platen steady-state output displacement amplitude normalized by the quasi-static displacement; illustrations of mode shapes for higher order modes show deformation fields associated very different motions of cell walls.

this relationship for honeycombs made from a single material. This establishes a baseline for evaluating the impact of using composite struts, which is outlined in the next section.

Recall that the standard linear model for viscoelasticity is defined in terms of two moduli, E_e and E_v and a viscosity η. Strictly speaking, these parameters could be determined from fits to cyclic loading across a broad range of frequencies, or, from translating temperature data into frequency space. The latter is quite involved and requires more information than than is typically provided with published temperature-dependent moduli. As an alternative, we adopt the following approach for parameter estimation, which assumes tabulated material loss factors are relatively constant across the relevant frequency range.

Viscoelasticity parameters are estimated by assuming that tabulated loss factors, such as those shown in the Ashby map in Figure 5.10, are associated with frequencies corresponding to peak material damping. Using these loss factors and the quasi-static elastic moduli, $E_2 = E_e E_v/(E_e + Ev)$, one can solve for associated values of E_e and E_v. The viscosity η is then chosen to match the peak damping frequency of the material to that of the structure. Obviously, this is an optimal condition that produces peak damping in the structure; it should also be recognized that depending on the natural frequency of the structures, materials that exhibit this peak frequency may be difficult to identify. Nevertheless, this procedure provides an upper bound for the increase in damping possible with composite struts. For metals, the loss factors vary weakly with frequency over a broad range, and the outlined procedure ensures that the chosen loss factor at the frequency of interest is representative of this value. For polymers, the premise is that suitable chemistries can be identified that have peak frequencies near that of the structure, with loss factors in agreement with tabulated data.

For honeycombs with monolithic struts, the elastic modulus $E = E_e E_v/(E_e + E_v)$ plays no role in the frequency-response, provided one compares output dynamic dis-

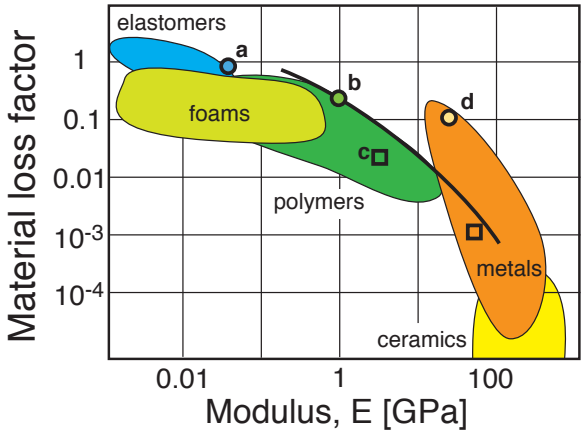

Figure 5.10: An adapted Ashby map illustrating the relationship between loss coefficients and elastic moduli for various classes of materials. The squares indicate the base material used as face sheets, while the circles denote materials chosen as candidate fillers.

placements to the quasi-static response. Figure 5.11 illustrates the relationship between structural loss factors and the material loss factors for several uniform honeycombs. The structural loss factor was computed by finding the peak response at resonance for the mode that exhibits the largest displacement in the loading direction. That is, the results in Figure 5.11 were determined by finding the first peak in the response shown in Figure 5.8. Figure 5.11 clearly demonstrates that structural loss factors are 23% higher than material loss factors, in precisely the same manner as a uniform rod under axial loading. Recall from Section 5, that this slightly higher damping level can be attributed to inertial effects arising from the consideration of a material with a distributed mass. The same holds true for uniform honeycombs subject to their first vibration mode, where cells deform cooperatively and effective medium descriptions of the honeycomb are accurate.

The question naturally arises as to whether cell geometry can be manipulated to increase structural damping while maintaining static stiffness. To address this question, novel honeycombs with non-uniform cell shapes were generated using a simple mapping

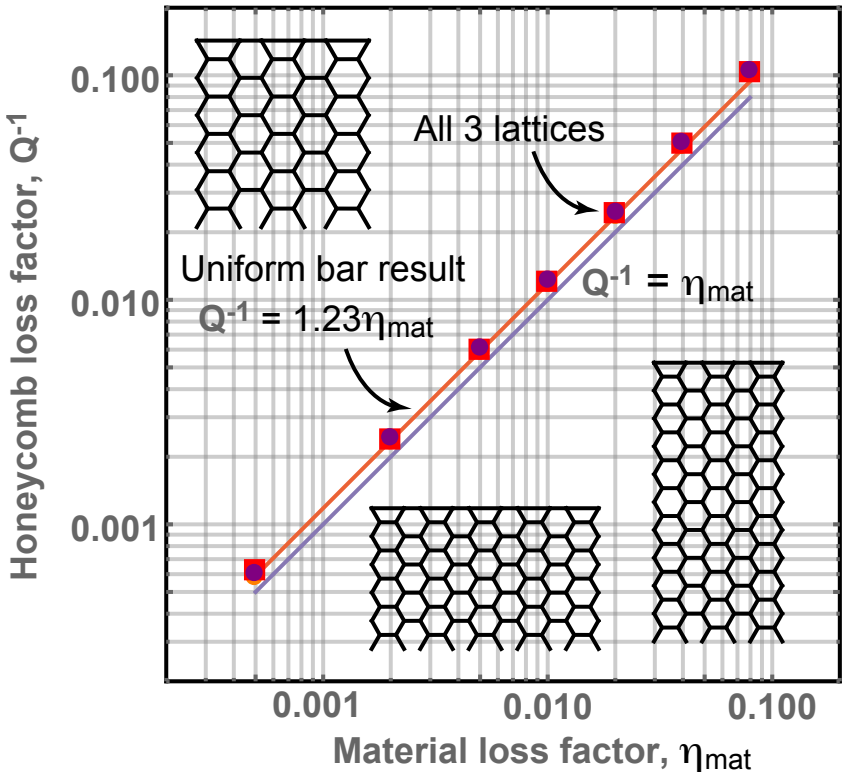

Figure 5.11: Loss factors at resonance for uniform honeycombs with monolithic struts, when the viscosity is tuned such that $\xi = \eta\omega_n/(E_e + E_v) = 1$. Tuned honeycombs give the same response as a uniaxial material with the same effective modulus and density.

algorithm[5], as shown in Figure 5.12. The mapping was based on moving strut intersections according to a simple harmonic function in two directions. The function ensures that the dimensions of the structure are a multiple of the mapping wavelength, such that the outer boundaries are unchanged. As shown in Figure 5.12, the effect of the mapping is to compress or elongate cells near the centerlines of the base structure.

Frequency response curves were generated using the FEA framework described earlier; several examples are shown in Figure 5.12. Note that changes in cell distribution shift the natural frequency of the structure, presumably as a result of changes to the static stiffness. The first resonant peak was used to estimate the structural loss factor (i.e. Q^{-1}). The structural loss factors are shown along with static stiffness values in Figure 5.12, normalized by the results of the uniform honeycomb. One obtains the same relative performance between the perturbed and uniform honeycombs regardless of the material damping used for both cases. Hence, the factor of two improvement in damping exhibited in Figure 5.12 is purely a function of geometry.

The results indicate that honeycombs with large, centrally placed cells increase structural damping, presumably because they disrupt the standing half-wave present in a uniform honeycomb. However, the effect depends strongly on the nature of compressed cells on either side of the open space. Compare for example the red honeycomb on the left of Figure 5.12 with the green honeycomb shown on the right; the differences in cell topology are slight, and yet the overall damping level is quite different. Future work will address these differences through systematic exploration of the design space.

[5]The mapping algorithm was developed by Prof. B. Compton at the University of Tennessee, and will described in forthcoming publications.

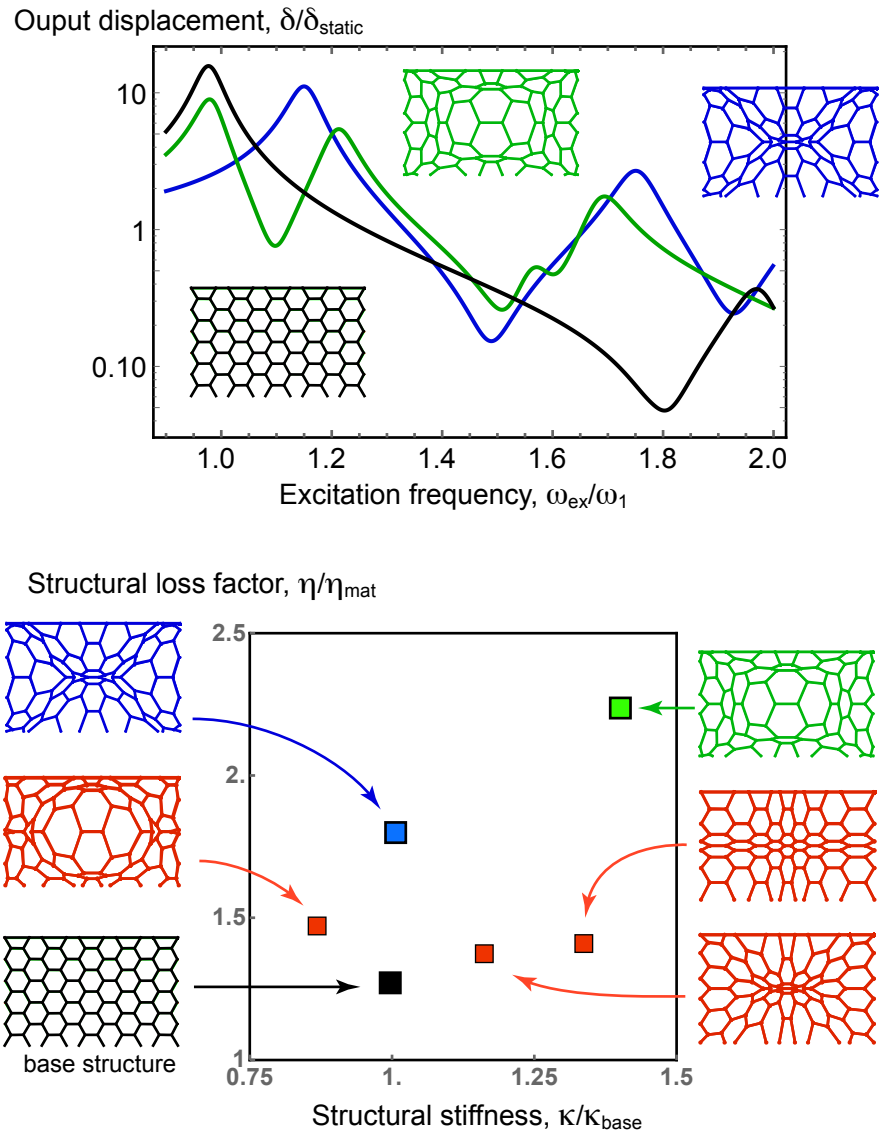

Figure 5.12: Loss factors at resonance for perturbed honeycombs with monolithic struts, when the viscosity is tuned such that $\xi = \eta\omega_n/(E_e + E_v) = 1$.

5.9 Damping in honeycombs with composite struts

In this section, we examine the impact of using composite struts, to address whether or not including high damping phases will be effective improve structural damping. The labelled points in Figure 5.10 indicate representative materials chosen for the present study.

The two "baseline" materials are indicated by squares: a glassy polymer with $E_2 = 4\ GPa$ and $\eta_{mat} = 0.02$, and aluminum with $E_2 = 70\ GPa$ and $\eta_{mat} = 0.001$. Point **(a)** is representative of silicone elastomers, while point **(b)** is an arbitrary point at the edge of the polymer region that maximizes stiffness and loss factors. Point **(c)** is a typical glassy polymer (such as PMMA or PC) and considered as both a filler material and an outer shell. Point **(d)** is an arbitrary point at the edge of the metal region that maximizes stiffness and loss factors.

For the purposes of illustration, the present study fixes the cell size to be $a = 1\ cm$ and the wall thickness to be $d = 1.4\ mm$. Composite struts have 1 mm cores with 0.2 mm face sheets on either side. A specimen with $N_X = N_Y = 5$ is analyzed (i.e. structures identical to those shown in Figures 5.8 and 5.9). For comparison with composite struts, two baseline cases with monolithic struts are identified: solid walls and "shell" walls created by using the face sheets with an empty core. Properties of these baseline cases are listed in Table 5.1. The table includes the properties used in the analysis, as well as the structural damping found by analyzing frequency response curves for the monolithic struts. As seen from Table 5.1, removing material from the solid core (to convert to shell walls) leads to higher natural frequencies due to the loss of mass, which outweighs the associated loss of stiffness. The baseline structural loss factors are comparable to that of the material loss factor, as discussed in Section 5.8.

The composite struts are created by combining the baseline materials described in

Cell walls	$E,\ \rho$	η_{mat}	ω_1	kL^4/EI	Q	ξ_{eff}
metal, solid	70 GPa, 2.7 g/cm^3	0.001	7.6 kHz	27.5	450	0.00123
metal, empty core	70 GPa, 2.7 g/cm^3	0.001	11.1 kHz	14.9	450	0.00123
polymer, solid	4 GPa, 1.2 g/cm^3	0.01	1.6 kHz	1.6	50	0.0123
polymer, empty core	4 GPa, 1.2 g/cm^3	0.01	2.7 kHz	0.9	46	0.0123

Table 5.1: Baselines strut properties used for the comparison with composite struts; the cell size is $a = 1\ cm$, the wall thickness is 1.4 mm, and the number of cells is $N_X = N_Y = 5$. Thus, the specimens measure about 2" square. Viscoelastic moduli are computed assuming peak damping; the viscosity is chosen to match the characteristic frequencies of the materials and the structures.

Filler material	$E,\ \rho$	η_{mat}	E_e	E_v
a, elastomer	40 MPa, 1.2 g/cm^3	0.89	200 MPa	50 MPa
b, polymer with high damping	1 GPa, 1.2 g/cm^3	0.2	1.5 GPa	3 GPa
c, polymer with low damping	4 GPa, 1.2 g/cm^3	0.02	4.2 GPa	100 GPa
d, metal with high damping	20 MPa, 2.7 g/cm^3	0.1	24.4 GPa	111 GPa

Table 5.2: Filler materials considered in the composite comparison; the core size is 1 mm and the face sheet thickness is 0.2 mm. Viscoelastic moduli are computed assuming peak damping; the viscosity is chosen to match the characteristic frequencies of the materials and the structures.

Table 5.1 with the filler materials listed in Table 5.2. The filler materials in the study are shown as filled circles in the Ashby diagram in Figure 5.10. Again, viscoelastic moduli of the filler are computed assuming peak damping; the viscosity parameter is chosen to match the characteristic frequencies of the materials and the structures. For the composite struts, the filler material is treated as the viscoelastic face, while the face sheets are treated as purely elastic. For this reason, the estimated damping of the composite honeycombs is an underestimate; for lightly damped systems, the effective damping constant for the face sheets can be superposed with the effective damping constant for the composite (with elastic face sheets).

The frequency responses of two systems are shown in Figure 5.13: a metal filled with elastomer, and a polymer filled with elastomer. Clearly, more significant damping

is achieved when the modulus of the filler material is closer to the face sheet modulus. Figure 5.13 illustrates that the storage and loss moduli vary only slightly over the same frequency range. The Q factor is defined as the maximum output displacement (relative to the quasi-static response) across the entire range of frequencies. Clearly, optimal structural damping is achieved when $(E_e + E_v)/\eta = \omega_n$, as suggested by the approximate model presented earlier in this chapter.

Figure 5.14 provides an Ashby-type diagram that maps the structural loss factors with the structural stiffness, for various composite walls. The data refers to the response at the first natural frequency, with the loss factor computed as Q^{-1}. Table 5.3 summarizes the numerical values of the inputs and outputs of the analysis. The stiffness used in the bottom of Figure 5.14 is defined as the ratio of the normalized pressure magnitude to the static output displacement, $Lp_o/EI\delta_{st}$.

The results clearly indicate that significant damping improvements with composite struts are only possible when the modulus of the filler material is within a factor of 100 of the face sheet material. Further, the shifts in stiffness are relatively small due to the inefficient use of material near the neutral axis of the beam. When the modulus of the filler and shell are within a factor of one hundred, the shifts in effective damping coefficient can be a factor of 5-10. For these bending-dominated structures, the effective damping of the composite does not follow rule of mixtures, but rather scales with the ratio $\frac{E_2 I}{EI}$; this diminishes the potential impact of the viscoelastic core because only the core material near the face sheets contributes to damping.

These effects are more clearly illustrated in Figure 5.15, which fixes the modulus ratio between filler and shell, or the loss-factor of the filler. When the moduli of the filler is low, significant gains are only possible using fillers with very high material loss factors. On the other hand, for structures with high loss factors $\eta_{mat} \sim 1$, dramatic improvements are possible if the filler has a modulus within 5% of the shell. The results in Figure

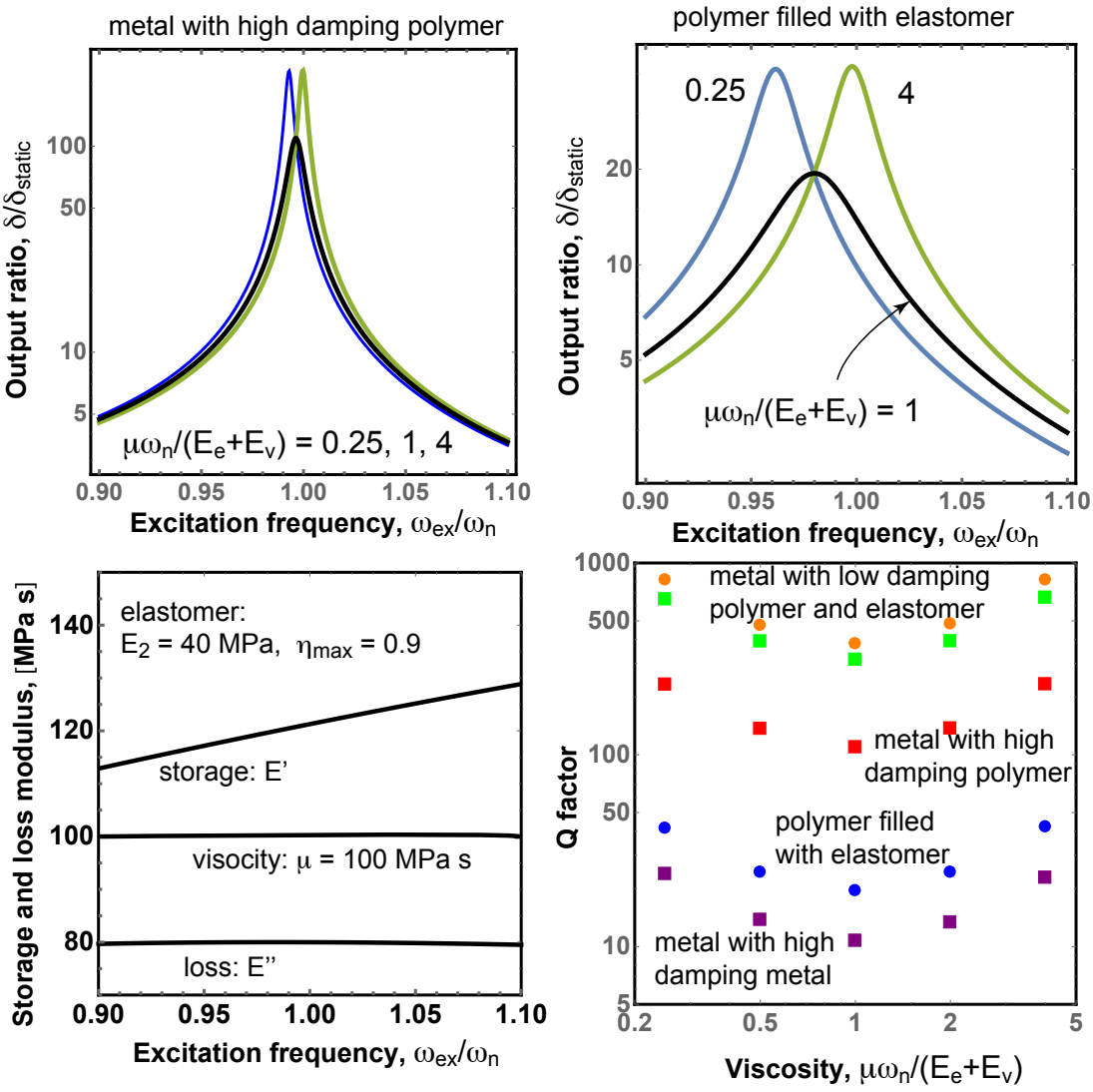

Figure 5.13: Frequency response curves for two systems with properties listed in Tables 5.1 and 5.2, for several levels of viscosity. Optimal damping occurs when the frequency associated with peak loss moduli is tuned to the natural frequency of the structure. Note that the loss moduli does not vary by more than 10% over the frequency range shown.

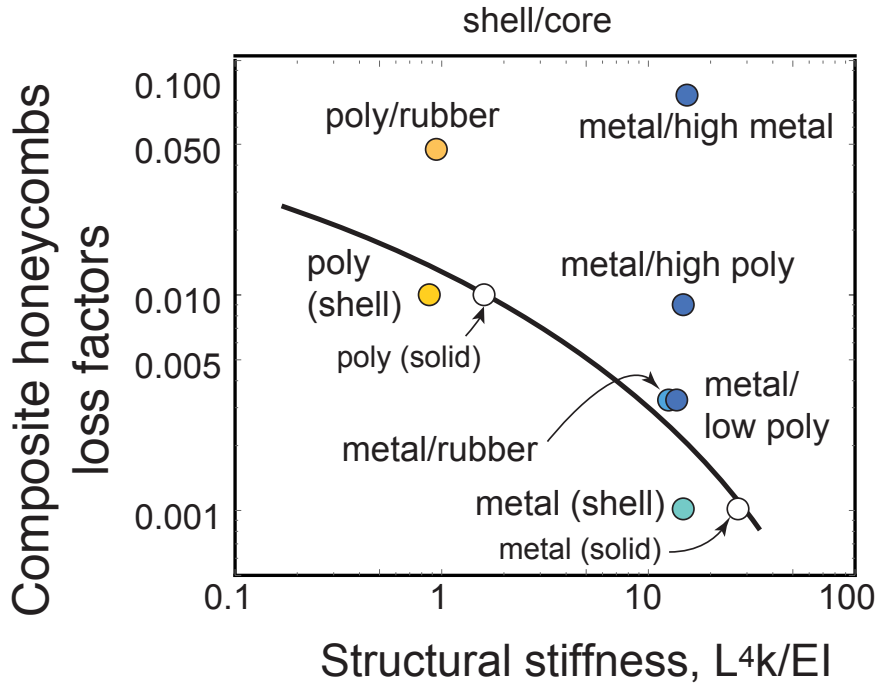

Figure 5.14: An Ashby-type map illustrating structural loss factors versus static stiffness for honeycombs made with composite walls.

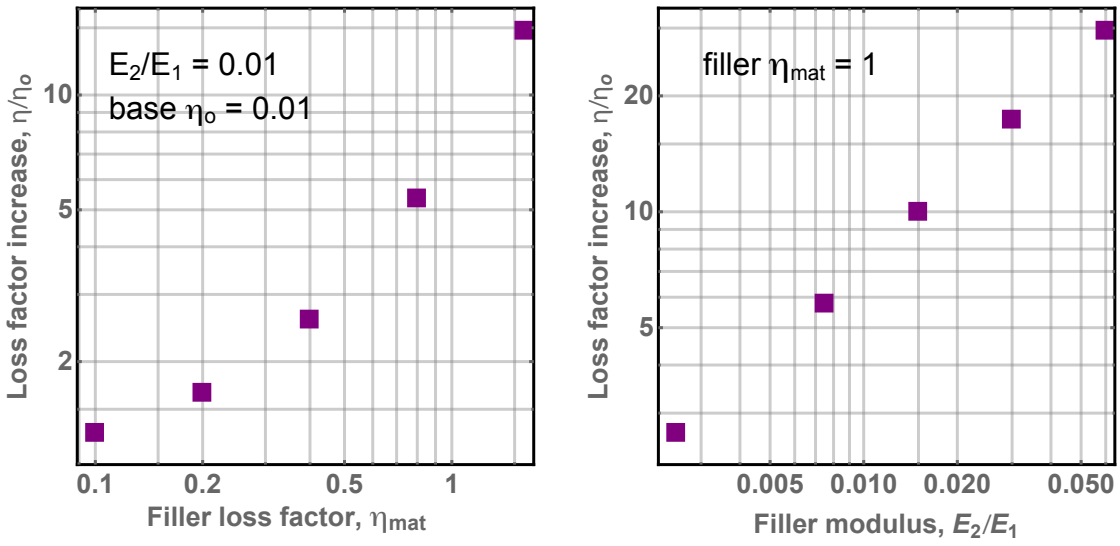

Figure 5.15: An illustration of the effect of filler loss factors and filler modulus on the structural loss factor, for honeycombs made with composite walls.

5.15 clearly indicate the importance of using high modulus fillers. With sufficiently high modulus fillers, damping can be improved by a factor of 10 relative to the walls, while stiffness can be improved by a factor of 100 relative to just the filler.

5.10 Conclusions

This chapter has made several important contributions to the understanding of damping in cellular structures; first and foremost, it provides a clear, efficient framework to make quantitative connections between viscoelastic materials parameters and structural damping. While the focus of this chapter was on steady-state response near resonance, the framework can be applied more generally to consider impacts and other transient phenomena. Approximate solutions for forced dynamic response in bending and stretching provide elegant scaling relationships that identify effective property combinations; these invariably involve matching the characteristic frequency of the material to that of the

Case	Face sheets: filler	α_a, β_a	α_b, β_b	η_a, η_b	Q	η_H
1	metal: solid	1, 500	1, 500	182, 182	450	0.001
2	metal: shell	1, 500	1, 500	200, 200	450	0.001
3	metal: **a**, elastomer	0.014, 0.018	0.004, 0.005	0.007, 0.002	156	0.003
4	metal: **b**, high damp. poly	0.097, 0.293	0.029, 0.087	0.117, 0.035, 0.03	54	0.009
5	metal: **c**, low damp. poly	0.229, 5.85	0.076, 1.93	2.26, 0.74	191	0.0026
6	metal: **d**, high damp. metal	0.64, 3.51	0.32, 1.79	1.3, 0.66	11.5	0.044
7	polymer: solid	1, 50	1, 50	18.5, 18.5	43	0.011
8	polymer: shell	1, 50	1, 50	20, 20	43	0.011
9	polymer: **a**, elastomer	0.2,0.25	0.064, 0.080	0.1, 0.032	9.9	0.051

Table 5.3: Property combinations used in the study of honeycombs with composite struts; the loss factors for the composite structures are compared with their monolithic counter parts in Figure 5.14.

structure. With regards to structural resonance of honeycombs, several key observations should provide insightful for future development efforts:

- Well-established descriptions of honeycombs based on effective properties yield accurate, closed-form estimates for the lowest structural natural frequencies, provided there are more than four cells in both directions. Higher order frequencies that involve deformation gradients acting over the scale of individual cells (e.g strut vibrations) require numerical techniques; approximately three elements per vibration mode at the scale of individual cell walls yields accurate results for the first dozen or so natural frequencies.

- Uniform honeycombs with monolithic walls subjected to nearly one-dimensional deformation exhibit structural loss factors that are nearly identical to material loss factors. Structural loss factors can be a factor of two higher than material loss factors for honeycombs with non-uniform cell shapes, due to disruption of standing waves generated during uniaxial vibration. This gain in loss factor can be achieved without sacrificing structural stiffness, suggesting a path towards stiff, high damping structures. Future work should focus on optimization to determine

if larger gains are possible; the framework presented here is highly efficient and should be useful for this purpose.

- Composite walls in honeycombs can offer significant improvements in structural loss factors (relative to their monolithic counterparts); for sufficiently high filler modulus (with a factor of 100), damping can be improved by a favor of 5-10 relative to the wall material, with stiffness values 100 times greater than just the filler material itself.

Chapter 6

Large deformation element

6.1 Introduction

There are many examples of highly porous materials whose microstructure consists of cells formed by connecting networks of slender members, whose thickness is much smaller than the pore size. These include the internal structure of plants [71–74], synthetic and natural foams [6, 75, 76], microtubule networks in biological cells [77–81], and metamaterials designed to exploit non-linear behaviors [8, 14–27]. In all the these structures, the large aspect ratio of the members implies that stretching, bending and large rotations are possible and in many instances, central to the macroscopic functionality. In many instances, large strains are also present, though it is worth emphasizing that in many instances the strains remain small even in when these three deformation modes are present.

Modeling the response of long, slender structures (typically called rods, beams or fibers) have been pursued extensively for decades [28, 82–84], and it is fair to say that the behavior is well-understood and methods are fairly well developed (e.g. [28, 30, 54–56]). That said, simulations remain quite challenging due to the highly non-linear governing

equations involved, which often lead to complex behaviors associated with bifurcations, i.e. buckling and 'snap-through'; the latter refers to a fiber moving unstably from one configuration to a dramatically different configuration, often accompanied by a negative stiffness matrix that causes serious headaches with gradient-based solution methods.

By far, the most common type of solution approach is to cast governing equations based on conservation of momentum in an incremental framework [55, 56]. Such approaches effectively track the solution as deformation increases by solving linear equations representing an expansion from a known state. Certainly these methods have proven successful in the context of predicting the response of simple structures comprising a limited number of slender members; however, serious convergence difficulties often arise for even modestly more complex fiber arrangements. Even specialized solution techniques such as the RIKS method frequently fail, either by failing to find *any* solution or by simply missing a relevant bifurcation. Explicit dynamic methods are more stable, but can require exceedingly small time steps to capture rapid events associated with transitions from one stable configurations to another.

For elastic materials (even highly non-linear ones), one can naturally cast the problem in terms of energy minimization. The challenge of discovering bifurcations is then recast as finding the relevant energy minima. Often, the principle minimum of interest is the global minimum, as presumably, physical systems will find a pathway to this configuration. (This is not always the case: the energy barrier between local minima and the global minimum may be insurmountable, indicating that the global minimum is unreachable in practice.) For finding global minima, many robust search algorithms exist, notably direct search methods that essentially probe the space by evaluating a large number of possible configurations. For obvious reasons, conventional wisdom is that such methods are inherently slow: however, they are amenable to high degrees of parallelization, as such methods rely on function evaluations rather than solving a system

of linear equations based on incremental stiffness matrices.

For large systems, the amenity of parallelization can carry the day; ultimately, the lack of sophistication in the solution algorithm is overcome by the brute force of an extreme number of simultaneous function evaluations. Still further, the robustness of direct search methods implies that failed searches are rare, in contrast to gradient-based methods that often involve poorly conditioned Jacobians.

This is demonstrated in the present work using a Monte Carlo minimization technique. In this approach, each degree of freedom in the model is perturbed and the resulting change in energy is used to either accept or reject the perturbation. The key advantage of this approach is that the perturbations can be done in parallel, implying that one can simultaneously evaluate the impact of changing a large number of degrees of freedom in the energy space. This has recently been demonstrated for large arrays of cohesively bonded bricks [85–87], whose interactions include the possibility of bond rupture (i.e. softening behavior). This inherently non-linear behavior (which can include negative stiffness matrices) can be solved for cases with $10^5 - 10^6$ degrees of freedom in a matter of minutes. Relying only on the evaluation of the global system energy as a function of the unknowns, the complexity of implementation is essentially independent of the degree of non-linearity (be it kinematic or material) and is only restricted to conservative systems. In the context of fiber networks modeled with finite elements, this implies that one merely writes the energy of the system in terms of nodal variables, moving immediately to the solution algorithm without the complexity of deriving highly non-linear governing equations (or their linearized incremental form).

In order to use direct search algorithms and account for large rotations (including both those arising from rigid body rotations and large bending deformations), one must cast the problem in terms of the deformed state. We do so here using an apparently novel element based on Bezier curves, which use global nodal positions in the deformed

state, the global rotation of the element ends, and the stretch ratios at the element ends. Because stretch is a nodal variable, continuity in deformed tangents, curvature and stretch between elements is ensured, such that one does not have to enforce additional constraints relating to prevent elements from "kinking". This element formulation makes energy computations extremely straightforward, and hence is ideally suited to direct search minimization to find solutions. The remainder of this paper describes this element, the associated energy computations, and the performance of Monte Carlo minimization for several test cases.

6.2 Element formulation

Here, we define an element that is initially straight in the undeformed state, and can take on large rotations and curvatures in the deformed state. Here, $X_i^{A,B}$ are the coordinates of the endpoints in the original state, $x^{A,B}$ are the coordinates in the deformed state, and $\theta^{A,B}$ are the global rotations in the deformed state, measured counter-clockwise with respect to the X_1-axis. The deformed state is defined by a cubic Bezier curve, given generally by:

$$x_i(t) = (1-t)^3 x_i^A + 3t(1-t)^2 x_i^a + 3t^2(1-t)x_i^b + t^3 x_i^B \tag{6.1}$$

where $x_i^{A,B}$ are the coordinates of the end-points, and $x_i^{a,b}$ are the coordinates of control points; t is the parametric variable defined on the interval $0 \leq t \leq 1$. As shown in Figure 6.1, the curve at A is tangent to the line extending from the end point A to the control point a, and similarly so for the other end-point. The distance from the end-points to their respective control points controls the size of the loop, while the direction specifies the 'side' which the loop falls, relative to the straight line connect the end-points. Thus,

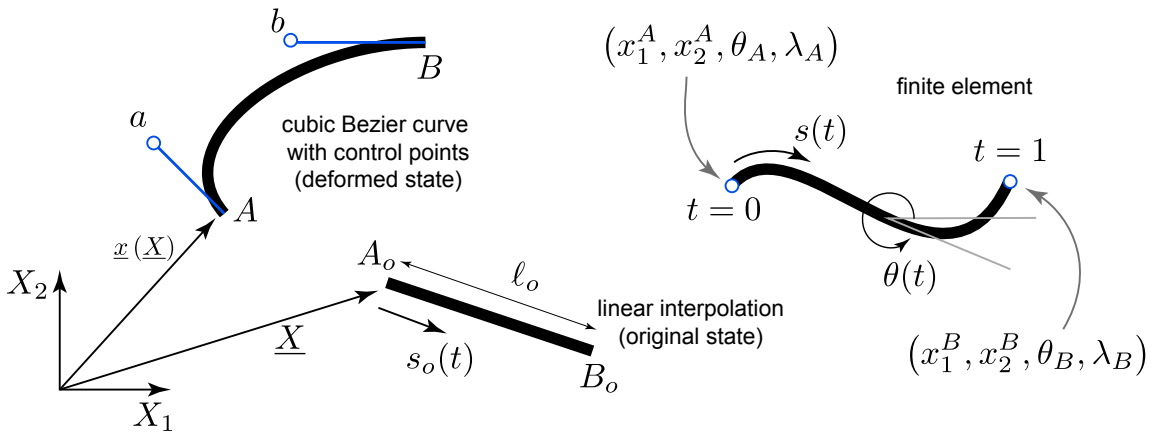

Figure 6.1: Schematic illustrations of Bezier curve illustrating the control points((left) and the parameters used to describe the finite element based on Bezier interpolation (right).

an interesting feature of Bezier curves is that they can trace non-convex shapes, including loops that cross. In what follows, we replace the control points with the stretch ratios at the ends, $\lambda^{A,B}$, such that the interpolation involves four nodal variables at each end, i.e. $\left(x_1^A, x_2^A, \theta_A, \lambda_A\right)$ and $\left(x_1^B, x_2^B, \theta_B, \lambda_B\right)$. Hence, the element has eight degrees of freedom, as suggested by the pure Bezier curve. However, unlike the pure Bezier curve, the degrees of freedom have explicit meaning in the context of fiber deformation, unlike the positions of the control points.

Let $s(t)$ be the distance along the curve in the deformed state; in this case, the tangent vector to the curve in the deformed state is definedy by:

$$\frac{dx_1}{ds} = \frac{x_1'(t)}{s'(t)} = \cos\theta(t); \quad \frac{dx_2}{ds} = \frac{x_2'(t)}{s'(t)} = \sin\theta(t) \tag{6.2}$$

where primes indicate the total derivative with respect to t; the derivative of the path length with respect to the parameter t is given by:

$$s'(t) = \sqrt{x_i'(t)x_i'(t)} \tag{6.3}$$

with summations implied by index notation, and $x_i'(t)$ computed from the Bezier curve. To develop a finite element whose nodal degrees of freedom include the end point positions and tangent in the deformed state (such that one can prescribe forces and moments), we replace the control points in the pure Bezier curve, eqn. 6.1 with:

$$\begin{aligned} x_1^a &= x_1^A + \frac{\ell_o}{3}\lambda_A \cos\theta_A; \quad x_2^a = x_2^A + \frac{\ell_o \lambda_A}{3}\sin\theta_A \\ x_1^b &= x_1^B - \frac{\ell_o \lambda_B}{3}\cos\theta_B; \quad x_2^b = x_2^B - \frac{\ell_o \lambda_B}{3}\sin\theta_B \end{aligned} \tag{6.4}$$

where $\lambda_{A,B}$ represent the stretch ratio of the beam at the end-points, and ℓ_o is the length of the undeformed (straight element) element; the above can be obtained from eqns. (6.1 -6.3) with $t = 0$ for point A and $t = 1$ for point B. Thus, the parametric definition of the Bezier curve to be utilized in the remainder of the paper is:

$$x_1(t) = N_1(t)x_1^A + N_2(t)\ell_o\lambda_A\cos\theta_A + N_3(t)x_1^B + N_4(t)\ell_o\lambda_B\cos\theta_B \tag{6.5}$$

$$x_2(t) = N_1(t)x_2^A + N_2(t)\ell_o\lambda_A\sin\theta_A + N_3(t)x_2^B + N_4(t)\ell_o\lambda_B\sin\theta_B \tag{6.6}$$

where

$$N_1(t) = 1 - 3t^2 + 2t^3; \quad N_2(t) = t(t-1)^2; \quad N_3(t) = 3t^2 - 2t^3; \quad N_4(t) = t^2(t-1) \tag{6.7}$$

For the finite element, we wish to compute the stretch in the beam, which for small strains (but arbitrary displacements and rotations) is given by:

$$\lambda(t) = \frac{ds}{ds_o} - z\frac{d\theta}{ds_o} \tag{6.8}$$

where $s_o(t) = f(X_i(t))$ is the length along undeformed beam, and z is the distance from the neutral axis of the beam. For simplicity, we present results for an initially straight ele-

ment with linear interpolation for the undeformed position, as in $X_i(t) = (1-t)X_i^A + tX_i^B$. Alternative formulations for initially curved elements follow the same exact procedure, but obviously require non-linear interpolations for the undeformed coordinates; an obvious choice is to use identical interpolation as the deformed coordinates, i.e. an isoparametric element.

From here, the computation of the mechanical performance of the beam is trivial, though the resulting algebraic forms are somewhat lengthy. Using the above, and recognizing $s'_o = \sqrt{X'_i X'_i} = \ell_o$ for straight beams with linear interpolation of the *undeformed* coordinates, one must compute:

$$\frac{ds}{ds_o} = \frac{s'(t)}{s'_o(t)} = \frac{\sqrt{x'_i(t)x'_i(t)}}{\ell_o} \tag{6.9}$$

which yields the stretch in the beam as function of the implicit (interpolation) parameter t. One can use eqns. (6.5 -6.7) to demonstrate that $ds/ds_o(t=0) = \lambda_A$ and $ds/ds_o = \lambda_B$; further, one can easily show that the angles at the ends are given by:

$$\frac{dx_1}{ds}(t=0) = \frac{x'_1}{s'} = \cos\theta_A; \quad \frac{dx_2}{ds}(t=0) = \frac{x'_2}{s'} = \sin\theta_A \tag{6.10}$$

and so forth for the slopes of the deformed state at $t = 1$, i.e. $dx_1/ds = \cos\theta_B$ and $dx_2/ds = \sin\theta_B$. This has important implications for continuity; consider if one were to approximate stretch in the element as uniform and use the end-points to compute it, i.e. $\ell_o\lambda_A \approx \sqrt{(x_i^B - x_i^A)(x_i^B - x_i^A)}$. (This is obviously attractive because it eliminates two nodal degrees of freedom, i.e. $\lambda^{A,B}$.) However, this can lead to discontinuity in curvature (manifested as 'kinking' in the deformed state), as will be come clear from what follows.

The curvature of the beam is computed from

$$\frac{d\theta}{ds_o} = \frac{1}{\ell_o}\frac{d}{dt}\left(\tan^{-1}\frac{x_2'(t)}{x_1'(t)}\right) = \frac{1}{\ell_o}\left(\frac{x_1'(t)x_2''(t) - x_1'(t)x_2'(t)}{x_i'x_i'}\right) \tag{6.11}$$

Here again, assuming uniform stretch (instead of eqn. 6.9) which would imply $x_i'x_i' = (s'(t))^2 \approx \ell^2$. In turn, this with eqn. 6.11 would imply $d\theta/ds_o$ is not continuous across element boundaries (as ℓ is different for each element). This is the essence of 'kinking'; while such phenomena can be eliminated by imposing additional constraints relating to the jump in angle between the lines formed between element end-points, the present formulation avoids this entirely by using stretch at the nodes as an explicit variable.

As will be illustrated, a single element is only capable of producing uniform curvature in the limit that the radius of curvature is much smaller than the element length; this is a consequence of the fact that cubic interpolations are only fair approximations for a circle. As will be noted, it is interesting to note that while deviations from exactly solutions for a significant curvature (say, on the order of the beam length) are not significant, the *average* curvature shows very small deviations from an exact result.

The results above allow one to compute the energy in the element through the use of eqns. (6.5 -6.11) and numerical integration. For small stretch (e.g. when the cross-section dimensions of the beam are not appreciably altered by axial stretch), the strain in the beam is $\epsilon(t) = \lambda(t) - 1$, and the strain energy can be written as:

$$\begin{aligned}\Pi_e &= \frac{1}{2}\int_0^{\ell_o}\left[EA\left(\frac{ds}{ds_o}-1\right)^2 + EI\left(\frac{d\theta}{ds_o}\right)^2\right]ds_o \\ &= \frac{\ell_o}{2}\int_0^{1}\left[EA\left(\frac{ds}{ds_o}-1\right)^2 + EI\left(\frac{d\theta}{ds_o}\right)^2\right]dt\end{aligned} \tag{6.12}$$

where A is the cross-sectional area of the beam and I is the moment of inertia. For a given set of nodal quantities, eqn. 6.12 is evaluated numerically, and direct search

algorithms can be applied to the sum of strain energy across all elements. To apply external forces or moments, one can subtract additional terms corresponding to the potential energy associated with the set of generalized nodal 'forces' (i.e. work conjugate terms to the nodal displacements). The appropriate generalized work conjugate 'forces' can be computed as follows, which also provides the method to compute the reaction forces when nodal variables are explicitly prescribed.

The variation in potential energy for an element with applied nodal forces and moments can be written as:

$$\begin{aligned}\delta\Pi &= \ell_o \int_0^1 \left[EA\left(\frac{ds}{ds_o}-1\right)\delta\left(\frac{ds}{ds_o}\right) + EI\frac{d\theta}{ds_o}\delta\left(\frac{d\theta}{ds_o}\right)\right] dt \\ &\quad - \left(F_1^A\delta x_1^A + F_2^A\delta x_2^A + M^A\delta\theta_A + \Lambda^A\delta\lambda_A\right) \\ &\quad - \left(F_1^B\delta x_1^B + F_2^B\delta x_2^B + M^B\delta\theta_B + \Lambda^B\delta\lambda_B\right) = 0 \end{aligned} \tag{6.13}$$

where $F_i^{A,B}$ are nodal forces applied to the end-points, $M^{A,B}$ are the nodal moments, and $\Lambda^{A,B}$ are higher order terms that are shown numerically to be zero when stretch is not prescribed at a node. Note that since $\delta x_i(t) = \delta\left[X_i(t) + u_i(t)\right]$, we have $\delta u_i = \delta x_i$; hence, the nodal force terms are the usual ones irrespective of the fact they are acting on the variation of global deformed position. We can lump the external force terms into a generalized vector of nodal forces, i.e. replace them with $[P]_{1x8}^T[\delta Q]_{8x1}$, where P is a general notation for all work conjugate force/moment terms, and δQ is the general notation for the variation in the deformation variables at the nodes.

For the variation in axial stretch, we have:

$$\delta\left(\frac{ds}{ds_o}\right) = \frac{1}{\ell_o\sqrt{x_i'x_i'}}\left(x_1'\delta x_1' + x_2'\delta x_2'\right) \tag{6.14}$$

$$= \begin{bmatrix} \frac{x_1'}{\ell_o\sqrt{x_i'x_i'}} & \frac{x_2'}{\ell_o\sqrt{x_i'x_i'}} & 0 & 0 \end{bmatrix} \begin{bmatrix} \delta x_1' \\ \delta x_2' \\ \delta x_1'' \\ \delta x_2'' \end{bmatrix} \tag{6.15}$$

$$= \left[I_\lambda\right]_{1x4}\left[B(t)\right]_{4x8}\left[\delta Q\right]_{8x1} \tag{6.16}$$

where $\left[I_\lambda\right]_{1x4}$ can be inferred from the above, while $\left[B(t)\right]_{4x8}$ can be found by differentiating the global positions and taking the variation with respect to nodal variables; full results are given in the Appendix.

Similarly, for the variation in curvature, we have:

$$\delta\left(\frac{d\theta}{ds_o}\left[x_i', x_i''\right]\right) = \frac{\partial}{\partial x_1'}\frac{d\theta}{ds_o}\delta x_1' + \frac{\partial}{\partial x_2'}\frac{d\theta}{ds_o}\delta x_2' + \frac{\partial}{\partial x_1''}\frac{d\theta}{ds_o}\delta x_1'' + \frac{\partial}{\partial x_2''}\frac{d\theta}{ds_o}\delta x_2'' \tag{6.17}$$

$$\begin{aligned} &= \left(\frac{2x_1'x_2'x_1'' + \left[\left(x_2'\right)^2 - \left(x_1'\right)^2\right]x_2''}{\ell_o\left[\left(x_1'\right)^2 + \left(x_2'\right)^2\right]^2}\right)\delta x_1' \\ &\quad + \left(\frac{\left[\left(x_2'\right)^2 - \left(x_1'\right)^2\right]x_1'' - 2x_1'x_2'x_2''}{\ell_o\left[\left(x_1'\right)^2 + \left(x_2'\right)^2\right]^2}\right)\delta x_2' \\ &\quad - \left(\frac{x_2'}{\ell_o\left[\left(x_1'\right)^2 + \left(x_2'\right)^2\right]}\right)\delta x_1'' \\ &\quad + \left(\frac{x_1'}{\ell_o\left[\left(x_1'\right)^2 + \left(x_2'\right)^2\right]}\right)\delta x_2'' \end{aligned} \tag{6.18}$$

$$= \left[I_\kappa\right]_{1x4}\left[B(t)\right]_{4x8}\left[\delta Q\right]_{8x1} \tag{6.19}$$

where again the entries of $\left[I_\kappa\right]_{1x4}$ can be inferred from the above, and $\left[B(t)\right]$ and $\left[\delta Q\right]$ are

identical to the prior result. This implies that the nodal forces are given by:

$$[P]^T_{1x8} = \ell_o \int_0^1 \left(EA \left(\frac{ds}{ds_o} - 1 \right) [I_\lambda]_{1x4} + EI \frac{d\theta}{ds_o} [I_\kappa]_{1x4} \right) [B(t)]_{4x8} \, dt \tag{6.20}$$

Naturally, one could sum the nodal forces arising from each element and set the result to zero; doing so involves lengthy non-linear equations in terms of the nodal variables. For direct search methods, this is unnecessary, and eqn. 6.20 is only used to compute the reaction forces associated with each degree of freedom.

The variation of potential energy implies that the work terms that are conjugate to the stretch should be zero when stretch is left as a free variable; this indeed turns out to be the case numerically.

6.3 Numerical solution techniques

The formulation outlined in the previous section forms the basis for several numerical solution techniques. The simplest and most straightforward to implement is direct energy minimization, using the total energy of a system defined by multiple elements; the energy for each element can be computed directly through numerical integration of eqn. 6.12. The nodal variables that minimize the system's total energy are then solved for using standard minimization algorithms. Alternatively, one can utilize non-linear root solving algorithms in conjunction with the above description of nodal forces; in this approach, a global system of equations is assembled by summing the forces at nodes associated with connected elements.

To explore the performance of the element, a variety of energy minimization techniques were explored using the commercial code ABAQUS, i.e. Monte Carlo, Nelder-Mead and Newton-Raphson methods. The first two are direct search methods that do

not involve derivatives of the global energy function. Newton-Raphson relies on numerical differentiation of the energy potential to compute derivatives used during energy minimization iterations. A broad range of numerical parameters were considered to explore the efficiency of the various methods. By and large, the study was inconclusive, in the sense that each method has advantages and disadvantages pertaining to classical trade-offs between accuracy and robustness. In the benchmarking cases in the next section, results were generated by Monte Carlo method, which offers more efficient scaling as the number of elements (degrees of freedom) is increased. The performance of the element in these cases is then used as the basis for the discussion of future work addressing numerical implementation.

6.4 Benchmarking cases

To validate the above framework and generate insight regarding the effectiveness of direct search algorithms, several benchmark cases involving large rotations with analytical solutions were analyzed; all of them invoke the assumption that stretching in the beam is negligible, the so-called "elastica" limit. Hence, the focus is on the element's ability to capture arbitrarily large rotations.

Elastica cantilever with end moment

Consider a cantilever of length ℓ_o lying along the X_1-axis such that $dX_1/ds_o = \ell_o$, subjected to a pure moment at the free end, M, and assume that the axial stretch is negligible such that $ds/ds_o = 1$. The solution is uniform curvature given by $EId\theta/ds_o = M$; hence, $\theta(X_1) = (M\ell_o/EI)X_1 \equiv \tilde{M}X_1$. Thus, noting that $dx_1/ds = dx_1/ds_o = \cos\theta$,

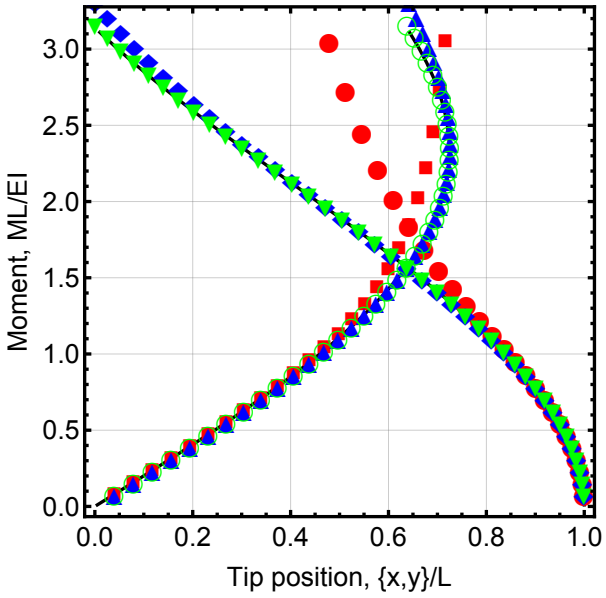

Figure 6.2: Comparison of elastica theory for a cantilever with an applied moment at the tip and Bezier finite element results, for $A\ell_o^2/I = 10^4$. Key: red-1 element, blue-2 elements, green-3 elements.

$dx_2/ds = dx_2/ds_o = \sin\theta$, $x_1(s_o = 0)$ and $x_2(s_o = 0)$=0

$$x_1(X_1) = \frac{1}{\tilde{M}} \sin\left(\tilde{M}_o \frac{X_1}{\ell_o}\right); \quad x_2(X_1) = \frac{1}{\tilde{M}}\left[1 - \cos\left(\tilde{M}_o \frac{X_1}{\ell_o}\right)\right] \tag{6.21}$$

Figure 6.2 illustrates the relationship between the tip position of the cantilever and the applied moment; the beam curls upwards (a positive moment is applied), such that the horizontal position of the tip decreases and the vertical position increases. The results illustrate that the present beam formulation is efficient, with three elements being sufficient to completely capture the large rotation response. By comparison, a simulation with conventional Bernoulli-Euler beam elements requires five to six elements. Hence, the novel interpolation functions used in the present formulation are more efficient that conventional elements for this particular case.

Buckling of a pinned elastica beam

Consider a cantilever of length ℓ_o lying along the X_1-axis such that $dX_1/ds_o = \ell_o$, subjected to a pure horizontal compressive force at the free end, $F = -F_1(\ell_o)$, and assume that the axial stretch is negligible such that $ds/ds_o = 1$. A free body diagram reveals that the moment at any location is given by $M = EId\theta/ds_o = -Fx_2$. Taking the derivative, we note $dM/ds_o = EId^2\theta/ds_o^2 = -Fdx_2/ds_o = -F\sin\theta$, since $ds/ds_o = 1$. For convenience, define $\tilde{s}_o = s_o/\ell_o$. Hence, the governing equation is simply:

$$\theta'' + \tilde{F}\sin\theta = 0 \tag{6.22}$$

where $(\,)' = d/d\tilde{s}_o$, $\tilde{F} = F\ell_o^2/EI$ and the boundary conditions are $\theta'(0) = 0$ and $\theta'(\tilde{s}_o = 1) = 0$, since the moments are zero at the ends. Multiplying by θ' and integrating, we observe:

$$\left[\frac{1}{2}\left(\theta'\right)^2 - \tilde{F}\cos\theta\right] = C \tag{6.23}$$

The constant can be cast in terms of the rotation at one end, e.g. $\theta_o = \theta(0)$: replacing the integration constant with $\tilde{-}F\cos\theta_o$ (since $\theta'(0) = 0$), we obtain:

$$\theta' = \pm\sqrt{2\tilde{F}}\sqrt{\cos\theta - \cos\theta_o} = \frac{d\theta}{d\tilde{s}_o} \tag{6.24}$$

The solution for an upward buckle (where $\phi_o > 0$ and $\theta' < 0$) is found by integrating both sides, yielding:

$$\sqrt{2\tilde{F}}\tilde{s}_o = \int_{\theta(\tilde{s}_o)}^{\theta_o} \frac{d\theta}{\sqrt{\cos\theta - \cos\theta_o}} \tag{6.25}$$

For a symmetric buckle, $\theta(\tilde{s}_o = 1/2) = 0$ (i.e. the slope at the center of the beam is zero), such that the load can be determined as function of the initial slope by:

$$\tilde{F}\left(\theta_o\right) = 2\left[\int_0^{\theta_o} \frac{d\theta}{\sqrt{\cos\theta - \cos\theta_o}}\right]^2, \tag{6.26}$$

which is an elliptical integral of the first kind, and can be determined numerically. (Such functions are explicitly defined in *Mathematica*.) For small θ_o, we obtain $\tilde{F} = \pi^2$, which corresponds to Euler's classical buckling result. Let $\tilde{x}_i = x_i/\ell_o$; the deformed state can be determined from $\tilde{x}_1' = \cos\theta$ and $\tilde{x}_2' = \sin\theta$. Using these with equation 6.24 and noting that the deformation is symmetric, we obtain the following:

$$\tilde{x}_2^{max} = \tilde{x}_2(1/2) = \frac{1}{\sqrt{2\tilde{F}}}\int_0^{\theta_o} \frac{\sin\theta d\theta}{\sqrt{\cos\theta - \cos\theta_o}} \tag{6.27}$$

$$\tilde{x}_1(1/2) = \frac{1}{\sqrt{2\tilde{F}}}\int_0^{\theta_o} \frac{\cos\theta d\theta}{\sqrt{\cos\theta - \cos\theta_o}} \tag{6.28}$$

Note that from symmetry, the horizontal displacement in the loading end is twice that of the horizontal displacement of the loading end, such that $\tilde{x}_1(1) = 2\tilde{x}_1(1/2)$.

Figure 6.3 illustrates the response of the pinned beam subjected to axial compression. As the end displacement increases, the structure buckles into an arc shape with finite rotation at the ends and maximum displacement in the center. For this particular problem six elements are required for highly accurate response; this is consistent with the previous benchmark, in the sense that the pinned beam has mirrored symmetry. It is apparent that three elements per 90^o arc are needed to accurately capture response. This provides a useful guideline to the number of elements needed for large rotations; for example, if the ends were clamped (which does not afford a numerical solution), then large rotations forming a loop will require four times as many elements.

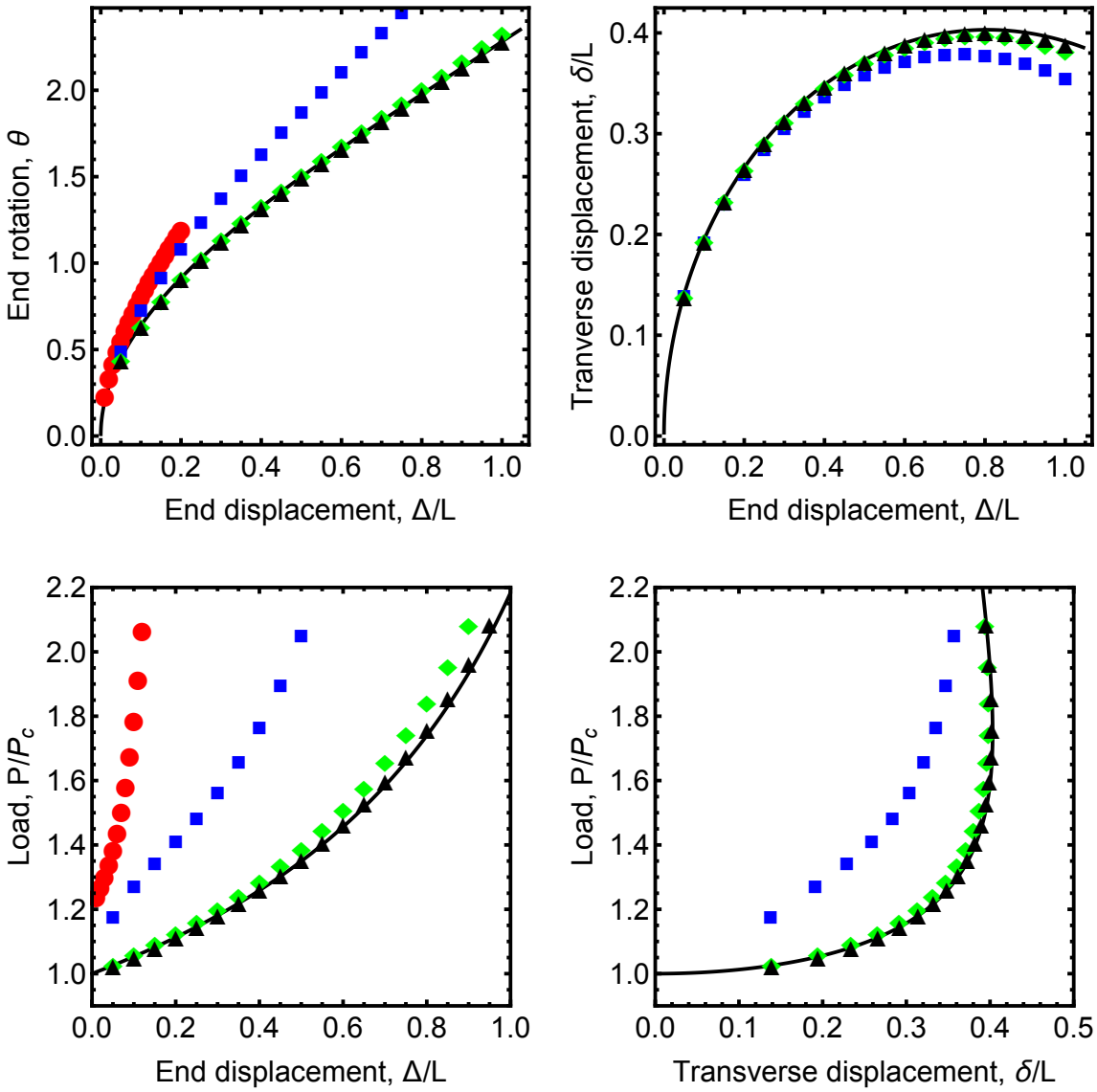

Figure 6.3: Comparison of elastica theory for a pinned-pinned beam loaded in compression (buckling) and Bezier finite element results, for $A\ell_o^2/I = 10^4$. Key: red-1 element, blue-2 elements, green-4 elements, black-6 elements.

Elastica cantilever with a dead transverse load

Consider a cantilever of length ℓ_o lying along the X_1-axis such that $dX_1/ds_o = \ell_o$, subjected to a pure vertical force at the free end, $F = -F_2(\ell_o)$, and assume that the axial stretch is negligible such that $ds/ds_o = 1$. A free body diagram reveals that the moment at any location is given by $M = EId\theta/ds_o = -Fx_1$. Taking the derivative, we note $dM/ds_o = EId^2\theta/ds_o^2 = -Fdx_1/ds_o = -F\cos\theta$, since $ds/ds_o = 1$. For convenience, define $\tilde{s}_o = s_o/\ell_o$. Hence, the governing equation is simply:

$$\theta'' + \tilde{F}\cos\theta = 0 \tag{6.29}$$

where $(\,)' = d/d\tilde{s}_o$, $\tilde{F} = F\ell_o^2/EI$ and the boundary conditions are $\theta(0) = 0$ and $\theta'(\tilde{s}_o = 1) = 0$, since the slope at the clamped end and moment at the free end are zero. The solution follows that of the previous section, only with the slope at the free end, $\theta_1 = \theta(\tilde{s}_o = 1)$ as the unknown parameter.

$$\tilde{F}(\theta_1) = \frac{1}{2}\left[\int_0^{\theta_1} \frac{d\theta}{\sqrt{\sin\theta - \sin\theta_1}}\right]^2, \tag{6.30}$$

which again can be determined numerically. (Such functions are explicitly defined in *Mathematica*.) Again, let $\tilde{x}_i = x_i/\ell_o$; the deformed state can be determined from $\tilde{x}_1' = \cos\theta$ and $\tilde{x}_2' = \sin\theta$. Using these, we obtain the following for the tip position:

$$\tilde{x}_1(1) = \frac{1}{\sqrt{2\tilde{F}}}\int_0^{\theta_1} \frac{\cos\theta d\theta}{\sqrt{\sin\theta - \sin\theta_1}} \tag{6.31}$$

$$\tilde{x}_2(1) = \frac{1}{\sqrt{2\tilde{F}}}\int_0^{\theta_o} \frac{\sin\theta d\theta}{\sqrt{\cos\theta - \cos\theta_o}} \tag{6.32}$$

These results fully define the tip position and load as a function of the implicit as a function of the implicit parameter θ_1.

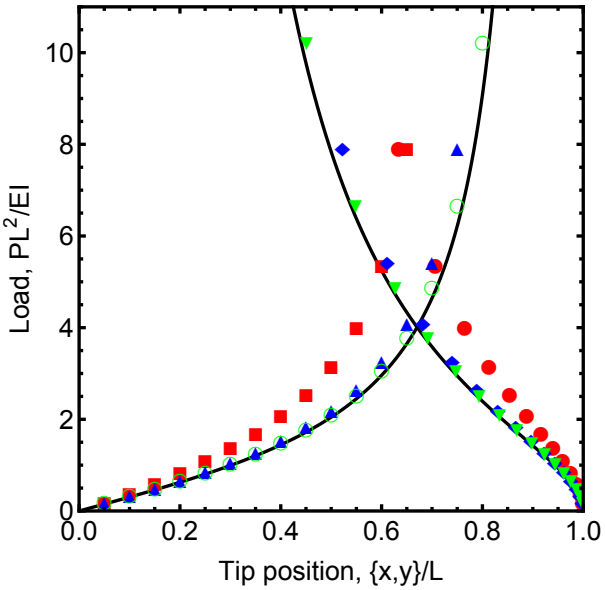

Figure 6.4: Comparison of elastica theory for a cantilever with an load at the tip and Bezier finite element results, for $A\ell_o^2/I = 10^4$. Key: red-1 element, blue-2 elements, green-3 elements.

Figure 6.4 illustrates a comparison of elastic theory and the present beam formulation; as the load increase, the tip position moves upwards and to the left. As in the case with applied end moments, the formulation of a single arc requires only three elements for accurate results.

6.5 Discussion and future Work

The benchmark cases illustrated in the previous section illustrate the accuracy of the beam formulation; based on comparisons with traditional Bernoulli-Euler elements, the novel interpolation adopted here is moderately more efficient, in that the number of required elements for arbitrary large rotations is cut in half as a general rule. This has important implications for large-scale involving a multitude of slender beams, but less so for structures involving a limited number of members.

The advantage of the present formulation for large scale systems lies in the fact that it provides a direct calculation of energy, and as such can be utilized with non-gradient methods for energy minimization. As gradient-based methods are well-known to scale poorly for systems with large degrees of freedom, the present formulation may offer key speed advantages for such systems. Unfortunately, the implementation of the formulation in non-parallel codes did not offer much speed advantage, for the limited number of cases studied in this work. Generally speaking, Monte-Carlo simulations with sufficiently small perturbations to capture buckling instabilities performed comparably to gradient-based methods. This is undoubtedly a consequence of the fact that only systems with few degrees of freedom (less than 20 or so) were explored, and critically, the implementation of Monte Carlo methods did not include parallel computing.

To scale up to larger systems and more rigorously assess the potential advantage of the present formulation, highly parallel implementations are required. Direct energy minimization of other highly non-linear systems on highly parallel platforms such as GPUs has been demonstrated to offer significant computational advantages [85–87]. This strongly suggests that the present formulation in similar parallel frameworks will offer significant advantages to gradient-based methods, owing to the fact that gradient based methods do not enjoy significant gains from parallelization. Hence, future work should focus on exploring the efficiency of the present formulation in such frameworks for large systems involving thousands of members.

6.6 Appendix

For the element, the variations in the displacement gradients is written in terms of the variation of the nodal quantities as:

$$\begin{bmatrix} \delta x_1' \\ \delta x_2' \\ \delta x_1'' \\ \delta x_2'' \end{bmatrix} = \begin{bmatrix} N_1' & 0 & -N_2'\ell_o\lambda_A\sin\theta_A & N_2'\ell_o\cos\theta_A & N_3' & 0 & -N_4'\ell_o\lambda_B\sin\theta_B & N_4'\ell_o\cos\theta_B \\ 0 & N_1' & N_2'\ell_o\lambda_A\cos\theta_A & N_2'\ell_o\sin\theta_A & 0 & N_3' & N_4'\ell_o\lambda_B\cos\theta_B & N_4'\ell_o\sin\theta_B \\ N_1'' & 0 & -N_2''\ell_o\lambda_A\sin\theta_A & N_2''\ell_o\cos\theta_A & N_3'' & 0 & -N_4''\ell_o\lambda_B\sin\theta_B & N_4''\ell_o\cos\theta_B \\ 0 & N_1'' & N_2''\ell_o\lambda_A\cos\theta_A & N_2''\ell_o\sin\theta_A & 0 & N_3'' & N_4''\ell_o\lambda_B\cos\theta_B & N_4''\ell_o\sin\theta_B \end{bmatrix} \begin{bmatrix} \delta x_1^A \\ \delta x_2^A \\ \delta\theta_A \\ \delta\lambda_A \\ \delta x_1^B \\ \delta x_2^B \\ \delta\theta_B \\ \delta\lambda_B \end{bmatrix}$$

$$= [B(t)]_{4x8}\,[\delta Q]_{8x1} \tag{6.33}$$

Chapter 7

Conclusions and future work

The results from this dissertation provide important insights and capabilities for the design of cellular structures that control non-linear material response and energy absorption during compressive loading. Specifically, these contributions support the following general conclusions, and recommendations for future work:

Post-buckling behaviors in structures with angled struts:

- The behavior of angled struts provides important insights regarding the role of post-buckling behaviors, notably the transition from compression-controlled softening to tension-controlled stiffening. The models presented in this work provide an efficient basis to consider novel architectures with multiple angled struts which can improve strength and energy absorption. In addition, the models should find utility in the development of 'programmable materials' that are designed to exhibit multiple stable deformation states. A key contribution is the ability to estimate strut strains during snap-through, which can guide material selection and set limits of cell topologies that produce robust response.

- Predictions of viscoelastic struts that experience moderate rotations illustrate that significant increases in damping are possible due to non-linear response, even in scenarios where the quasi-static response shows no hysteresis. For structures that exhibit snap-through, the combination of structural and material hysteresis leads to dramatic increases in damping during cyclic loading. The models provide a quantitative basis to estimate the level of intrinsic damping needed to stabilize dynamic events associated with snap-through, which should find utility in the design of effective cellular materials with multiple stable states.

- Future work should focus on the cyclic hysteresis exhibited by angled struts, with more sophisticated material models that can be correlated with standard viscoelasticity parameters. That is, the standard linear model utilized in Chapter 5 on damped resonance response should be incorporated into the angled strut model, such that the implications of specific material selections are more easily understood. This exercise should provide insight into the moderate amounts of hysteresis exhibited in stochastic foams; i.e., the hysteresis exhibited by angled struts and arising from viscoelastic is likely to be effective in quantifying links between base properties and foam response.

Simulations and design of cellular structures with multiple internal struts:

- Large deformation simulations of structures with multiple internal struts is made challenging by strong non-linearities and bifurcations; different topologies exhibit widely different degrees of imperfection sensitivity. A detailed study of four different topologies with hundreds of different geometry parameters has established numerical parameters – including mesh size, loading rate, imperfection definition, heuristic damping parameters – that are effective in achieving consistent results for their strength and energy absorption. Nevertheless, the strong sensitivity of re-

sponse to small changes in geometry indicates the design space is highly complex, and claims of broadly applicable numerical procedures are worthy of skepticism. Future work based on direct energy minimization of structures using global formulations (such as that presented in Chapter 5) is a potentially promising pathway to improve studies on the effect of topology for structures involving large rotations.

- The use of internal braces to sub-divide larger cells is a promising pathway to control post-buckling behaviors, with increases in strength and energy absorption of about a factor of three. Braces between buckling-dominated struts that lie perpendicular to the loading direction are highly effective in controlling post-buckling stability leading to large improvements in energy absorption; however, the concomitant change in strength is negligible. Angled internal struts are more effective in increasing both strength and energy absorption; connections associated with the first buckling mode of the larger cell structure are most effective.

- Future work should focus on extending the insights generated in this work to structures with more than a single 'macro-cell'. As the results of this dissertation indicate that this extension will be computationally expensive, focus should be on triangular cells that are subdivided into smaller triangles. The results presented here suggest that uniaxial response can be significantly improved if the sub-divisions are not based on uniform sub-divisions, but rather the inclusion of sub-cells that are not isotropic.

Damping near resonances in cellular structures:

- The framework presented in this work is a highly efficient pathway to predict the implications of material selection and topology on forced, damped response of cellular materials. The scaling relationships elucidated in Chapter 5 illustrate that

optimal responses are achieved when the characteristic frequency of the viscoelastic material are 'tuned' to match the frequency of the resonance mode for which damping is sought. For isotropic prismatic honeycombs subject to lateral compression, the level of structural damping mirrors the loss factors of the base material, due to the fact a standing wave is established in the loading direction.

- Loss factors for honeycombs comprising composite struts can be significantly higher than the stiff phase utilized to provide static stiffness, suggesting that composite cellular materials can significantly improve damping over monolithic materials with high stiffness and low damping. This suggests a clear pathway to creating lightweight structures with both high stiffness and improved damping; for example, include a high damping elastomer in a stiff polymer with relatively low damping can reduce resonsance response by a factor of 5-10; high damping metals such as tin used as filler materials inside low damping shells can lead to similar improvements. The increase in damping is most pronounced when the modulus of the high damping phase is within a factor of twenty of the modulus of the low-damping phase.

- Cellular structures that comprise a distribution of cell sizes and shapes can be effective in improving damping in monolithic material structures; the improvements are most effective when internal cells are included that disrupt the formation of standing waves established during uniaxial resonance. Damping increases of a factor of two were demonstrated with concomitant increases in structural stiffness; this strongly suggests that topology optimization can be exploited to identify non-uniform cell distributions that lead to further increases. The efficiency of the numerical framework presented here sets the stage for such efforts.

- Future work should focus on the interplay of material selection and topology in

controlling structural resonance. An important advance would be a tabulation of the frequency response of various polymers; while temperature-frequency superposition methods are well-known, existing data in the literature is relatively sparse. Quantification of the frequency response of common elastomer and glassy polymer formulations is needed to determine whether the damping gains illustrated in this work can be realized in structures with dimensions relevant to key applications.

Bibliography

[1] T. A. Schaedler and W. B. Carter, "Architected cellular materials," *Annual Review of Materials Research*, vol. 46, pp. 187–210, 2016.

[2] L. Gibson, "Modelling the mechanical behavior of cellular materials," *Materials Science and Engineering: A*, vol. 110, pp. 1–36, 1989.

[3] D. V. Dounis and G. L. Wilkes, "Structure-property relationships of flexible polyurethane foams," *Polymer*, vol. 38, no. 11, pp. 2819–2828, 1997.

[4] N. Mills, "Finite element models for the viscoelasticity of open-cell polyurethane foam," *Cellular polymers*, vol. 25, no. 5, pp. 293–316, 2006.

[5] P. Scarfato, L. Di Maio, L. D'Arienzo, S. Rinaldi, and L. Incarnato, "Composition-structure-property relationships of commercial polyurethane foams for mattresses," *AIP Conference Proceedings*, vol. 1695, no. 1, p. 020048, 2015.

[6] L. J. Gibson and M. F. Ashby, *Cellular solids: structure and properties*. Cambridge university press, 1999.

[7] V. S. Deshpande, N. A. Fleck, and M. F. Ashby, "Effective properties of the octet-truss lattice material," *Journal of the Mechanics and Physics of Solids*, vol. 49, no. 8, pp. 1747–1769, 2001.

[8] J. Bauer, S. Hengsbach, I. Tesari, R. Schwaiger, and O. Kraft, "High-strength cellular ceramic composites with 3d microarchitecture," *Proceedings of the National Academy of Sciences*, vol. 111, no. 7, pp. 2453–2458, 2014.

[9] H. A. Eschenauer and N. Olhoff, "Topology optimization of continuum structures: a review," *Applied Mechanics Reviews*, vol. 54, no. 4, pp. 331–390, 2001.

[10] F. Côté, V. Deshpande, N. Fleck, and A. Evans, "The compressive and shear responses of corrugated and diamond lattice materials," *International Journal of Solids and Structures*, vol. 43, no. 20, pp. 6220–6242, 2006.

[11] M. Crisfield, "A fast incremental/iterative solution procedure that handles "snap-through"," in *Computational Methods in Nonlinear Structural and Solid Mechanics*, pp. 55–62, Elsevier, 1981.

[12] P. J. Tan, J. J. Harrigan, and S. R. Reid, "Inertia effects in uniaxial dynamic compression of a closed cell aluminium alloy foam," *Materials Science and Technology*, vol. 18, no. 5, pp. 480–488, 2002.

[13] K.-J. Bathe, *Finite element procedures*. Klaus-Jurgen Bathe, 2006.

[14] T. E. Bruns and D. A. Tortorelli, "Topology optimization of non-linear elastic structures and compliant mechanisms," *Computer Methods in Applied Mechanics and Engineering*, vol. 190, no. 26–27, pp. 3443 – 3459, 2001.

[15] T. Mullin, S. Deschanel, K. Bertoldi, and M. C. Boyce, "Pattern transformation triggered by deformation," *Phys. Rev. Lett.*, vol. 99, p. 084301, Aug 2007.

[16] K. Bertoldi and M. C. Boyce, "Mechanically triggered transformations of phononic band gaps in periodic elastomeric structures," *Phys. Rev. B*, vol. 77, p. 052105, Feb 2008.

[17] D. Krishnan and H. Johnson, "Optical properties of two-dimensional polymer photonic crystals after deformation-induced pattern transformations," *Journal of the Mechanics and Physics of Solids*, vol. 57, no. 9, pp. 1500 – 1513, 2009.

[18] J.-H. Jang, C. Y. Koh, K. Bertoldi, M. C. Boyce, and E. L. Thomas, "Combining pattern instability and shape-memory hysteresis for phononic switching," *Nano Letters*, vol. 9, no. 5, pp. 2113–2119, 2009. PMID: 19391612.

[19] S. Singamaneni, K. Bertoldi, S. Chang, J.-H. Jang, S. L. Young, E. L. Thomas, M. C. Boyce, and V. V. Tsukruk, "Bifurcated mechanical behavior of deformed periodic porous solids," *Advanced Functional Materials*, vol. 19, no. 9, pp. 1426–1436, 2009.

[20] T. Bückmann, N. Stenger, M. Kadic, J. Kaschke, A. Frölich, T. Kennerknecht, C. Eberl, M. Thiel, and M. Wegener, "Tailored 3d mechanical metamaterials made by dip-in direct-laser-writing optical lithography," *Advanced Materials*, vol. 24, no. 20, pp. 2710–2714, 2012.

[21] S. Shan, S. H. Kang, J. R. Raney, P. Wang, L. Fang, F. Candido, J. A. Lewis, and K. Bertoldi, "Multistable architected materials for trapping elastic strain energy," *Advanced Materials*, vol. 27, no. 29, pp. 4296–4301, 2015.

[22] N. Hu and R. Burgueno, "Buckling-induced smart applications: recent advances and trends," *Smart Materials and Structures*, vol. 24, p. 063001, 2015.

[23] T. Fenzel, C. Findeisen, M. Kadic, P. Gumbsch, and M. Wegener, "Tailored buckling microlattices as reusable light-weight shock absorbers," *Journal of the Mechanics and Physics of Solids*, vol. 102, pp. 151–164, 2017.

[24] C. Findeisen, J. Hohe, M. Kadic, and P. Gumbsch, "Characteristics of mechanical metamaterials based on buckling elements," *Journal of the Mechanics and Physics of Solids*, vol. 102, pp. 151 – 164, 2017.

[25] B. Haghpanah, A. Shirazi, L. Salari-Sharif, A. G. Izard, and L. Valdevit, "Elastic architected materials with extreme damping capacity," *Extreme Mechanics Letters*, vol. 17, pp. 56–61, 2017.

[26] Q. Chen, X. Zhang, and B. Zhu, "Design of buckling-induced mechanical metamaterials for energy adsorption using topology optimization," *Structural and Multidisciplinary Optimization*, vol. 58, no. 4, pp. 1395–1410, 2018.

[27] C. S. Ha, R. Lakes, and M. Plesha, "Design, fabrication and analysis of lattice exhibiting energy adsorption through snap-through behavior," *Materials and Design*, vol. 141, pp. 426–437, 2018.

[28] F. W. WILLIAMS, "An approach to the non-linear behaviour of the members of a rigid jointed plane framework with finite deflections," *The Quarterly Journal of Mechanics and Applied Mathematics*, vol. 17, no. 4, pp. 451–469, 1964.

[29] A. Jennings, "Frame analysis including change of geometry," *Journal of the Structural Division*, vol. 94, no. 3, pp. 627–644, 1968.

[30] R. Wood and O. Zienkiewicz, "Geometrically nonlinear finite element analysis of beams, frames, arches and axisymmetric shells," *Computers & Structures*, vol. 7, no. 6, pp. 725 – 735, 1977.

[31] B. A. RADOMSKE, *Large Deflection Analysis of Shallow Framed Structures*. PhD thesis, University of British Columbia, 1972.

[32] M. Papadrakakis, "Post-buckling analysis of spatial structures by vector iteration methods," *Computers & structures*, vol. 14, no. 5, pp. 393–402, 1981.

[33] J. Meek and H. S. Tan, "Geometrically nonlinear analysis of space frames by an incremental iterative technique," *Computer Methods in Applied Mechanics and Engineering*, vol. 47, no. 3, pp. 261 – 282, 1984.

[34] D. Pecknold, J. Ghaboussi, and T. Healey, "Snap-through and bifurcation in a simple structure," *Journal of engineering mechanics*, vol. 111, no. 7, pp. 909–922, 1985.

[35] K. Kondoh, K. Tanaka, and S. Atluri, "An explicit expression for the tangent-stiffness of a finitely deformed 3-d beam and its use in the analysis of space frames," *Computers & structures*, vol. 24, no. 2, pp. 253–271, 1986.

[36] E. Lui and W.-F. Chen, "Analysis and behaviour of flexibly-jointed frames," *Engineering Structures*, vol. 8, no. 2, pp. 107 – 118, 1986.

[37] K.-M. Nee and A. Haldar, "Elastoplastic nonlinear post-buckling analysis of partially restrained space structures," *Computer methods in applied mechanics and engineering*, vol. 71, no. 1, pp. 69–97, 1988.

[38] L. H. Teh and M. J. Clarke, "Co-rotational and lagrangian formulations for elastic three-dimensional beam finite elements," *Journal of Constructional Steel Research*, vol. 48, no. 2–3, pp. 123 – 144, 1998.

[39] S. Lopez, "Post-critical analysis of structures with a nonlinear pre-buckling state in the presence of imperfections," *Computer Methods in Applied Mechanics and Engineering*, vol. 191, no. 39–40, pp. 4421 – 4440, 2002.

[40] Y.-B. Yang, J.-D. Yau, and L.-J. Leu, "Recent developments in geometrically nonlinear and postbuckling analysis of framed structures," *Applied Mechanics Reviews*, vol. 56, no. 4, pp. 431–449, 2003.

[41] J. Casals-Terre and A. Shkel, "Dynamic analysis of a snap-action micromechanism," in *Sensors, 2004. Proceedings of IEEE*, pp. 1245–1248 vol.3, Oct 2004.

[42] J. Qiu, J. H. Lang, and A. H. Slocum, "A curved-beam bistable mechanism," *Microelectromechanical Systems, Journal of*, vol. 13, no. 2, pp. 137–146, 2004.

[43] L. Gong, S. Kyriakides, and N. Trantafyllidis, "On the stability of kelvin cell foams under compressive loads," *Journal of the Mechanics and Physics of Solids*, vol. 53, pp. 771–794, 2005.

[44] C. Coulais, J. Overvelde, L. Lubers, K. Bertoldi, and M. van Hecke, "Discontinuous buckling of wide beams and metabeams," *Physical review letters*, vol. 115, p. 044301, 2015.

[45] M. Vangbo, "An analytical analysis of a compressed bistable buckled beam," *Sensors and Actuators A: Physical*, vol. 69, no. 3, pp. 212–216, 1998.

[46] E. T. Enikov, S. S. Kedar, and K. V. Lazarov, "Analytical model for analysis and design of v-shaped thermal microactuators," *Microelectromechanical Systems, Journal of*, vol. 14, no. 4, pp. 788–798, 2005.

[47] J. Casals-Terre, A. Fargas-Marques, and A. M. Shkel, "Snap-action bistable micromechanisms actuated by nonlinear resonance," *Microelectromechanical Systems, Journal of*, vol. 17, no. 5, pp. 1082–1093, 2008.

[48] J. Zhao, J. Jia, X. He, and H. Wang, "Post-buckling and snap-through behavior of inclined slender beams," *Journal of Applied Mechanics*, vol. 75, no. 4, p. 041020, 2008.

[49] S. Krylov, B. R. Ilic, D. Schreiber, S. Seretensky, and H. Craighead, "The pull-in behavior of electrostatically actuated bistable microstructures," *Journal of Micromechanics and Microengineering*, vol. 18, no. 5, p. 055026, 2008.

[50] C.-C. Wu, M.-J. Lin, and R. Chen, "Bistable criterion for mechanically bistable mechanism," in *Micro Electro Mechanical Systems (MEMS), 2012 IEEE 25th International Conference on*, pp. 396–399, Jan 2012.

[51] C.-C. Wu, M.-J. Lin, and R. Chen, "The derivation of a bistable criterion for double v-beam mechanisms," *Journal of Micromechanics and Microengineering*, vol. 23, no. 11, p. 115005, 2013.

[52] H. Steiner, W. Hortschitz, M. Stifter, and F. Keplinger, "Thermal actuated passive bistable mems switch," in *Microelectronic Systems Symposium (MESS), 2014*, pp. 1–5, IEEE, 2014.

[53] M. F. Berwind, A. Kamas, and C. Eberl, "A hierarchical programmable mechanical metamaterial unit cell showing metastable shape memory," *Advanced Engineering Materials*, vol. 20, no. 11, p. 1800771, 2018.

[54] A. Ben-Tal and A. Nemirovski, *Lectures on modern convex optimization: analysis, algorithms, and engineering applications*, vol. 2. Siam, 2001.

[55] R. Yang and C. Chuang, "Optimal topology design using linear programming," *Computers and Structures*, vol. 52, no. 2, pp. 265 – 275, 1994.

[56] M. P. Bendsøe and O. Sigmund, *Topology optimization: theory, methods, and applications*. Springer, 2004.

[57] M. P. Bendsøe and N. Kikuchi, "Generating optimal topologies in structural design using a homogenization method," *Computer Methods in Applied Mechanics and Engineering*, vol. 71, no. 2, pp. 197 – 224, 1988.

[58] N. Kikuchi, K. Y. Chung, T. Torigaki, and J. E. Taylor, "Adaptive finite element methods for shape optimization of linearly elastic structures," in *The Optimum Shape*, pp. 139–169, Springer, 1986.

[59] J. Franců, "Homogenization of linear elasticity equations," *Aplikace matematiky*, vol. 27, no. 2, pp. 96–117, 1982.

[60] M. Neves, H. Rodrigues, and J. Guedes, "Optimal design of periodic linear elastic microstructures," *Computers & Structures*, vol. 76, no. 1, pp. 421 – 429, 2000.

[61] S. P. Timoshenko and J. M. Gere, *Theory of elastic stability*. Courier Dover Publications, 2009.

[62] J. B. Ostos, R. Rinaldi, C. m Hammetter, G. Stucky, F. Zok, and A. Jacobsen, "Deformation stabilization of lattice structures via foam addition," *Acta Materialia*, vol. 60, no. 19, pp. 6476–6485, 2012.

[63] C. Hammetter and F. Zok, "Compressive response of pyramidal lattices embedded in foams," *Journal of Applied Mechanics*, April 2013.

[64] H. N. Wadley, "Multifunctional periodic cellular metals," *Philosophical Transactions of the royal society A-Mathematical physical and engineering sciences*, vol. 364, pp. 31–68, 2006.

[65] L. Gordon, B. Bouwhuis, M. Suralvo, J. McCrea, G. Palumbo, and G. Hibbard, "Micro-truss nanocrystalline ni hybrids," *Acta Materialia*, vol. 57, no. 3, pp. 932–939, 2009.

[66] L. Valdevit, S. W. Godfrey, T. A. Schaedler, A. J. Jacobsen, and W. B. Carter, "Compressive strength of hollow microlattices: Experimental characterization, modeling, and optimal design," *Journal of Materials Research*, pp. 1–13, 2013.

[67] Abaqus, "Abaqus analysis user's manual," 2009.

[68] B. G. Compton and J. A. Lewis, "3d-printing of lightweight cellular composites," *Advanced materials*, vol. 26, no. 34, pp. 5930–5935, 2014.

[69] J. R. Raney, B. G. Compton, J. Mueller, T. J. Ober, K. Shea, and J. A. Lewis, "Rotational 3d printing of damage-tolerant composites with programmable mechanics," *Proceedings of the National Academy of Sciences*, vol. 115, no. 6, pp. 1198–1203, 2018.

[70] A. Ortona, C. D'Angelo, S. Gianella, and D. Gaia, "Cellular ceramics produced by rapid prototyping and replication," *Materials Letters*, vol. 80, pp. 95 – 98, 2012.

[71] A. F. Skutch, "Anatomy of leaf of banana, musa sapientum l. var. hort. gros michel," *Botanical Gazette*, vol. 84, no. 4, pp. 337–391, 1927.

[72] A. F. Skutch, "Anatomy of the axis of the banana," *Botanical Gazette*, vol. 93, no. 3, pp. 233–258, 1932.

[73] A. F. Skutch, "On the development and morphology of the leaf of the banana (musa sapientum l.)," *American Journal of Botany*, vol. 17, no. 4, pp. 252–271, 1930.

[74] L. J. Gibson, "The hierarchical structure and mechanics of plant materials," *Journal of the royal society interface*, vol. 9, no. 76, pp. 2749–2766, 2012.

[75] M. Avalle, G. Belingardi, and R. Montanini, "Characterization of polymeric structural foams under compressive impact loading by means of energy-absorption diagram," *International Journal of Impact Engineering*, vol. 25, no. 5, pp. 455–472, 2001.

[76] R. Lakes, "Materials with structural hierarchy," *Nature*, vol. 361, no. 6412, p. 511, 1993.

[77] F. Ziebert, H. Mohrbach, and I. M. Kulić, "Why microtubules run in circles: Mechanical hysteresis of the tubulin lattice," *Phys. Rev. Lett.*, vol. 114, p. 148101, Apr 2015.

[78] T. A. Reid, C. Coombes, and M. K. Gardner, "Manipulation and quantification of microtubule lattice integrity," *Biology Open*, vol. 6, no. 8, pp. 1245–1256, 2017.

[79] E. H. Kellogg, N. M. Hejab, S. Howes, P. Northcote, J. H. Miller, J. F. Díaz, K. H. Downing, and E. Nogales, "Insights into the distinct mechanisms of action of taxane and non-taxane microtubule stabilizers from cryo-em structures," *Journal of Molecular Biology*, vol. 429, no. 5, pp. 633 – 646, 2017.

[80] G. Alushin, G. Lander, E. Kellogg, R. Zhang, D. Baker, and E. Nogales, "High-resolution microtubule structures reveal the structural transitions in $\alpha\beta$-tubulin upon gtp hydrolysis," *Cell*, vol. 157, no. 5, pp. 1117 – 1129, 2014.

[81] H. Doodhi, A. Prota, R. Rodríguez-García, H. Xiao, D. Custar, K. Bargsten, E. Katrukha, M. Hilbert, S. Hua, K. Jiang, I. Grigoriev, C.-P. Yang, D. Cox, S. Horwitz, L. Kapitein, A. Akhmanova, and M. Steinmetz, "Termination of protofilament elongation by eribulin induces lattice defects that promote microtubule catastrophes," *Current Biology*, vol. 26, no. 13, pp. 1713 – 1721, 2016.

[82] J. SIDAROUS and M. VANDERBILT, "An analytical methodology for predicting dynamic building response to wind," in *Wind Engineering* (J. CERMAK, ed.), pp. 709 – 724, Pergamon, 1980.

[83] J. Sadler, "On the analytical lumped-mass model of an elastic four-bar mechanism," *Journal of Engineering for Industry*, vol. 97, no. 2, pp. 561–565, 1975.

[84] S. BODNER and P. SYMONDS, "Plastic deformations in impact and impulsive loading of beams**the results presented in this paper were obtained in the course of research sponsored by the office of naval research under contract nonr-562(10) with brown university.," in *Plasticity* (E. LEE and P. SYMONDS, eds.), pp. 488 – 500, Pergamon, 1960.

[85] J. W. Pro, R. K. Lim, L. R. Petzold, M. Utz, and M. R. Begley, "Gpu-based simulations of fracture in idealized brick and mortar composites," *Journal of the Mechanics and Physics of Solids*, vol. 80, pp. 68 – 85, 2015.

[86] R. K. Lim, J. W. Pro, M. R. Begley, M. Utz, and L. R. Petzold, "High-performance simulation of fracture in idealized 'brick and mortar' composites using adaptive monte carlo minimization on the gpu," *The International Journal of High Performance Computing Applications*, vol. 30, no. 2, pp. 186–199, 2016.

[87] J. W. Pro, *Distributed cohesive zone methods for modeling fracture in brittle coating systems & composites*. PhD thesis, University of California, Santa Barbara, 2016. Copyright - Database copyright ProQuest LLC; ProQuest does not claim copyright in the individual underlying works; Last updated - 2017-03-07.